UNIVERSITÀ DI PISA

Department of Information Engineering

PhD Course in Remote Sensing

Anomalous change detection in multi-temporal hyperspectral images

Salvatore Resta

Advisors

Prof. Ing. Giovanni Corsini _____

Prof. Ing. Marco Diani _____

Ing. Nicola Acito _____

December 2012

SSD: ING-INF/03

Abstract

In latest years, the possibility to exploit the high amount of spectral information has made hyperspectral remote sensing a very promising approach to detect changes occurred in multi-temporal images. Detection of changes in images of the same area collected at different times is of crucial interest in military and civilian applications, spanning from wide area surveillance and damage assessment to geology and land cover. In military operations, the interest is in rapid location and tracking of objects of interest, people, vehicles or equipment that pose a potential threat. In civilian contexts, changes of interest may include different types of natural or manmade threats, such as the path of an impending storm or the source of a hazardous material spill.

In this PhD thesis, the focus is on Anomalous Change Detection (ACD) in airborne hyperspectral images. The goal is the detection of small changes occurred in two images of the same scene, i.e. changes having size comparable with the sensor ground resolution. Specifically, the ACD problem can be stated as follows: given two images of the same scene collected at different times, referred to as the test image and the reference image, respectively, ACD algorithms aim to identify the set of pixels that are

significantly different between the two images. The objects of interest typically occupy few pixels of the image and change detection must be accomplished in a pixel-wise fashion. Moreover, since the images are in general not radiometrically comparable, because illumination, atmospheric and environmental conditions change from one acquisition to the other, pervasive and uninteresting changes must be accounted for in developing ACD strategies.

ACD process can be distinguished into two main phases: a pre-processing step, which includes radiometric correction, image co-registration and noise filtering, and a detection step, where the pre-processed images are compared according to a defined criterion in order to derive a statistical ACD map highlighting the anomalous changes occurred in the scene. In the literature, ACD has been widely investigated providing valuable methods in order to cope with these problems. In this work, a general overview of ACD methods is given reviewing the most known pre-processing and detection methods proposed in the literature. The analysis has been conducted unifying different techniques in a common framework based on binary decision theory, where one has to test the two competing hypotheses H_0 (change absent) and H_1 (change present) on the basis of an observation vector derived from the radiance measured on each pixel of the two images.

Particular emphasis has been posed on statistical approaches, where ACD is derived in the framework of Neymann Pearson theory and the decision rule is carried out on the basis of the statistical properties assumed for the two hypotheses distribution, the observation vector space and the secondary data exploited for the estimation of the unknown parameters. Typically, ACD techniques assume that the observation represents the realization of jointly Gaussian spatially stationary random process. Though such assumption is adopted because of its mathematical tractability, it may be quite simplistic to model the multimodality usually met in real data. A more appropriate model is that adopted to derive the well known RX anomaly detector which assumes the local Gaussianity of the hyperspectral data. In this framework, a new statistical ACD method has been proposed considering the local Gaussianity of the hyperspectral data. The assumption of local stationarity for the observations in the two hypotheses is taken into account by considering two different models, leading to two different detectors.

In addition, when data are collected by airborne platforms, perfect co-registration between images is very difficult to achieve. As a consequence, a residual mis-registration (RMR) error should be taken into account in developing ACD techniques. Different techniques have been proposed to cope with the performance degradation problem due to the RMR, embedding the a priori knowledge on the statistical properties of the RMR in the change detection scheme. In this context, a new method has been proposed for the estimation of the first and second order statistics of the RMR. The technique is based on a sequential strategy that exploits the Scale Invariant Feature Transform (SIFT) algorithm cascaded with the Minimum Covariance Determinant algorithm. The proposed method adapts the SIFT procedure to hyperspectral images and improves the robustness of the outliers filtering by means of a highly robust estimator of multivariate location.

Then, the attention has been focused on noise filtering techniques aimed at enforcing the consistency of the ACD process. To this purpose, a new method has been proposed to mitigate the negative effects due to random noise. In particular, this is achieved by means of a band selection technique aimed at discarding spectral channels whose useful signal content is low compared with the noise contribution. Band selection is performed on a per-pixel basis by exploiting the estimates of the noise variance accounting also for the presence of the signal dependent noise component.

Finally, the effectiveness of the proposed techniques has been extensively evaluated by employing different real hyperspectral datasets containing anomalous changes collected in different acquisition conditions and on different scenarios, highlighting advantages and drawbacks of each method.

In summary, the main issues related to ACD in multi-temporal hyperspectral images have been examined in this PhD thesis. With reference to the pre-processing step, two original contributions have been offered: i) an unsupervised technique for the estimation of the RMR noise affecting hyperspectral images, and ii) an adaptive approach for ACD which mitigates the negative effects due to random noise. As to the detection step, a survey of the existing techniques has been carried out, highlighting the major drawbacks

and disadvantages, and a novel contribution has been offered by presenting a new statistical ACD method which considers the local Gaussianity of the hyperspectral data.

Index terms: anomalous change detection, hyperspectral images, mis-registration noise estimation, binary decision theory.

Contents

List of tables

List of figures

List of acronyms

AACD	Adaptive Anomalous Change Detection
ABS	Adaptive Band Selection
ACD	Anomalous Change Detection
AD	Anomaly Detection
CC	Chronochrome
CD	Change Detection
CE	Covariance Equalization
CP	Control Point
CVA	Change Vector Analysis
CV	Combined Vector
DEM	Digital Elevation Model
DR	Dimensionality Reduction
DV	Difference Vector
EC	Elliptically Contoured
FAR	False Alarm Rate
FODT	Fraction Of Detected Target
GLI	Gray Level Image
GLRT	Generalized Likelihood Ratio Test
GRC	Ground Resolution Cell
GT	Ground Truth
HACD	Hyperbolic Anomalous Change Detection
HYNPE	Hyperspectral Noise Parameters Estimation
HSI	Hyperspectral Image

IGM	Input Geometry
INS	Inertial Navigation System
JV	Joint Vector
KP	Keypoint
LCRA	Local Co-Registration Adjustment
LR	Likelihood Ratio
MAD	Median Absolute Deviation
MCD	Minimum Covariance Determinant
MD	Magnitude Direction
MSE	Mean Square Error
NCC	Normalized Cross-correlation
NP	Neyman Pearson
NW	Noise Whitening
PCA	Principal Component Analysis
PCC	Pearsonian Correlation Coefficient
PDF	Probability Density Function
RGB	Red Green Blue
RMR	Residual Mis-Registration
RN	Registration Noise
ROC	Receiver Operating Characteristic
RSE	Root Square Error
SAM	Spectral Angle Mapper
SCM	Spectral Correlation Mapper
SCV	Spectral Change Vector
SIFT	Scale Invariant Feature Transform

SNR	Signal to Noise Ratio
SP	Subspace Projection
SRMRE	Sequential Residual Mis-Residual Estimation
SSI	Signal Subspace Identification
TPS	Thin Plate Spline
UW	Uncertainty Window
VIS	Visible
VNIR	Visible Near Infrared
WD	Whitening/Dewhitening

Chapter 1

Anomalous change detection in hyperspectral images

This chapter introduces the problem of change detection in multi-temporal images highlighting the main challenges and the numerous related research topics. After briefly surveying the main techniques proposed in the literature in change detection applications, the chapter addresses anomalous change detection in hyperspectral images. On the basis of the general description of the problem, the main motivation, the novelties and the structure of the thesis are illustrated.

1.1 Problem statement

Change Detection (CD) is a challenging task aimed at detecting a set of pixels that are substantially different in multi-temporal images of the same scene. CD has been effectively employed for environmental monitoring, such as in geology, land cover and

hydrology [1],[2] and for defence and surveillance applications (e.g. tracking of vehicles, identification of potential threats, damage assessment [3],[4]). In the literature, this problem has been addressed exploiting temporal series of images acquired by both active [5]-[8] and passive sensors [9]-[12]. In this PhD thesis, the interest is in CD based on the analysis of multi-temporal hyperspectral images (HSI). This topic represents an emerging field of research that is gaining increasing interest in the scientific community because of the potential benefits expected in military and civilian applications. Generally speaking, in military application hyperspectral imaging has widened prospects for intelligence information gathering. Research efforts in HSI processing have been extensively conducted in Anomaly Detection (AD, [13],[14],[15]) applications (i.e. the presence of man-made objects in a natural background) which allow the analyst to rapidly locate deceived targets by considering one image at a time. Despite the suggestion that AD would suffice for military applications, it will only partially reduce the great amount of data arising from HSI ([16],[17],[18]). To interpret all anomalies every time they appear in an image would still require a considerable effort, while most of those anomalies will not require repeated analysis. Conversely, by adopting proper change detection algorithms in the considered scenario, the analyst's attention would be streamlined towards objects/areas of potential interest, reducing the requirement for accurate analysis on every scene while increasing the analyst's capacity with respect to small but anomalous changes [19]. Related applications of interest concern chemical and biological weapons use, power plant growing and configuration, and many other examples in which imagery analysts spend a relevant amount of time. In civilian applications, CD techniques based on HSI have demonstrated potential as a means to detect, identify, and map changes in forest cover [19],[21], damage assessment after disaster/extraordinary natural events, monitoring of the impact of human activities on built up and urbanized region of the earth surface [22],[23].

CD in HSI is accomplished by checking for changes in the spectrum of spatially coincident pixels/areas in the different images. Such spectral changes may be caused by object motion or by a change in the region status.

CD has many aspects that are strictly related to the field of image processing. Works presented in the literature witness that CD has indeed benefited from studies on image

registration [24]-[27], background statistical modelling [10], optical flow [28],[29] and non-uniformity artefacts correction [18]. Furthermore, different solutions to the CD problem have been proposed in the remote sensing literature for environmental monitoring and surveillance applications from both spaceborne and airborne platforms ([21],[23],[30]).

Broadly speaking, a CD algorithm should take the image pair as input and generate a single image, called the change statistic whose highest values should be associated to the relevant changes. The challenge is designing a CD strategy mostly insensitive to non relevant or pervasive changes, such as those induced by sensor noise, contrast, brightness or focus differences, shadow and camera motion, or atmospheric or even seasonal changes.

The distinction between pervasive and relevant changes, which is fundamental for the choice of the proper CD strategy, depends on the application of interest. Thus, in this work, we confine our interest to the detection of small changes resulting from insertion, deletion or movement of small size objects (generally man-made), as well as from small stationary objects whose spectrum changes from one image to another, as in the case of camouflage, concealment and deception. This kind of CD problem, which is known in the literature as Anomalous Change Detection (ACD), has been deeply investigated ([31],[32],[33]) in both aerial and terrestrial applications ([34],[35]).

Basically, the general process of change detection is best looked at as having two main steps. The first one is a pre-processing step, which includes radiometric and geometric correction. These aspects are mainly due to physical constraints associated to the acquisition process. In fact, when the emitted or reflected electro-magnetic energy is acquired by a sensor installed onboard an aircraft or spacecraft, the collected energy does not coincide with the energy emitted or reflected from the same portion of the scene observed in a different time. This is mainly due to variation in atmospheric conditions, sun's azimuth and elevation, presence of aerosols which modify the observed energy. Therefore, in order to make multi-temporal images radiometrically comparable, those radiometric distortions must be corrected. Several algorithms have been presented in the literature to cope with this problem, such as the Chronochrome

(CC, [36]), which represents the optimal linear mean square error predictor, and the Covariance Equalization (CE, [37]), which represents a suboptimal solution requiring less binding constraint than the CC, both in their global and cluster based versions ([38],[39]).

Geometric correction is concerned with the correspondence between homologous pixels of the images being collected, so that the pixels of each image refer to same portion of the scene. In the case of aerial or satellite images, this operation is performed by transforming the geodetic or UTM coordinates available of each pixel to image coordinates.

The ACD process can be further enforced by means of additional techniques, such as noise filtering and/or dimensionality reduction. In the first case, a proper technique for random noise reduction could be applied to the image pair before the final results can be obtained. In the second case, any method of data reduction, such as the Temporal Principal Component Analysis (TPCA, [40]), could be applied as the first step [41].

The second phase is the detection step, in which the dissimilarity between corresponding pixels in the two images is evaluated on the basis of the observation vector that depends on the values of corresponding pixels of both the test and the reference image.

In particular, two main classes of detectors have been presented in the literature. The first class refers to deterministic approaches, where no statistical model is assumed for the observation and the ACD process is aimed at detecting changes by means of a deterministic measure of similarity between corresponding pixel vectors. Within this class, different detectors are illustrated, based on Euclidean distance and angular metrics, such as the Change Vector Analysis (CVA, [10]), the Spectral Angle Mapper (SAM, [42]), the Pearsonian Correlation Coefficient (PCC, [43]) and the Spectral Correlation Mapper (SCM, [19]).

While the first detector class is aimed at detecting changes by means of similarity measures relying on deterministic and geometric concepts, the class of statistical ACD algorithms employs a detection scheme derived in the framework of Neymann Pearson

theory. The statistical model assumed to solve the decision problem leads to a detection rule that is based on the Mahalanobis distance between the observation vector and the no change class. Such general structure of the detector includes two well established ACD strategies, the Difference Based ACD ([44]), the Straight RX ACD ([34]) and a recently proposed technique, named Hyperbolic ACD (HACD, [45]).

Afterwards, these algorithms are extended so as to take into account a Residual Mis-Registration (RMR). RMR stems from the difficulty to achieve a perfect co-registration between images. This error can be viewed as a per-pixel shift in both the row and column directions, ranging in magnitude from a fraction of pixel to few pixels. Several methods have been proposed to reduce the effects of RMR errors, based on the Change Vector Analysis (CVA) in the Magnitude-Direction (MD) domain [46],[47], the gradient of the registered image combined with a Thin Plate Spline (TPS) transform [48] and the normalized cross-correlation for selected channels of the image pairs [49].

Recently, the Local Co-Registration Adjustment (LCRA, [51],[52]) approach has been developed, embedding the a priori knowledge on the RMR statistics in the change detection framework. Basically, the LCRA approach compares the Pixel Under Test (PUT) of the test image with those belonging to a given neighborhood, or uncertainty window (UW), in the reference image. The UW size and shape depend on the statistical properties of the RMR ([19]). The choice of the UW is crucial in that it strongly influences both the detection performance and the computational load of LCRA based ACD algorithms. In fact, on one hand the UW should be large enough to allow the RMR effects to be properly compensated, on the other hand, it should be as small as possible to avoid the mis-detection of anomalous changes. When GPS positional errors, INS angular errors and DEM errors [53] are not available, the estimation of the RMR noise remains an open issue, and the UW is generally set in an almost arbitrary fashion by making some assumptions about the magnitude of the RMR.

In this PhD work, a new fully unsupervised algorithm, named Sequential Residual Mis-Registration Estimation (SRMRE, [54]) is proposed to estimate the magnitude of the RMR directly from the image pairs. The proposed technique assumes the RMR as a unimodal bivariate random variable and estimates both its mean value and its

covariance matrix. Such estimates allow the UW in LCRA approach to be precisely defined. The method is based on the Scale Invariant Feature Transform (SIFT, [57],[58]) algorithm, which represents a well-established technique for extracting interest points in gray level images on the basis of their local spatial features. The SIFT algorithm is embedded in a sequential processing scheme that allows the potential distinct spectral features present in the numerous channels of the hyperspectral data to be accounted for. The algorithm does not require ancillary data about the instrumentation accuracy. Therefore, in ACD problems, it can be successfully applied as a method to mitigate the effect of misalignment both after the co-registration step and in those applications that use the image pairs aligned through direct geo-referencing.

In applying ACD algorithms embedded in the LCRA approach to real data, a strong sensitivity of the detection algorithms to the presence of the random noise has been experienced [42]. Significant evidence of this criticism has been noticed in spatial regions made by materials exhibiting low values of the useful signal (as compared to the noise variance) in a certain number of spectral channels.

As a result, the use of the entire available spectrum leads to a reduction in the overall performance. To improve the robustness of the algorithm to random noise, a new adaptive band selection approach has been proposed. The strategy, which is called Adaptive ACD (AACD, [59]) selects the bands where the signal level is higher than the noise standard deviation. Band selection is performed on a per-pixel basis, thus the number of retained bands may change from one pixel to another. The selection strategy exploits the estimates of the noise variance obtained from the analyzed image. In particular, this is achieved by also accounting for the presence of the signal dependent noise affecting data acquired by new generation sensors. For this purpose a recently developed algorithm, named Hyperspectral Noise Parameters Estimation (HYNPE, [55]), is employed. The basic idea behind the proposed band selection strategy is to retain only the bands, for a given pixel, where the signal content is sufficiently strong to be reliably detected.

Afterwards, a new ACD technique, named Combined Vector ACD (CV-ACD, [56]), is proposed considering the previously introduced common framework. The proposed

technique considers the more appropriate model adopted to derive the well known RX anomaly detector which takes into account the local Gaussianity of the hyperspectral data. The assumption of local stationarity for the observations in the two hypotheses is adopted as a common support in the statistical model of the observation. On the basis of the secondary data exploited for the estimation of the unknown parameters, two new different detectors are derived.

The effectiveness of the proposed techniques has been evaluated on real HSIs containing several anomalous changes of different size and material collected in different acquisition conditions and on different scenarios, highlighting advantages and drawbacks of each method.

1.2 Outline of the thesis

A theoretical framework embedding the main ACD methods in hyperspectral imaging proposed in the literature is dealt with in Chapter 2. The analysis in conducted formulating ACD as a binary decision problem between the two competing hypotheses, H_0 (change absent) and H_1 (change present). A brief insight into the two main classes of detectors, deterministic and statistical, respectively, and on their relative assumptions is given. A rigorous mathematical derivation of the statistical ACD methodology is then provided modelling the observation conditioned to the hypotheses H_0 and H_1 as a multivariate Gaussian vector with different parameters.

The problem of residual mis-registration (RMR) noise estimation is dealt with in Chapter 3. In particular, a statistical model of the RMR and its parameters is first illustrated. Although such parameters could be theoretically provided with the geo-referencing instrumentation, they are typically unavailable. This prevents ACD strategies aimed at reducing the effects of the RMR to be effectively exploited. A solution to face this limitation is proposed. In particular, a novel technique designed for estimating the RMR parameters in a completely unsupervised manner is presented, providing reliable and accurate estimates of the RMR noise parameters.

Chapter 4 presents a novel methodology to cope with random noise affecting hyperspectral data collected in different acquisition conditions. To this aim, the use of a band selection technique and a noise whitening procedure is adopted in an adaptive fashion, exploiting the SNR estimates of the collected image per pixel per band.

In Chapter 5, attention is focused on a novel statistical ACD technique, based on a more appropriate model distribution of each pixel vector conditioned to the two competing hypotheses. In particular, it considers the multivariate local Gaussian model proposed in the well known RX algorithm for anomaly detection applications. The method overcomes relevant drawbacks exhibited by the other methods and show its appropriateness for processing the image line by line, following the data collection scheme typical of push-broom sensors.

Experimental evidence of the actual advantages offered by the proposed solutions is obtained by extensively analyzing different real multi-temporal hyperspectral images collected in different scenarios at the end of the last three chapters. Finally, Chapter 6 concludes the thesis outlining a summary and providing the final remarks and suggestions.

Chapter 2

A theoretical overview of ACD methods in HSI

This chapter presents an overview of the main state-of-the-art ACD methods. The analysis is conducted in the purpose of embedding different techniques in a common framework based on binary decision theory. Specifically, two different approaches, referred to as deterministic and statistical approach, respectively, are introduced following the same binary decision problem framework. Afterwards, the analysis is extended to dedicated pre-processing methods, aimed at enforcing the consistency of the ACD process.

2.1 Introduction

Anomalous Change Detection (ACD) is aimed at detecting a set of pixels that are substantially different in multi-temporal images of the same scene. ACD has been

effectively employed for defence and surveillance applications (e.g. tracking of vehicles, identification of potential threats, damage assessment [4],[11]). In this framework, ACD based on the analysis of multi-temporal HSI is a recent emerging technology that is gaining increased interest in the research community because of the potential benefits expected in practical applications. ACD in HSI is accomplished by checking for changes in the spectrum of spatially coincident pixels/areas in the different images. Such spectral changes may be caused by object motion or by a change in the object status as, for example, in the case of camouflaged objects.

ACD algorithms take the image pair as input and generate a single image, called the change statistic whose highest values should be associated to the relevant changes. The challenge is designing a ACD strategy mostly insensitive to non relevant or pervasive changes, such as those induced by sensor noise, contrast, brightness or focus differences, shadow and camera motion, or atmospheric or even seasonal changes.

This chapter presents an overview of the main state-of-the-art ACD methods and pre-processing techniques aimed at enforcing the consistency of the ACD process. The analysis explores the whole ACD processing chain and it is conducted in order to highlight advantages and drawbacks of each method, so as to define the most appropriate technique for the considered application.

Specifically, the ACD problem is approached using a pixel-level scheme. ACD is formulated as a binary decision problem where one has to test the two competing hypotheses on the basis of an observation vector derived from the radiance measured on each pixel of the two images:

$$\begin{aligned} &H_0 : \text{Change Absent} \\ &H_1 : \text{Change Present} \end{aligned} \tag{2.1}$$

where H_0 is the no change occurred hypothesis and H_1 is the change occurred hypothesis.

In general terms, the ACD process can be distinguished into two main phases: a pre-processing step, which includes radiometric correction, image co-registration and eventually noise filtering and/or dimensionality reduction, and a detection step, where

the resulting images are compared according to a defined criterion in order to evaluate the ACD statistic.

To introduce the basics of the ACD process, let us denote as $\mathbf{Y}$ and $\mathbf{Z}$ the two images to be analyzed, which will be referred to as the test image and the reference image, hereinafter. In particular, $\mathbf{Y} \in R^{L \times N_S \times N_L}$ and $\mathbf{Z} \in R^{L \times N_S \times N_L}$, where N_S and N_L represent, respectively, the spatial dimensions of the two images and L is the number of spectral channels. Let us also denote as $\mathbf{y}(i,j) = [y_1(i,j), y_2(i,j), ..., y_L(i,j)]^T$ and $\mathbf{z}(i,j) = [z_1(i,j), z_2(i,j), ..., z_L(i,j)]^T$ the generic pixel vector of the collected at-sensor radiance of the test and reference image, respectively. Each pixel is viewed as a $L \times 1$ random vector (RV) in the spatial position (i,j) (i and j are the sample and the line indexes respectively, i.e. $i = [1, ..., N_S]$, $j = [1, ..., N_L]$).

In the first part of this chapter we assume that: i) the two images are perfectly co-registered, so that the value of the spectral signature of the vectors $\mathbf{y}(i,j)$ and $\mathbf{z}(i,j)$ associated to the spatial coordinates (i,j) in both images represents the same physical area; ii) the two images are radiometrically comparable that is, the same acquisition conditions are assumed for both the images.

On the basis of the above stated assumptions, according to pixel-based ACD scheme, the dissimilarity between corresponding pixels in the two images is assessed by means of a function $T(i,j)$ depending only on the pixel vectors in the (i,j) position, and the decision is taken on the basis of the observation vector $\mathbf{e}(i,j)$ that depends on the values of $\mathbf{y}(i,j)$ and $\mathbf{z}(i,j)$. In particular, two main classes of detectors are initially introduced. The first class refers to deterministic approaches, where no statistical model is assumed for the observation, and the ACD process is aimed at detecting changes by means of a deterministic measure of similarity between corresponding pixel vectors. Within this class, different detectors have been proposed in the literature, based on Euclidean distance and angular metrics, such as the Change Vector Analysis (CVA, [10]), the Spectral Angle Mapper (SAM, [42]), the Pearsonian Correlation Coefficient (PCC, [43]) and the Spectral Correlation Mapper (SCM, [19]).

The second class refers to statistical approaches, where the ACD scheme has been derived in the framework of Neymann Pearson theory and the decision rule is carried out on the basis of the statistical properties assumed for the two hypotheses distribution, the observation vector space and the secondary data exploited for the estimation of the unknown parameters. The statistical model assumed to solve the decision problem leads to a detection rule that is based on the Mahalanobis distance between the observation vector and the no change class. Such general structure of the detector includes two well established ACD strategies, the Difference Based ACD ([44]) and the Straight RX ACD ([34]), and it is further adopted in this work to derive a new ACD strategy, which will be presented in a dedicated chapter. Moreover, a recently proposed technique, named Hyperbolic ACD (HACD, [45]) is described considering a statistical ACD framework which makes use of a detector based on the same structure considered in the former case.

Afterwards, we remove the previously considered simplifying assumptions and approach the more general case where i) the two images are not perfectly co-registered, and ii) they are collected in different acquisition conditions, i.e. they are not radiometrically comparable. Concerning the first hypothesis, a Residual Mis-Registration (RMR) error is taken into account in developing ACD strategies. To this purpose, an effective approach named Local Co-registration Adjustment (LCRA, [51],[52]), recently proposed in the literature to cope with the performance degradation due to RMR, is presented, and the different detectors initially introduced in a pixel wise fashion are adapted to the LCRA case. Concerning the second assumption, we consider the case in which the two images are collected in different atmospheric conditions, so that they are not radiometrically comparable. To this purpose, we describe the most popular techniques which have been proposed in the literature, the Chronochrome (CC, [36]) which represents the minimum MSE (MMSE) predictor based on multivariate linear regression, and the Covariance Equalization (CE, [37]), both in its global and cluster based version ([38],[39]).

The chapter is organized as follows. section 2.2 describes the most common deterministic approaches proposed in the literature; section 2.3 introduces the statistical theoretical framework for ACD. In particular, the same structure based on decision

theory is adopted to describe three well established ACD techniques. Afterwards, in section 2.4 and 2.5 an extensive analysis of additional constraints in ACD problems is performed. In particular, section 2.4 examines the case in which the two images are not perfectly co-registered, analyzing the effects of the RMR in the detection performance and describing the approaches proposed to cope with the performance degradation due to RMR. section 2.5 considers the case in which the two images are not radiometrically comparable, describing the most common pre-processing methods proposed in the literature to deal with this aspect.

2.2 Deterministic methods

We start by introducing the first class of ACD detectors, which refers to deterministic methods. They are based on a measure of similarity between corresponding pixel vectors, and they do not assume any statistical hypothesis for the observation. Due to the numerous aspects and physical constraints related to HSI in ACD, different solutions have been proposed in the literature [60],[61]. In particular, in this chapter two different kind of metrics are examined, based on Euclidean distance [63] and angular measures, respectively [64]. Concerning the first class of detectors, we consider the Change Vector Analysis approach (CVA, [65]), and we further describe an additional approach, recently proposed in the literature by projecting the observation on a different coordinate system [10]. Then, in the framework of angular metrics, three different detectors are presented, the Spectral Angle Mapper (SAM, [42]), the Pearsonian Correlation Coefficient (PCC, [43]) and the Spectral Correlation Mapper (SCM, [19]). The ACD process is carried out by exploiting a measure of similarity evaluated on the observation vector $\mathbf{e}(i,j)$. In particular, the resulting ACD detector depends from the specific form assumed by the observation $\mathbf{e}(i,j)$, which is a function of the two corresponding pixel vectors $\mathbf{y}(i,j)$ and $\mathbf{z}(i,j)$ of the test and the reference image, respectively.

2.2.1 Change Vector Analysis (CVA) based ACD (CVA-ACD)

Given the pixel pair $\mathbf{y}(i,j)$ and $\mathbf{z}(i,j)$, in the CVA approach we define the observation $\mathbf{e}(i,j)$ as:

$$\mathbf{e}(i,j) = \mathbf{y}(i,j) - \mathbf{z}(i,j) \tag{2.2}$$

In ACD problems, the observation vector defined according to (2.2) has been equivalently denoted as Spectral Change Vector (SCV, [10]) or Difference Vector (DV, [66]). When the images are perfectly co-registered and radiometrically comparable, the CVA results as the most natural choice for ACD. In particular, it is given by the Euclidean Norm of the SCV:

$$T_E(i,j) = \|\mathbf{e}(i,j)\|_2 \tag{2.3}$$

In equation (2.3), $\|\ \|_2$ denotes the L2 norm, which can be equivalently expressed as $\|\mathbf{e}(i,j)\|_2 = \sqrt{\mathbf{e}(i,j)^T \cdot \mathbf{e}(i,j)}$. The CVA method computes the degree of anomalousness between corresponding pixels by determining the Euclidean distance through *L*-dimensional change space. In particular, according to the CVA, the higher is the distance, the more is the difference between the compared spectra $\mathbf{y}(i,j)$ and $\mathbf{z}(i,j)$. CVA is typically adopted as an empirical measure of anomalousness and it does not consider any specific theoretical framework in order to address all the information contained in the SCV. The detector (2.3) will be referred to as CVA-ACD, hereinafter.

2.2.1.1 CVA in the polar domain

In most of the applications, only the magnitude of the CVA is exploited in order to evaluate the ACD statistic, leading to a suboptimal exploitation of the information content arising from the SCV. Recently, a new technique has been proposed in the literature [10], where the ACD is performed by considering a different coordinate

system. In particular, the SCV is represented in an L-dimensional hyperspherical coordinate system, where the multidimensional pixel vector $\mathbf{e}(i,j)$ is described in terms of magnitude ($\rho(i,j)$), and an $L-1$ dimensional vector $\left[\vartheta_1(i,j),\vartheta_2(i,j),...,\vartheta_{N_C-1}(i,j)\right]$ that represents the change vector angular coordinates.

The relationship between the SCV represented in the Cartesian and the hyperspherical coordinate system is the following:

$$\begin{aligned} &e_1(i,j)=\rho(i,j)\cdot\cos(\vartheta_1(i,j))\\ &e_2(i,j)=\rho(i,j)\cdot\sin(\vartheta_1(i,j))\cdot\cos(\vartheta_2(i,j))\\ &...\\ &e_L(i,j)=\rho(i,j)\cdot\sin(\vartheta_1(i,j))\cdot\sin(\vartheta_2(i,j))\cdot...\cdot\cos(\vartheta_{L-1}(i,j)) \end{aligned} \tag{2.4}$$

where $\rho(i,j)\in[0,\rho_{\max}]$, $\vartheta_1(i,j)\in[0,2\pi)$ and $\vartheta_1(i,j),\vartheta_2(i,j),...,\vartheta_{L-1}(i,j)\in[0,\pi]$. Notice that $\rho_{\max}$ is the maximum value assumed by the magnitude on the considered difference image, i.e. $\rho_{\max}=\max_{i,j}\left\{\left(e_1(i,j)^2+e_2(i,j)^2+...+e_L(i,j)^2\right)^{1/2}\right\}$.

The representation of the SCV in the magnitude-direction (MD) domain permits us to identify distinct regions containing different information. In particular, to better explain how the SCV in the MD domain can be exploited in ACD, let us assume that the CVA technique is applied to a multi-temporal dataset consisting of two spectral channels, i.e. $\mathbf{y}(i,j)=[y_1(i,j),y_2(i,j)]$ and $\mathbf{z}(i,j)=[z_1(i,j),z_2(i,j)]$ (the analysis can be further generalized by considering more directions). In this case, the SCV is the two dimension vector given by $\mathbf{e}(i,j)=[e_1(i,j),e_2(i,j)]$. The representation of the SCV $\mathbf{e}(i,j)$ in the MD domain can be expressed as:

$$\begin{aligned} &\rho(i,j)=\sqrt{e_1(i,j)^2+e_2(i,j)^2}\\ &\vartheta(i,j)=\arctan\left(\frac{e_1(i,j)}{e_2(i,j)}\right) \end{aligned} \tag{2.5}$$

where, similarly to the CVA, the higher is the magnitude, the more different are the compared spectra. Therefore, since the two images are supposed to be radiometrically comparable, the MD domain can be separated in two different regions, the circle C_n of no-changed pixels, $C_n=\{(i,j):0\le\rho(i,j)\le T,0\le\vartheta(i,j)\le 2\pi\}$ and the annulus A_c of changed

pixels, $A_c = \{(i,j): T \le \rho(i,j) \le \rho_{\max}, 0 \le \vartheta(i,j) \le 2\pi\}$, respectively. Moreover, in the MD domain we can introduce a further definition, related to sectors S_k:

$$S_k = \{(i,j): T \le \rho(i,j) \le \rho_{\max}, \vartheta_k \le \vartheta(i,j) \le \vartheta_{k+1}\} \tag{2.6}$$

where $0 \le \vartheta_k \le \vartheta_{k+1} \le 2\pi$, $k = 1,2,...,K$. Sectors are mainly related to the direction of the change vectors and therefore they can add useful information related to the kind of changes occurred in the scene. In particular, it is expected that pixels belonging to the same kind of change are included in the same sector. In [10] the authors propose to exploit the information related to angular sectors in multispectral images by means of clustering techniques in order to achieve the more ambitious goal of change understanding, i.e. segmenting changes by semantic type.

2.2.2 Correlation based methods

In this paragraph we focus on physically-based spectral distance metrics, which treat test and reference spectra as *L*-dimensional vectors in the feature space. In classification and detection applications with HSI, the use of appropriate distance metrics, aimed at describing spectral characteristics in mathematical or physical meaning, has shown to achieve better results as compared to methods based on Euclidean distance [63]. Within the class of deterministic methods used in HSI, one of the most important and widely used spectral distance metric for classification and material identification is the Spectral Angle Mapper (SAM, [59]), which has been applied in many research fields. However, it presents several limitations in certain occasions because of its ambiguous mathematical meaning. As a consequence, different metrics have been proposed instead, aimed at reducing the limitations introduced. In the following, we report three different ACD detectors based on the most common similarity measures adopted in HSI based on spectral correlation.

2.2.2.1 Spectral Angle Mapper (SAM) based ACD (SAM-ACD)

Given the pixel pair $\mathbf{y}(i,j)$ and $\mathbf{z}(i,j)$, the Spectral Angle Mapper (SAM, [59]) considers the following observation $\mathbf{e}(i,j)$:

$$\mathbf{e}(i,j)=[\mathbf{y}(i,j),\mathbf{z}(i,j)] \tag{2.7}$$

According to (2.7), $\mathbf{e}(i,j)$ is an $L\times 2$ array in the spatial position (i,j), i.e. $\mathbf{e}(i,j)=[\mathbf{e}_1(i,j),\mathbf{e}_2(i,j)]$. The SAM detector computes a hyper-angle between different spectral components of the observation $\mathbf{e}(i,j)$:

$$T_{SAM}(i,j)=\arccos\left(\frac{\mathbf{e}_1(i,j)\cdot\mathbf{e}_2(i,j)}{\|\mathbf{e}_1(i,j)\|_2\cdot\|\mathbf{e}_2(i,j)\|_2}\right) \tag{2.8}$$

Since the SAM is a similarity metric based on a angular measure, it is robust to changes in illumination of the scene. In fact, the difference between $\mathbf{e}_1(i,j)$ and $\mathbf{e}_2(i,j)$, corresponding to the two spectra $\mathbf{y}(i,j)$ and $\mathbf{z}(i,j)$ (referring to the same region of the scene collected at different times in potentially different illumination conditions) only modifies its magnitude, while the direction of the vectors does not change. In particular, the more similar are the compared spectra, the smaller is the spectral angle. The SAM detector ranges in values from 0, when $\mathbf{e}_1(i,j)$ and $\mathbf{e}_2(i,j)$ have the same direction, to $\pi/2$ when $\mathbf{e}_1(i,j)$ and $\mathbf{e}_2(i,j)$ have orthogonal direction. The detector (2.8) will be referred to as SAM-ACD, hereinafter.

2.2.2.2 Pearsonian Correlation Coefficient (PCC) based ACD (PCC-ACD)

A derivative of the SAM is the Pearsonian Correlation Coefficient (PCC, [43]) which is able to distinguish between positive and negative correlations. The PCC, which considers the same observation $\mathbf{e}(i,j)$ as in the SAM-ACD, is defined as:

$$T_{PCC}(i,j) = \arccos\left(\frac{\left(\mathbf{e}_1(i,j) - \boldsymbol{\mu}_y\right) \cdot \left(\mathbf{e}_2(i,j) - \boldsymbol{\mu}_z\right)}{\left\| \left(\mathbf{e}_1(i,j) - \boldsymbol{\mu}_y\right) \right\|_2 \cdot \left\| \left(\mathbf{e}_2(i,j) - \boldsymbol{\mu}_z\right) \right\|_2} \right) \tag{2.9}$$

where $\boldsymbol{\mu}_y$ and $\boldsymbol{\mu}_z$ are the average spectra of the test image and the reference image, respectively:

$$\begin{aligned} \boldsymbol{\mu}_y &= \frac{1}{N_S \cdot N_L} \sum_{i=1}^{N_S} \sum_{j=1}^{N_L} \mathbf{y}(i,j) \\ \boldsymbol{\mu}_z &= \frac{1}{N_S \cdot N_L} \sum_{i=1}^{N_S} \sum_{j=1}^{N_L} \mathbf{z}(i,j) \end{aligned} \tag{2.10}$$

As in the SAM-ACD, the more similar are the compared spectra, the smaller is the spectral angle. The PCC detector ranges in values from 0, when $\mathbf{e}_1(i,j)$ and $\mathbf{e}_2(i,j)$ have the same direction, to π when $\mathbf{e}_1(i,j)$ and $\mathbf{e}_2(i,j)$ have opposite direction. The detector (2.9) will be referred to as PCC-ACD, hereinafter.

2.2.2.3 Spectral Correlation Mapper (SCM) based ACD (SCM-ACD)

Since SAM-ACD is unable to detect negatively correlated data, the Spectral Correlation Mapper (SCM, [19]) is designed in order to correct these limitations. The SCM method adopts Pearson's correlation, though preserving the SAM characteristic of minimizing the shading effect. It is defined as:

$$T_{SCM}(i,j) = \arccos\left(\frac{\left(\mathbf{e}_1(i,j) - \boldsymbol{\mu}_y\right) \cdot \left(\mathbf{e}_2(i,j) - \boldsymbol{\mu}_y\right)}{\left\| \left(\mathbf{e}_1(i,j) - \boldsymbol{\mu}_y\right) \right\|_2 \cdot \left\| \left(\mathbf{e}_2(i,j) - \boldsymbol{\mu}_y\right) \right\|_2} \right) \tag{2.11}$$

where the observation $\mathbf{e}(i,j)$ is the same as in the SAM-ACD and PCC-ACD cases, and $\boldsymbol{\mu}_y$ is the average spectra of the test image, evaluated according to (2.10). The detector (2.11) will be referred to as SCM-ACD, hereinafter.

2.3 Statistical methods

In this section, the focus is on ACD algorithms based on statistical methods. In this context, the detection strategies are formulated by resorting to a binary hypothesis-testing problem solved according to decision rules typical of the detection theory. The foundation of ACD approaches is given by the Neyman-Pearson criterion (NP), according to which the optimum decision strategy is given by a Likelihood Ratio Test (LRT) dependent on the probability density functions (PDFs) conditioned to the two hypotheses [56].

In particular, we assume that $\mathbf{e}(i,j)$ is a multivariate Gaussian distributed random vector (RV) with mean value $\boldsymbol{\mu}_0$ and covariance matrix $\boldsymbol{\Gamma}_0$ under the hypothesis H_0, and with mean value $\boldsymbol{\mu}_1$ and covariance matrix $\boldsymbol{\Gamma}_1$ under the hypothesis H_1. Thus, we have:

$$\begin{aligned} &\mathbf{e}(i,j)|H_0 \in N(\boldsymbol{\mu}_0, \boldsymbol{\Gamma}_0) \\ &\mathbf{e}(i,j)|H_1 \in N(\boldsymbol{\mu}_1, \boldsymbol{\Gamma}_1) \end{aligned} \tag{2.12}$$

Since no decision cost and no prior information about the likelihood of each hypothesis is available, the decision problem in (2.12) can be solved using the NP approach. Accordingly, the decision strategy is based on the LR $\Lambda(i,j)$, i.e. the ratio between the PDF of the observation vector conditioned to the two hypotheses:

$$\Lambda(i,j) = \frac{p(\mathbf{e}(i,j)|H_1)}{p(\mathbf{e}(i,j)|H_0)} \underset{H_0}{\overset{H_1}{\gtrless}} \lambda_G \tag{2.13}$$

Depending on the assumptions of the statistical distributions of the observation $\mathbf{e}(i,j)$ conditioned to the hypotheses H_0 and H_1, in the following paragraphs two distinctive classes of statistical ACD detectors will be derived based on the decision strategy (2.13).

The first approach derives a simplified LRT decision rule. Specifically, the ACD strategy involves thresholding the background log-likelihood and, thus, only needs the specification of the background PDF to detect the anomalous changes occurred in the

observed scene [56]. The second approach takes into account the statistical independence between corresponding pixel vectors, leading to a different decision strategy [34]. In both cases, the parameters of the underlying PDFs are unknown and have to be estimated from the data themselves, leading to different ACD algorithms, as described in the next paragraph .

2.3.1 ACD based on quadratic detectors

In equation (2.13), all the parameters of the conditional PDFs are supposed known. Dealing with ACD problems such an assumption is not always satisfied. In particular $\boldsymbol{\mu}_1$, which is related to the potential change occurred, is generally not a-priori known. For this reason, a suboptimal decision strategy is exploited by resorting to the so-called Generalized Likelihood Ratio Test (GLRT), in which the ML estimate $\hat{\boldsymbol{\mu}}_1$ of $\boldsymbol{\mu}_1$ obtained from the observed data is adopted instead than its real value. This approach leads to the following decision rule:

$$\Lambda_G(i,j) = \frac{\max_{\boldsymbol{\mu}_1}\left(p\left(\mathbf{e}(i,j)\middle|H_1,\boldsymbol{\mu}_1,\boldsymbol{\Gamma}_1\right)\right)}{p\left(\mathbf{e}(i,j)\middle|H_0\right)} \underset{H_0}{\overset{H_1}{\gtrless}} \lambda_G \tag{2.14}$$

where the ML estimate $\hat{\boldsymbol{\mu}}_1 = \arg\max_{\boldsymbol{\mu}_1}\left(p\left(\mathbf{e}(i,j)\middle|H_1,\boldsymbol{\mu}_1,\boldsymbol{\Gamma}_1\right)\right)$ is employed in the numerator of equation (2.14). According to (2.12), the GLRT in (2.14) becomes:

$$\Lambda_G(i,j) = \frac{\left|\boldsymbol{\Gamma}_1\right|^{1/2}}{\left|\boldsymbol{\Gamma}_0\right|^{1/2}} \exp\left(-\frac{1}{2}\left(\mathbf{e}(i,j)-\boldsymbol{\mu}_0\right)^T \boldsymbol{\Gamma}_0^{-1}\left(\mathbf{e}(i,j)-\boldsymbol{\mu}_0\right)\right)^{-1} \underset{H_0}{\overset{H_1}{\gtrless}} \lambda_G \tag{2.15}$$

In (2.15), the ratio $\frac{\left|\boldsymbol{\Gamma}_1\right|^{1/2}}{\left|\boldsymbol{\Gamma}_0\right|^{1/2}}$ is always positive and can be included in the threshold λ_G. Moreover, the GLRT can be reformulated by taking the logarithm of $\Lambda_G(i,j)$ as:

$$\left(\mathbf{e}(i,j)-\boldsymbol{\mu}_0\right)^T \boldsymbol{\Gamma}_0^{-1}\left(\mathbf{e}(i,j)-\boldsymbol{\mu}_0\right) \underset{H_0}{\overset{H_1}{\gtrless}} \lambda \tag{2.16}$$

Notice that in deriving equation (2.16), we assume that the parameters $\boldsymbol{\mu}_0$ and $\boldsymbol{\Gamma}_0$ are known. In practice, such an assumption is unlikely to be met and such parameters are generally estimated by exploiting a set of secondary data, i.e. a set of observations from independent and identically distributed random vectors characterized by the same PDF as $\left(\mathbf{e}(i,j)\right)|H_0$. Thus, $\boldsymbol{\Gamma}_0$ and $\boldsymbol{\mu}_0$ are generally replaced with their ML estimates $\hat{\boldsymbol{\Gamma}}_0$ and $\hat{\boldsymbol{\mu}}_0$ from the secondary data. The resulting detector assumes the form:

$$T(i,j)=\left(\mathbf{e}(i,j)-\hat{\boldsymbol{\mu}}_0\right)^T \hat{\boldsymbol{\Gamma}}_0^{-1}\left(\mathbf{e}(i,j)-\hat{\boldsymbol{\mu}}_0\right) \underset{H_0}{\overset{H_1}{\gtrless}} \lambda \tag{2.17}$$

where the ACD statistic $T(i,j)$ is the Mahalanobis distance between the observed vector and the statistical distribution in the no change hypothesis.

The detection rule (2.17) can be used to derive different detectors modifying the observation vector $\mathbf{e}(i,j)$ and/or the secondary data used to estimate the background parameters $\boldsymbol{\Gamma}_0$ and $\boldsymbol{\mu}_0$. Interestingly, in the next two sub-paragraphs we show that the Simple Subtraction based detector in [34] and the Straight RX Anomaly Detector in [87] can be explained as special cases of the detection rule (2.17). Hereinafter, they will be referred to as the Difference Vector (DV) based and the Joint Vector (JV) based detectors, respectively.

2.3.1.1 Difference Vector (DV) based ACD (DV-ACD)

In the DV based approach, the observation space is obtained by subtracting the two images pixel by pixel. Thus, the observation vector $\mathbf{e}(i,j)$ is given by:

$$\mathbf{e}(i,j)=\mathbf{y}(i,j)-\mathbf{z}(i,j) \tag{2.18}$$

Because, under the hypothesis H_0, $\mathbf{y}(i,j)$ and $\mathbf{z}(i,j)$ have the same mean value, we let $\hat{\boldsymbol{\mu}}_0 = 0$ in (2.17). Furthermore, all the image pixels are used as secondary data to compute $\hat{\boldsymbol{\Gamma}}_0$:

$$\hat{\boldsymbol{\Gamma}}_0 = \frac{1}{N_S \cdot N_L} \sum_{i=1}^{N_S} \sum_{j=1}^{N_L} \mathbf{e}(i,j) \cdot \mathbf{e}(i,j)^T \tag{2.19}$$

Consequently, equation (2.17) becomes:

$$T_{DV}(i,j) = \mathbf{e}(i,j)^T \hat{\boldsymbol{\Gamma}}_0^{-1} \mathbf{e}(i,j) \underset{H_0}{\overset{H_1}{\gtrless}} \lambda \tag{2.20}$$

The detector (2.20) will be referred to as DV-ACD, hereinafter.

2.3.1.2 Joint Vector (JV) based ACD (JV-ACD)

In the JV data model, the observation vector is given by:

$$\mathbf{e}(i,j) = \begin{bmatrix} \mathbf{y}(i,j) \\ \mathbf{z}(i,j) \end{bmatrix} \tag{2.21}$$

In this case, the pixels from the two images are assumed to be realizations of two joint multivariate Gaussian vectors. Thus, $\mathbf{e}(i,j) | H_0$ is a realization of a Gaussian RV with the mean $\boldsymbol{\mu}_0$ and covariance matrix $\boldsymbol{\Gamma}_0$ given by:

$$\boldsymbol{\mu}_0 = \begin{bmatrix} \boldsymbol{\mu}_y \\ \boldsymbol{\mu}_z \end{bmatrix} \qquad \boldsymbol{\Gamma}_0 = \begin{bmatrix} \boldsymbol{\Gamma}_y & \boldsymbol{\Gamma}_{yz} \\ \boldsymbol{\Gamma}_{yz}^T & \boldsymbol{\Gamma}_z \end{bmatrix} \tag{2.22}$$

where $\boldsymbol{\mu}_y$ ($\boldsymbol{\mu}_z$) and $\boldsymbol{\Gamma}_y$ ($\boldsymbol{\Gamma}_z$) are the mean vector and the covariance matrix of the test image (reference image), respectively, while $\boldsymbol{\Gamma}_{yz}$ is the cross-covariance matrix between the two images.

According to (2.17), the detector associated to the JV data model is:

$$T_{JV}(i,j)=\left(\mathbf{e}(i,j)-\hat{\boldsymbol{\mu}}_0\right)^T\hat{\boldsymbol{\Gamma}}_0^{-1}\left(\mathbf{e}(i,j)-\hat{\boldsymbol{\mu}}_0\right)\underset{H_0}{\overset{H_1}{\gtrless}}\lambda \tag{2.23}$$

where $\hat{\boldsymbol{\mu}}_0$ and $\hat{\boldsymbol{\Gamma}}_0$ represent the ML estimates of $\boldsymbol{\mu}_0$ and $\boldsymbol{\Gamma}_0$, respectively:

$$\hat{\boldsymbol{\mu}}_0=\begin{bmatrix}\hat{\boldsymbol{\mu}}_y\\ \hat{\boldsymbol{\mu}}_z\end{bmatrix}\qquad \hat{\boldsymbol{\Gamma}}_0=\begin{bmatrix}\hat{\boldsymbol{\Gamma}}_y & \hat{\boldsymbol{\Gamma}}_{yz}\\ \hat{\boldsymbol{\Gamma}}_{yz}^T & \hat{\boldsymbol{\Gamma}}_z\end{bmatrix} \tag{2.24}$$

Such parameters are obtained using all the pixels in the joint image as secondary data:

$$\begin{aligned}
&\hat{\boldsymbol{\mu}}_y=\frac{1}{N_S\cdot N_L}\sum_{i=1}^{N_S}\sum_{j=1}^{N_L}\mathbf{y}(i,j)\quad \hat{\boldsymbol{\Gamma}}_y=\frac{1}{N_S\cdot N_L}\sum_{i=1}^{N_S}\sum_{j=1}^{N_L}\mathbf{y}(i,j)\cdot\mathbf{y}(i,j)^T-\hat{\boldsymbol{\mu}}_y\cdot\hat{\boldsymbol{\mu}}_y^T\\
&\hat{\boldsymbol{\mu}}_z=\frac{1}{N_S\cdot N_L}\sum_{i=1}^{N_S}\sum_{j=1}^{N_L}\mathbf{z}(i,j)\quad \hat{\boldsymbol{\Gamma}}_z=\frac{1}{N_S\cdot N_L}\sum_{i=1}^{N_S}\sum_{j=1}^{N_L}\mathbf{z}(i,j)\cdot\mathbf{z}(i,j)^T-\hat{\boldsymbol{\mu}}_z\cdot\hat{\boldsymbol{\mu}}_z^T\\
&\hat{\boldsymbol{\Gamma}}_{yz}=\frac{1}{N_S\cdot N_L}\sum_{i=1}^{N_S}\sum_{j=1}^{N_L}\mathbf{y}(i,j)\cdot\mathbf{z}(i,j)^T-\hat{\boldsymbol{\mu}}_y\cdot\hat{\boldsymbol{\mu}}_z^T
\end{aligned} \tag{2.25}$$

The detector in (2.24) will be referred to as JV-ACD, hereinafter.

2.3.2 ACD based on elliptically contoured distributions (EC-ACD)

The DV-ACD and JV-ACD algorithms have been derived by assuming the multivariate global Gaussian model. In some applications ([91],[92]) it has been observed that the data distributions have heavier tails than the Gaussian model. Thus, for those applications, the use of heavy tails statistical models has been investigated. Particularly, the class of Elliptically Contoured (EC) distributions has been considered. In [91] the use of the EC distributions has been investigated also for ACD applications. Specifically, the authors considered the EC-t distribution model.

In this section we show that the general form of the detector in (2.17) can be obtained also by assuming the EC-t (multivariate Student) distribution model for both the hypotheses. The PDF of the observation $\mathbf{e}(i,j)$ conditioned to the two hypotheses are:

$$\begin{aligned}&\mathbf{e}(i,j)|H_0 \in St(\mathbf{e}(i,j),\boldsymbol{\mu}_0,\boldsymbol{\Gamma}_0,\nu_0)\\&\mathbf{e}(i,j)|H_1 \in St(\mathbf{e}(i,j),\boldsymbol{\mu}_1,\boldsymbol{\Gamma}_1,\nu_1)\end{aligned} \tag{2.26}$$

where

$$St(\mathbf{e},\boldsymbol{\mu},\Gamma,\nu)=\frac{\Gamma\left(\frac{L+\nu}{2}\right)}{\Gamma\left(\frac{\nu}{2}\right)\cdot(\nu-2)^{L/2}\cdot(\pi)^{L/2}|\boldsymbol{\Gamma}|^{1/2}}\left(1+\frac{1}{\nu-2}(\mathbf{e}(i,j)-\boldsymbol{\mu})^T\boldsymbol{\Gamma}^{-1}(\mathbf{e}(i,j)-\boldsymbol{\mu})\right)^{-\frac{L+\nu}{2}} \tag{2.27}$$

is the EC-t PDF of the RV $\mathbf{e}$ having size equal to L, with mean vector $\boldsymbol{\mu}$, covariance matrix $\boldsymbol{\Gamma}$ and ν degrees of freedom. Following the same reasoning as that in section II, we can express the GLRT with respect to the parameter $\boldsymbol{\mu}_1$ as:

$$\Lambda_G(i,j)=\frac{\max_{\boldsymbol{\mu}_1}\left(St(\mathbf{e}(i,j)|H_1,\boldsymbol{\mu}_1)\right)}{St(\mathbf{e}(i,j)|H_0)}\underset{H_0}{\overset{H_1}{\gtrless}}\lambda_G \tag{2.28}$$

where the ML estimate $\hat{\boldsymbol{\mu}}_1=\arg\max_{\boldsymbol{\mu}_1}\left(p(\mathbf{e}(i,j)|H_1,\boldsymbol{\mu}_1,\mathbf{R}_1,\nu_1)\right)$ is employed in the numerator of equation (2.28). According to the assumed distribution model for both the hypotheses, the GLRT in (2.28) becomes:

$$\Lambda_G(i,j)=\frac{\Gamma\left(\frac{L+\nu_1}{2}\right)\Gamma\left(\frac{\nu_0}{2}\right)}{\Gamma\left(\frac{L+\nu_0}{2}\right)\Gamma\left(\frac{\nu_1}{2}\right)}\frac{\left(\frac{\nu_0-2}{\nu_1-2}\right)^{L/2}\frac{|\boldsymbol{\Gamma}_0|^{1/2}}{|\boldsymbol{\Gamma}_1|^{1/2}}}{\left(1+\frac{1}{\nu_0-2}(\mathbf{e}(i,j)-\boldsymbol{\mu}_0)^T\boldsymbol{\Gamma}_0^{-1}(\mathbf{e}(i,j)-\boldsymbol{\mu}_0)\right)^{-\frac{L+\nu_0}{2}}}\underset{H_0}{\overset{H_1}{\gtrless}}\lambda_G \tag{2.29}$$

Considering that the ratio $\frac{\Gamma\left(\frac{L+\nu_1}{2}\right)\Gamma\left(\frac{\nu_0}{2}\right)}{\Gamma\left(\frac{L+\nu_0}{2}\right)\Gamma\left(\frac{\nu_1}{2}\right)}\left(\frac{\nu_0-2}{\nu_1-2}\right)^{L/2}\frac{|\boldsymbol{\Gamma}_0|^{1/2}}{|\boldsymbol{\Gamma}_1|^{1/2}}$ is greater than zero, it can be included in the threshold λ_G, and the GLRT can be reformulated as:

$$\left(1+\frac{1}{\nu_0-2}(\mathbf{e}(i,j)-\boldsymbol{\mu}_0)^T\boldsymbol{\Gamma}_0^{-1}(\mathbf{e}(i,j)-\boldsymbol{\mu}_0)\right)^{\frac{L+\nu_0}{2}} \underset{H_0}{\overset{H_1}{\gtrless}} \lambda^* \tag{2.30}$$

Now, noting that the function at the left side of the inequality is monotonically non-decreasing, equation (2.30) can be rewritten as:

$$(\mathbf{e}(i,j)-\boldsymbol{\mu}_0)^T\boldsymbol{\Gamma}_0^{-1}(\mathbf{e}(i,j)-\boldsymbol{\mu}_0) \underset{H_0}{\overset{H_1}{\gtrless}} \lambda \tag{2.31}$$

where $\lambda=\left[\left(\lambda^*\right)^{\frac{2}{L+\nu_0}}-1\right]\cdot(\nu_0-2)$. As in the Gaussian model case considered in the previous section, being $\boldsymbol{\mu}_0$ and $\boldsymbol{\Gamma}_0$ not a priory known, they are replaced by their ML estimate $\hat{\boldsymbol{\Gamma}}_0$ and $\hat{\boldsymbol{\mu}}_0$ from the secondary data. The resulting detector becomes:

$$T_{EC}(i,j)=(\mathbf{e}(i,j)-\hat{\boldsymbol{\mu}}_0)^T\hat{\boldsymbol{\Gamma}}_0^{-1}(\mathbf{e}(i,j)-\hat{\boldsymbol{\mu}}_0) \underset{H_0}{\overset{H_1}{\gtrless}} \lambda \tag{2.32}$$

which is exactly the same expression as that reported in (2.17).

2.3.3 Hyperbolic ACD (H-ACD)

The JV-ACD detector described above does not distinguish between the case when $\mathbf{y}(i,j)$ or $\mathbf{z}(i,j)$ might be individually anomalous and the case when it is the change between $\mathbf{y}(i,j)$ and $\mathbf{z}(i,j)$ that is anomalous. In order to overcome this drawback, a new method has been proposed in [44]. It considers the observation model (2.21), where the pixels from the two images are assumed to be realizations of two joint multivariate Gaussian vectors. In particular, $\mathbf{e}(i,j)|H_0$ is modelled as a realization of a Gaussian RV with zero mean and covariance matrix $\boldsymbol{\Gamma}_0$, while $\mathbf{e}(i,j)|H_1$ is modelled as a realization of a Gaussian RV with zero mean and covariance matrix $\boldsymbol{\Gamma}_1$. Moreover, under the hypothesis H_0, $\mathbf{y}(i,j)$ and $\mathbf{z}(i,j)$ are supposed to be realizations of jointly Gaussian correlated RVs, while under the hypothesis H_1, $\mathbf{y}(i,j)$ and $\mathbf{z}(i,j)$ are supposed to be

realizations of jointly Gaussian uncorrelated RVs. As a consequence, referring to the notation introduced in (2.22), we have:

$$\mathbf{\Gamma}_0 = \begin{bmatrix} \mathbf{\Gamma}_y & \mathbf{\Gamma}_{yz} \\ \mathbf{\Gamma}_{yz}^T & \mathbf{\Gamma}_z \end{bmatrix} \qquad \mathbf{\Gamma}_1 = \begin{bmatrix} \mathbf{\Gamma}_y & 0 \\ 0 & \mathbf{\Gamma}_z \end{bmatrix} \tag{2.33}$$

where, under the hypothesis H_0, the covariance matrix $\mathbf{\Gamma}_0$ has the same expression as in the JV-ACD, while under the hypothesis H_1 the cross-covariance matrix $\mathbf{\Gamma}_{yz}$ of $\mathbf{\Gamma}_1$ is equal to zero. Notice that the hypothesis $\boldsymbol{\mu}_0 = \boldsymbol{\mu}_1 = 0$ can be achieved by first computing the mean spectrum for each image, and successively subtracting that mean from each pixel in each image.

Consequently, the LR in (2.13) becomes:

$$\Lambda(i,j) = \frac{|\mathbf{\Gamma}_0|^{1/2}}{|\mathbf{\Gamma}_1|^{1/2}} \frac{\exp\left(-\frac{1}{2}\mathbf{e}(i,j)^T \mathbf{\Gamma}_1^{-1}\mathbf{e}(i,j)\right)}{\exp\left(-\frac{1}{2}\mathbf{e}(i,j)^T \mathbf{\Gamma}_0^{-1}\mathbf{e}(i,j)\right)} \underset{H_0}{\overset{H_1}{\gtrless}} \lambda_G \tag{2.34}$$

In (2.15), the ratio $\frac{|\mathbf{\Gamma}_0|^{1/2}}{|\mathbf{\Gamma}_1|^{1/2}}$ is always positive and can be included in the threshold λ_G. The LR can be therefore reformulated by taking the logarithm of $\Lambda(i,j)$ as:

$$\mathbf{e}(i,j)^T \cdot \mathbf{\Gamma}_d \cdot \mathbf{e}(i,j) \underset{H_0}{\overset{H_1}{\gtrless}} \lambda \tag{2.35}$$

where we have denoted $\mathbf{\Gamma}_d = \mathbf{\Gamma}_0^{-1} - \mathbf{\Gamma}_1^{-1}$. According to the decision rule (2.35), the observation $\mathbf{e}(i,j)$ is considered an anomalous change only if $p(\mathbf{e}(i,j))$ is small and $p(\mathbf{y}(i,j))$ and $p(\mathbf{z}(i,j))$ are relatively large. That is, $\mathbf{y}(i,j)$ and $\mathbf{z}(i,j)$ are individually normal, but their relationship is unusual.

Notice that in deriving equation (2.35), we assume that $\mathbf{\Gamma}_d$ is known. In practice, such an assumption is unlikely to be met and such parameter is replaced with its ML estimate $\hat{\mathbf{\Gamma}}_d$ from the secondary data. Therefore, the resulting detector becomes:

$$T_H(i,j) = \mathbf{e}(i,j)^T \cdot \hat{\boldsymbol{\Gamma}}_d \cdot \mathbf{e}(i,j) \underset{H_0}{\overset{H_1}{\gtrless}} \lambda \tag{2.36}$$

where we have denoted with $\hat{\boldsymbol{\Gamma}}_d = \hat{\boldsymbol{\Gamma}}_0^{-1} - \hat{\boldsymbol{\Gamma}}_1^{-1}$, and $\hat{\boldsymbol{\Gamma}}_0$ and $\hat{\boldsymbol{\Gamma}}_1$ are the ML estimates of $\boldsymbol{\Gamma}_0$ and $\boldsymbol{\Gamma}_1$, respectively:

$$\hat{\boldsymbol{\Gamma}}_0 = \begin{bmatrix} \hat{\boldsymbol{\Gamma}}_y & \hat{\boldsymbol{\Gamma}}_{yz} \\ \hat{\boldsymbol{\Gamma}}_{yz}^T & \hat{\boldsymbol{\Gamma}}_z \end{bmatrix} \qquad \hat{\boldsymbol{\Gamma}}_1 = \begin{bmatrix} \hat{\boldsymbol{\Gamma}}_y & 0 \\ 0 & \hat{\boldsymbol{\Gamma}}_z \end{bmatrix} \tag{2.37}$$

Such parameters are obtained using all the pixels in the joint image as secondary data:

$$\begin{aligned} \hat{\boldsymbol{\Gamma}}_y &= \frac{1}{N_S \cdot N_L} \sum_{i=1}^{N_S} \sum_{j=1}^{N_L} \mathbf{y}(i,j) \cdot \mathbf{y}(i,j)^T \\ \hat{\boldsymbol{\Gamma}}_z &= \frac{1}{N_S \cdot N_L} \sum_{i=1}^{N_S} \sum_{j=1}^{N_L} \mathbf{z}(i,j) \cdot \mathbf{z}(i,j)^T \\ \hat{\boldsymbol{\Gamma}}_{yz} &= \frac{1}{N_S \cdot N_L} \sum_{i=1}^{N_S} \sum_{j=1}^{N_L} \mathbf{y}(i,j) \cdot \mathbf{z}(i,j)^T \end{aligned} \tag{2.38}$$

Note that $\boldsymbol{\Gamma}_d$, or equivalently its estimate $\hat{\boldsymbol{\Gamma}}_d$ is not a positive-definite matrix; it has negative as well as positive eigenvalues, and the boundaries of constant values in equation (2.36) are hyperbolic, not elliptical. For this reason, the detector (2.36) is referred to as Hyperbolic ACD (H-ACD).

2.3.4 Hyperbolic EC-ACD (H-EC-ACD)

Similarly to the extension provided in section 2.3.2, in [32] the same class of EC-t distribution reported in (2.26) has been assumed for modelling both the hypotheses H_0 and H_1 in the H-ACD approach, leading to a closed-form expression of the related LR. In particular, the PDF of the observation $\mathbf{e}(i,j)$ conditioned to the two hypotheses are:

$$\begin{aligned} &\mathbf{e}(i,j) | H_0 \in St(\mathbf{e}(i,j), 0, \boldsymbol{\Gamma}_0, \nu) \\ &\mathbf{e}(i,j) | H_1 \in St(\mathbf{e}(i,j), 0, \boldsymbol{\Gamma}_1, \nu) \end{aligned} \tag{2.39}$$

where under the hypothesis H_0, $\mathbf{e}(i,j)$ is a $L\times 1$ EC-t distributed RV, with zero mean vector, covariance matrix $\boldsymbol{\Gamma}_0$ and ν degrees of freedom, while under the hypothesis H_1, $\mathbf{e}(i,j)$ is EC-t distributed, with zero mean vector, covariance matrix $\boldsymbol{\Gamma}_1$ and ν degrees of freedom. Following the decision strategy (2.13), we can express the LR with respect to the PDF distributions (2.40) as:

$$\Lambda(i,j)=\frac{St\left(\mathbf{e}(i,j)|H_1\right)}{St\left(\mathbf{e}(i,j)|H_0\right)}\underset{H_0}{\overset{H_1}{\gtrless}}\lambda \tag{2.40}$$

By substituting the above multivariate EC-t form into (2.28) and dropping unimportant additive constants, the expression for the ACD detector becomes:

$$\frac{\nu-2+\mathbf{e}(i,j)^T\boldsymbol{\Gamma}_0^{-1}\mathbf{e}(i,j)}{\nu-2+\mathbf{e}(i,j)^T\boldsymbol{\Gamma}_1^{-1}\mathbf{e}(i,j)}\underset{H_0}{\overset{H_1}{\gtrless}}\lambda \tag{2.41}$$

Notice that in deriving equation (2.41), we assumed that $\boldsymbol{\Gamma}_0$ and $\boldsymbol{\Gamma}_1$ are known. In practice, such parameters are replaced with their ML estimates $\hat{\boldsymbol{\Gamma}}_0$ and $\hat{\boldsymbol{\Gamma}}_1$, from the secondary data evaluated according to (2.24), (2.25).

In addition, the decision rule (2.41) requires an estimate of ν as well. In [32], it has been found that a quick estimate of ν is obtained by taking a ratio of moments of the distribution of the observation vector $\mathbf{e}(i,j)$:

$$\hat{\nu}=2+\frac{\kappa_m}{\kappa_m-(2\cdot L+1)} \tag{2.42}$$

where $\kappa_m=\frac{E\{r^3\}}{\mu_r}$, r is the scalar magnitude of the whitened observed vector, i.e. $r=\sqrt{\mathbf{e}(i,j)^T\boldsymbol{\Gamma}^{-1}\mathbf{e}(i,j)}$ and μ_r and $E\{r^3\}$ are the first and the third order statistical moment, respectively.

Therefore, the resulting detector becomes:

$$T_{ECH}(i,j)=\frac{\hat{\nu}-2+\mathbf{e}(i,j)^T\hat{\mathbf{\Gamma}}_0^{-1}\mathbf{e}(i,j)}{\hat{\nu}-2+\mathbf{e}(i,j)^T\hat{\mathbf{\Gamma}}_1^{-1}\mathbf{e}(i,j)}\underset{H_0}{\overset{H_1}{\gtrless}}\lambda \tag{2.43}$$

which extends the H-ACD detector to the case of EC-t distributed observation model.

2.4 Dealing with mis-registration errors (LCRA-ACD)

It is important to point out that in the previous sections we assumed that the images have been perfectly co-registered. When images are collected by airborne platforms, perfect co-registration is very difficult to achieve, and therefore a residual mis-registration (RMR) error should be taken into account in developing ACD strategies. The RMR can be viewed as a per-pixel shift in both line and sample directions, whose magnitude is typically in the order of a few pixels. It has been shown [Ref4] that the RMR is detrimental for pixel-based ACD algorithms, because it leads to a detection performance loss increasing with its magnitude.

Recently, the Local Co-Registration Adjustment (LCRA, [Ref5]) approach has been proposed to cope with the performance degradation problem due to RMR, improving the results in ACD tasks. The LCRA approach embeds the a priori knowledge on the magnitude of the RMR on the pixel based CD scheme. In order to reduce the effects due to RMR, in the LCRA approach one compares the pixel vector in position (i,j) of the test image with those belonging to a given neighbourhood of the coordinates (i,j) in the reference image.

Such a neighbourhood is selected by means of an uncertainty window W_R whose size has to be tailored to the magnitude of the RMR ([Ref7]). In accordance with the LCRA approach, the statistic adopted by a given ACD detector assumes the following general form:

$$T_{LCRA}(i,j)=\min_{(r,p)\in W_R}\left(\widetilde{T}(i,j,r,p)\right) \tag{2.44}$$

The following example provides a motivation for the LCRA approach. Let us assume that the changes of interest are represented by deletions, i.e. objects present in the test image and non present in the reference image (the discussion will be further generalized to all kind of changes contemplated by the hypothesis H_1). If the observed vector in position (i,j) really represents a change, then $\mathbf{y}(i,j)$ should differ not only from $\mathbf{z}(i,j)$, but also from its neighbours. On the contrary, if $\mathbf{y}(i,j)$ only seems to be a change, due to mis-registration error, then at least one of the neighbours of $\mathbf{z}(i,j)$, belonging to W_R, should be similar to $\mathbf{y}(i,j)$. According to (2.44), given the generic position (i,j), T_{LCRA} assigns the lowest anomalousness value resulting from the combination of $\mathbf{y}(i,j)$ with each of the vector $\mathbf{z}(i+r,j+p)$ belonging to W_R.

With reference to the deterministic approaches, the expression $\tilde{T}_E(i,j,r,p)$ of $\tilde{T}(i,j,r,p)$ in the case of the CVA-ACD becomes:

$$\begin{aligned}&\tilde{T}_E(i,j,r,p)=\left\|\tilde{\mathbf{e}}(i,j,r,p)\right\|_2\\&\tilde{\mathbf{e}}(i,j,r,p)=\mathbf{y}(i,j)-\mathbf{z}(i+r,j+p)\end{aligned} \tag{2.45}$$

As to the angular metrics in their LCRA versions, the particular form $\tilde{T}_{SAM}(i,j,r,p)$, for the SAM-ACD becomes:

$$\tilde{T}_{SAM}(i,j,r,p)=\arccos\left(\frac{\tilde{\mathbf{e}}_1(i,j,r,p)\cdot\tilde{\mathbf{e}}_2(i,j,r,p)}{\left\|\tilde{\mathbf{e}}_1(i,j,r,p)\right\|_2\cdot\left\|\tilde{\mathbf{e}}_2(i,j,r,p)\right\|_2}\right) \tag{2.46}$$

while the form $\tilde{T}_{PCC}(i,j,r,p)$ for the PCC-ACD becomes:

$$T_{PCC}(i,j)=\arccos\left(\frac{\left(\tilde{\mathbf{e}}_1(i,j,r,p)-\boldsymbol{\mu}_y\right)\cdot\left(\tilde{\mathbf{e}}_2(i,j,r,p)-\boldsymbol{\mu}_z\right)}{\left\|\left(\tilde{\mathbf{e}}_1(i,j,r,p)-\boldsymbol{\mu}_y\right)\right\|_2\cdot\left\|\left(\tilde{\mathbf{e}}_2(i,j,r,p)-\boldsymbol{\mu}_z\right)\right\|_2}\right) \tag{2.47}$$

and the form $\tilde{T}_{SCM}(i,j,r,p)$ assumed by $\tilde{T}(i,j,r,p)$ results in:

$$T_{SCM}(i,j)=\arccos\left(\frac{\left(\tilde{\mathbf{e}}_1(i,j,r,p)-\boldsymbol{\mu}_y\right)\cdot\left(\tilde{\mathbf{e}}_2(i,j,r,p)-\boldsymbol{\mu}_y\right)}{\left\|\left(\tilde{\mathbf{e}}_1(i,j,r,p)-\boldsymbol{\mu}_y\right)\right\|_2\cdot\left\|\left(\tilde{\mathbf{e}}_2(i,j,r,p)-\boldsymbol{\mu}_y\right)\right\|_2}\right) \tag{2.48}$$

where according to the LCRA, the observation vector in (2.46), (2.47) and (2.48) becomes $\tilde{\mathbf{e}}(i,j,r,p)=[\mathbf{y}(i,j),\mathbf{z}(i+r,j+p)]$.

Concerning the statistical approaches, $\tilde{T}(i,j,r,p)$ is related to the statistic adopted by the given detector. The modified version of the ACD algorithms proposed in the previous section can be designed according to the general form in (2.44) to handle the RMR. In particular, the expression $\tilde{T}_{DV}(i,j,r,p)$ of $\tilde{T}(i,j,r,p)$ in the case of the DV-ACD becomes:

$$\begin{aligned}&\tilde{T}_{DV}(i,j,r,p)=\tilde{\mathbf{e}}(i,j,r,p)^T\cdot\hat{\boldsymbol{\Gamma}}_0^{-1}\cdot\tilde{\mathbf{e}}(i,j,r,p)\\&\tilde{\mathbf{e}}(i,j,r,p)=\mathbf{y}(i,j)-\mathbf{z}(i+r,j+p)\end{aligned}\tag{2.49}$$

$\hat{\boldsymbol{\Gamma}}_0$ is globally estimated from all the difference image pixels and cannot be modified according to the LCRA approach. Thus, it is estimated from the secondary data by supposing the perfect co-registration between images, and then applied to every shifted version of the observation $\tilde{\mathbf{e}}(i,j,k,l)$ according to the decision rule. In addition, the possibility to estimate $\boldsymbol{\Gamma}_0$ for every shifted version of the test and reference images would incorrectly result in the assumption that the same fixed RMR affects all the corresponding image pixels. Despite the inaccuracy in the estimation of $\boldsymbol{\Gamma}_0$ due to the RMR, the improvement yielded by the LCRA approach in the DV and JV observation models is very effective, as it will be shown in the experimental results section.

As to the JV-ACD, in its LCRA version, the particular form $\tilde{T}_{JV}(i,j,r,p)$ assumed by $\tilde{T}(i,j,r,p)$ is:

$$\begin{aligned}&\tilde{T}_{JV}(i,j,r,p)=(\tilde{\mathbf{e}}(i,j,r,p)-\hat{\boldsymbol{\mu}}_0)^T\cdot\hat{\boldsymbol{\Gamma}}_0^{-1}\cdot(\tilde{\mathbf{e}}(i,j,r,p)-\hat{\boldsymbol{\mu}}_0)\\&\tilde{\mathbf{e}}(i,j,r,p)=\begin{bmatrix}\mathbf{y}(i,j)\\\mathbf{z}(i+r,j+p)\end{bmatrix}\end{aligned}\tag{2.50}$$

Also in this case, being $\hat{\boldsymbol{\Gamma}}_0$ and $\hat{\boldsymbol{\mu}}_0$ obtained globally from all the pixels of the joint image, their values do not change when we use the LCRA approach, i.e. their values are those obtained by assuming perfectly co-registered images.

Finally, the H-ACD in its LCRA version $\tilde{T}_H(i,j,r,p)$ becomes:

$$\begin{aligned}\widetilde{T}_H(i,j,r,p) &= \widetilde{\mathbf{e}}(i,j,r,p)^T \cdot \hat{\mathbf{\Gamma}}_d^{-1} \cdot \widetilde{\mathbf{e}}(i,j,r,p) \\ \widetilde{\mathbf{e}}(i,j,r,p) &= \begin{bmatrix} \mathbf{y}(i,j) \\ \mathbf{z}(i+r,j+p) \end{bmatrix}\end{aligned} \tag{2.51}$$

where the same considerations regarding $\hat{\mathbf{\Gamma}}_0$ and $\hat{\boldsymbol{\mu}}_0$ as in the previous case also hold in this case.

Notice that, due to the asymmetric nature of the ACD problem, the LCRA approach would fail the detection of a change understood as the appearance of an object. Therefore, if the type of change is not a priori known, the LCRA approach can be generalized in order to include the different types of changes occurring, slightly reducing the performance, leading to the Symmetric LCRA (SLCRA):

$$T_{SLCRA}(i,j) = \max\left(\min_{(r,p)\in W_R} \left(\widetilde{T}(i,j,r,p)\right), \min_{(r,p)\in W_R} \left(\widetilde{T}^R(i,j,r,p)\right) \right) \tag{2.52}$$

where $\widetilde{T}^R(i,j,r,p)$ is the reverse detector of $\widetilde{T}(i,j,r,p)$ obtained by assuming $\mathbf{z}(i,j)$ as the test and $\mathbf{y}(i+r,j+p)$ as the reference pixel vector, respectively.

2.5 Radiometric compensation

As concerns the assumption about the two images are radiometric comparable, it is important to remark that its validity relies upon several factors. It depends on the specific platform (airborne or space-borne), the geometry of acquisition, as well as the spectral region being investigated. If the images are not radiometrically comparable, because of illumination or changes in atmospheric and environmental conditions from one acquisition to another, pervasive and uninteresting changes must be modelled and accounted for in developing ACD strategies. Several algorithms have been proposed in the past to cope with this problem. The Chronochrome method (CC, [36]), which represents the optimal linear mean square error predictor, provides a benchmark approach to transform the radiance signatures of the test image $\mathbf{Y}$ using the statistical

information of the co-registered image pair, making them suitable for the reference image $\mathbf{Z}$ collected at another time.

Unfortunately, if RMR affects the images, the use of such optimal predictor is not appropriate because it requires a perfect co-registration between images. As a consequence, a sub-optimal method should be adopted instead. In the literature, the Whitening/De-whitening (WD, [90]) technique has been proposed for transforming spectral signatures of targets viewed during multi-temporal monitoring in target detection applications. The WD performs a transformation by rotating, translating, and scaling the original HS image in order to obtain a transformed HS image having zero mean and a standard deviation of one for all the bands. Moreover, the transformed image cube has uncorrelated bands and unit covariance matrix. In CD applications, the same solution as WD is the Covariance Equalization (CE, [37]). Differently from CC, which relies upon a cross-covariance matrix for prediction, CE is based solely on the individual covariance matrices of the test and the reference images and is therefore less sensitive to RMR. In the following a theoretical derivation of the two methods is provided.

2.5.1 Chronochrome (CC) algorithm

The most popular algorithm for radiometric compensation in ACD applications when dealing with HSI is called Chronochrome (CC, [36]). CC derives from a linear model of the temporal development of collected spectra on the ground. It employs a linear version of the chromo-dynamics model for the prediction of the test image $\mathbf{Y}$ from the reference image $\mathbf{Z}$ using the statistical information of the co-registered image pair.

CC imposes an approximate colour constancy across times, in the sense of preserving all first- and second-order statistics, enabling the meaningful comparison of temporally separated spectral signatures. This mapping defines a spectral evolution operator, which can be exploited for translating target signatures from one set of environmental conditions to another. By requiring only first- and second-order hyperspectral statistics

to construct a linear transformation, CC defines a robust method of modelling atmospheric and other environmental effects that modify the apparent signature of every pixel.

In order to derive the CC predictor, let us consider the image pair $\mathbf{Y}$ and $\mathbf{Z}$, and let us also suppose that the two HSI are mean-centred (this assumption can be always achieved by subtracting the mean value from each image). A linear estimate of the generic pixel vector $\mathbf{y}(i,j)$ from $\mathbf{z}(i,j)$ is given by:

$$\hat{\mathbf{y}}(i,j) = \mathbf{L} \cdot \mathbf{z}(i,j) \tag{2.53}$$

equation (2.53) generates an associated error matrix $\mathbf{E}_m$ equal to:

$$\mathbf{E}_m = E\left\{\left(\mathbf{y}(i,j) - \mathbf{L} \cdot \mathbf{z}(i,j)\right) \cdot \left(\mathbf{y}(i,j) - \mathbf{L} \cdot \mathbf{z}(i,j)\right)^T\right\} \tag{2.54}$$

which can be rewritten as:

$$\begin{aligned}\mathbf{E}_m = E\Big\{&\left[\left(\mathbf{y}(i,j) - \boldsymbol{\Gamma}_{yz} \cdot \boldsymbol{\Gamma}_z^{-1} \cdot \mathbf{z}(i,j)\right) + \left(\boldsymbol{\Gamma}_{yz} \cdot \boldsymbol{\Gamma}_z^{-1} - \mathbf{L}\right) \cdot \mathbf{z}(i,j)\right] \times \\ &\left[\left(\mathbf{y}(i,j) - \boldsymbol{\Gamma}_{yz} \cdot \boldsymbol{\Gamma}_z^{-1} \cdot \mathbf{z}(i,j)\right) + \left(\boldsymbol{\Gamma}_{yz} \cdot \boldsymbol{\Gamma}_z^{-1} - \mathbf{L}\right) \cdot \mathbf{z}(i,j)\right]^T\Big\}\end{aligned} \tag{2.55}$$

where $\boldsymbol{\Gamma}_z$ represents the covariance matrix of $\mathbf{Z}$ and $\boldsymbol{\Gamma}_{yz}$ represent the cross-covariance between $\mathbf{Y}$ and $\mathbf{Z}$. When the two factors in equation (2.55) are multiplied, the cross terms vanish identically, resulting in:

$$\begin{aligned}\mathbf{E}_m = &E\left\{\left(\mathbf{y}(i,j) - \boldsymbol{\Gamma}_{yz} \cdot \boldsymbol{\Gamma}_z^{-1} \cdot \mathbf{z}(i,j)\right) \cdot \left(\mathbf{y}(i,j) - \boldsymbol{\Gamma}_{yz} \cdot \boldsymbol{\Gamma}_z^{-1} \cdot \mathbf{z}(i,j)\right)^T\right\} \\ &\left(\boldsymbol{\Gamma}_{yz} \cdot \boldsymbol{\Gamma}_z^{-1} - \mathbf{L}\right) \cdot \boldsymbol{\Gamma}_z \cdot \left(\boldsymbol{\Gamma}_{yz} \cdot \boldsymbol{\Gamma}_z^{-1} - \mathbf{L}\right)^T\end{aligned} \tag{2.56}$$

The MSE associated with the estimator $\mathbf{L}$ is given by the trace of the error matrix. Therefore, equation (2.56) implies:

$$\begin{aligned}tr(\mathbf{E}_m) = &E\left\{\left(\mathbf{y}(i,j) - \boldsymbol{\Gamma}_{yz} \cdot \boldsymbol{\Gamma}_z^{-1} \cdot \mathbf{z}(i,j)\right)^T \cdot \left(\mathbf{y}(i,j) - \boldsymbol{\Gamma}_{yz} \cdot \boldsymbol{\Gamma}_z^{-1} \cdot \mathbf{z}(i,j)\right)\right\} + \\ &tr\left[\left(\boldsymbol{\Gamma}_{yz} \cdot \boldsymbol{\Gamma}_z^{-1} - \mathbf{L}\right) \cdot \boldsymbol{\Gamma}_z \cdot \left(\boldsymbol{\Gamma}_{yz} \cdot \boldsymbol{\Gamma}_z^{-1} - \mathbf{L}\right)^T\right]\end{aligned} \tag{2.57}$$

where $tr(\mathbf{E}_m)$ denotes the trace of matrix $\mathbf{E}_m$. Because both terms are nonnegative, the first, being independent on $\mathbf{L}$, represents a lower limit on the error, which can be achieved by the minimum MSE solution:

$$\mathbf{L}_{CC} = \mathbf{\Gamma}_{yz} \cdot \mathbf{\Gamma}_z^{-1} \tag{2.58}$$

known spectrally as the Chronochrome (CC) transformation and mathematically as a matrix Wiener filter. Notice that in deriving equation (2.58), we assume that the parameters $\mathbf{\Gamma}_z$ and $\mathbf{\Gamma}_{yz}$ are known. In practice, $\mathbf{\Gamma}_z$ and $\mathbf{\Gamma}_{yz}$ are replaced with their ML estimates $\hat{\mathbf{\Gamma}}_z$ and $\hat{\mathbf{\Gamma}}_{yz}$ from the secondary data:

$$\begin{aligned} \hat{\mathbf{\Gamma}}_z &= \frac{1}{N_S \cdot N_L} \sum_{i=1}^{N_S} \sum_{j=1}^{N_L} \mathbf{z}(i,j) \cdot \mathbf{z}(i,j)^T \\ \hat{\mathbf{\Gamma}}_{yz} &= \frac{1}{N_S \cdot N_L} \sum_{i=1}^{N_S} \sum_{j=1}^{N_L} \mathbf{y}(i,j) \cdot \mathbf{z}(i,j)^T \end{aligned} \tag{2.59}$$

Since the minimum mean squared error solution to the corresponding estimation problem (which results in the matrix Wiener filter) depends on cross-correlations between the image pair, the CC method requires pixel-level image co-registration. As a consequence, the CC linear mapping, which statistically connects HS imaging spectra at multiple times, should be applied only when pixel-level co-registration is feasible.

2.5.2 Covariance Equalization (CE) algorithm

Covariance Equalization (CE, [37]) embodies a new, generally applicable multiple regression technique, useful in the absence of point-to-point association knowledge between two multivariate data sets. The utility of the CE technique has been evaluated primarily in transforming signatures acquired under one set of conditions for application to target detection under a second set of conditions (e.g., view angle, slant range, altitude, atmospheric conditions, and time of day). Its effectiveness has been also verified exploring HSI collected in both nadir-viewing and oblique acquisition

conditions [67]. Furthermore, it has also been adopted in CD tasks. CE does not require image registration, thus removing one of the most difficult impediments to the full exploitation of multi-temporal HSI. To derive it, we expand equation (2.54):

$$\mathbf{E}_m = \mathbf{\Gamma}_y - \mathbf{L}\cdot\mathbf{\Gamma}_{yz}^T - \mathbf{\Gamma}_{yz}\cdot\mathbf{L}^T + \mathbf{L}\cdot\mathbf{\Gamma}_z\cdot\mathbf{L}^T \tag{2.60}$$

The only factor requiring co-registration is $\mathbf{\Gamma}_{yz}$, which can be approximated using equation (2.53) [31]. Then, equation (2.61) becomes:

$$\mathbf{E}_m \approx \mathbf{\Gamma}_y - \mathbf{L}\cdot\mathbf{\Gamma}_z\cdot\mathbf{L}^T \tag{2.61}$$

This implies an approximate MSE given by:

$$tr(\mathbf{E}_m) \approx tr(\mathbf{\Gamma}_y) - tr(\mathbf{L}\cdot\mathbf{\Gamma}_z\cdot\mathbf{L}^T) = tr(\mathbf{\Gamma}_y) - tr(\mathbf{\Gamma}_z\cdot\mathbf{L}^T\cdot\mathbf{L}) \tag{2.62}$$

However, because $\mathbf{\Gamma}_y$ is a nonnegative matrix, the last term can be made arbitrarily negative, simply by scaling $\mathbf{L}$ by a large number. Therefore, in [31] it is proposed to adopt a not too greedy strategy requiring that the approximate MSE be zero.

Moreover, since this condition imposes a constraint only on the trace of equation (2.62), a convenient matrix constraint incorporating the trace condition is further obtained by requiring the full approximate covariance matrix $\mathbf{E}_m$ in equation (2.62) to be zero. Thus, we have:

$$\mathbf{L}_{CE}\cdot\mathbf{\Gamma}_z\cdot\mathbf{L}_{CE}^T = \mathbf{\Gamma}_y \tag{2.63}$$

which is the defining equation for the Covariance Equalization family of transformation. Since $\mathbf{\Gamma}_y$ and $\mathbf{\Gamma}_z$ are symmetric matrices, they can be diagonalized by orthonormal transformations:

$$\mathbf{\Gamma}_y = \mathbf{\Delta}_y\cdot\mathbf{D}_y\cdot\mathbf{\Delta}_y^T, \quad \mathbf{\Gamma}_z = \mathbf{\Delta}_z\cdot\mathbf{D}_z\cdot\mathbf{\Delta}_z^T \tag{2.64}$$

where $\mathbf{\Delta}_y, \mathbf{\Delta}_z$ are orthonormal matrices, and $\mathbf{D}_y, \mathbf{D}_z$, are diagonal matrices. Moreover, since $\mathbf{\Gamma}_y$ and $\mathbf{\Gamma}_z$ are nonnegative, so are the entries of $\mathbf{D}_y$ and $\mathbf{D}_z$, which means that symmetric square root matrices can be defined:

$$\mathbf{\Gamma}_y^{1/2} = \mathbf{\Delta}_y \cdot \mathbf{D}_y^{1/2} \cdot \mathbf{\Delta}_y^T, \quad \mathbf{\Gamma}_z^{1/2} = \mathbf{\Delta}_z \cdot \mathbf{D}_z^{1/2} \cdot \mathbf{\Delta}_z^T \tag{2.65}$$

Then equation (2.65) can be manipulated to:

$$\left(\mathbf{\Gamma}_y^{-1/2} \cdot \mathbf{L}_{CE} \cdot \mathbf{\Gamma}_z^{1/2}\right)\left(\mathbf{\Gamma}_y^{-1/2} \cdot \mathbf{L}_{CE} \cdot \mathbf{\Gamma}_z^{1/2}\right)^T = 1 \tag{2.66}$$

so that the general solution can be written as:

$$\mathbf{L}_{CE} = \mathbf{\Gamma}_y^{1/2} \cdot \mathbf{R} \cdot \mathbf{\Gamma}_z^{-1/2} \tag{2.67}$$

with $\mathbf{R}$ some orthonormal matrix. The best choice of $\mathbf{R}$ depends on the application. For HS imagery, it has been found that a valuable choice is the identity matrix, i.e. $\mathbf{R} = \mathbf{I}$, in that $\mathbf{L}_{CC}$ and $\mathbf{L}_{CE}$ produce similar results [31]. Notice that the prediction $\hat{\mathbf{y}}(i,j)$ of $\mathbf{y}(i,j)$ based on equation (2.67):

$$\hat{\mathbf{y}}(i,j) = \mathbf{L}_{CE} \cdot \mathbf{z}(i,j) \tag{2.68}$$

requires $\mathbf{\Gamma}_y$ and $\mathbf{\Gamma}_z$, that are replaced with their ML estimates $\hat{\mathbf{\Gamma}}_y$ and $\hat{\mathbf{\Gamma}}_z$ from the secondary data:

$$\begin{aligned} \hat{\mathbf{\Gamma}}_y &= \frac{1}{N_S \cdot N_L} \sum_{i=1}^{N_S} \sum_{j=1}^{N_L} \mathbf{y}(i,j) \cdot \mathbf{y}(i,j)^T \\ \hat{\mathbf{\Gamma}}_z &= \frac{1}{N_S \cdot N_L} \sum_{i=1}^{N_S} \sum_{j=1}^{N_L} \mathbf{z}(i,j) \cdot \mathbf{z}(i,j)^T \end{aligned} \tag{2.69}$$

In summary, because CE releases the requirement of pixel-level image co-registration, it represents a valuable method to effectively approach radiometric compensation when accurate image co-registration is not feasible.

Chapter 3

Residual mis-registration noise estimation

In this chapter we describe a novel method to estimate the first and second order statistics of the Residual Mis-Registration noise (RMR), which severely affects the performance of ACD techniques. Depending on the specific distribution of the RMR, the estimates allow to precisely define the size of the uncertainty window, which is crucial when dealing with mis-registration noise, as in the LCRA approach. The technique is based on a sequential strategy that exploits the well known Scale Invariant Feature Transform (SIFT) algorithm cascaded with the Minimum Covariance Determinant (MCD) algorithm. The proposed method adapts the SIFT procedure, which was originally developed to work on gray level images, to HSI so as to exploit the complementary information content of the numerous spectral channels, further improving the robustness of the outliers filtering by means of a highly robust estimator of multivariate location. The approach has been tested on different real HSI with very high spatial resolution. The analysis highlighted the effectiveness of the proposed strategy, providing reliable and very accurate estimation of the RMR statistics.

3.1 Introduction

Most of the ACD techniques proposed in the literature require the images to be perfectly aligned. Therefore, images are typically geo-referenced and ortho-rectified by means of GPS-INS data combined with the use of rational polynomial coefficients (RPCs) and a digital elevation model (DEM) [76], [77]. Due to the unavoidable onboard instrumentation errors and to the DEM inaccuracy, this process does not guarantee the perfect alignment between images, and further processing (co-registration) is necessary to improve the alignment accuracy. Co-registration typically consists in applying a spatial transformation to the test image, based on a parametric model of the geometrical distortion between the two images, so that pixels occupying the same position in the two images correspond to the same ground resolution cell in the monitored scene. Co-registration accuracy can be further enhanced with unsupervised techniques that estimate and correct the local mis-registration errors. Several methods have been proposed in the literature to reduce the effects of mis-registration errors, based on the optimization of a specific similarity measure between local patches of the image pair [78], the gradient of the registered image combined with a Thin Plate Spline (TPS) transform [48] and the normalized cross-correlation for characteristic channels of the image dataset [49]. However, even after the application of the above mentioned techniques, a residual mis-registration error (RMR, hereinafter) inevitably remains. Such a residual error can be viewed as a per pixel shift in both the row and column directions, whose magnitude is typically in the order of few pixels or of a fraction of pixel in the best case. It has been shown [50] that the RMR is detrimental for pixel-based ACD algorithms, because it leads to a detection performance loss increasing with its magnitude.

Recently, the LCRA ([45], [51]) approach has been proposed to cope with the performance degradation problem due to the RMR, providing excellent results in ACD tasks. The LCRA approach embeds the a priori knowledge on the magnitude of the RMR on the pixel based change detection scheme. In order to reduce the effects due to

RMR, in the LCRA approach one compares the Pixel Under Test (PUT) in the position (i, j) of the test image with those belonging to a given neighbourhood of the coordinates (i, j) in the reference image. Such a neighbourhood is selected by means of an uncertainty window (UW) whose size has to be chosen in accordance with the magnitude of the RMR ([52]). This choice is crucial in that it strongly influences both the detection performance and the computational load of LCRA based ACD algorithms. In fact, on one hand the UW should be large enough to allow the RMR effects to be properly compensated. On the other hand, it should be as small as possible, because it determines the spatial resolving capability of the ACD algorithm. In fact, there are cases where it is of operational interest to detect also small displacements, and increasing the size of the UW can be detrimental for ACD performance. For instance, vehicles and/or people monitoring in tactical scenarios is achieved by means of rapid and subsequent flights in the area of interest. In order to avoid mis-detection of slow moving targets, the UW should be as small as possible. As a second example, change detection of a target surrounded by objects having spectral signature similar to the target of interest, such as the case of deletion of a car among a group of similar vehicles in a parking lot, requires the UW to be as small as possible. Moreover, it is important to remark that the computational cost of LCRA based ACD increases with the UW size.

The magnitude of the RMR is not *a priori* known. Though it could be estimated on the basis of a) the GPS positional errors, b) the INS angular errors and c) the DEM errors [52], these ancillary data are not always available. Therefore, in most of the cases, the estimation of the RMR noise remains an open issue, and the UW in the LCRA approach is generally set in an almost arbitrary fashion by making some assumptions about the magnitude of the RMR. To the best of our knowledge there is not a criterion to fix the UW size without any knowledge about the RMR properties.

In this chapter we propose a new fully unsupervised algorithm to estimate the magnitude of the RMR directly from the image pairs. The proposed technique assumes the RMR as a unimodal bivariate random variable and estimates both its mean value and its covariance matrix. Such estimates allow the UW in LCRA approach to be precisely defined. The proposed technique is based on the well known Scale Invariant

Feature Transform (SIFT, [57], [58]) algorithm, which represents a valuable tool for extracting interest points (Keypoints, KPs) in gray level images on the basis of their local spatial features. The SIFT algorithm is embedded in a sequential processing scheme that allows the potential distinct spectral features present in different bands of the hyperspectral data to be accounted for. The algorithm is robust to radiometric differences between the two processed HSIs and it does not require ancillary data about the instrumentation accuracy or weather conditions during the acquisitions. Therefore, when dealing with ACD problem, it can be successfully applied as a method to mitigate the effect of misalignment both after the co-registration step and in those applications that use the image pairs aligned through direct geo-referencing. This particular feature of the proposed method is of great interest for those situations (such as area surveillance) where a prompt response has to be given in near real time and the co-registration task is not feasible because it is typically very time consuming [18].

The rest of the chapter is organized as follows. In section 3.2, the RMR model is described, and the two-parameter noise model is introduced. In section 3.3, the algorithm for RMR noise parameters estimation is presented. In section 3.4 and 3.5, results obtained on different real HSIs are discussed and conclusions are drawn.

3.2 Residual mis-registration noise model

Let us consider two HSIs $\mathbf{Y}$ (test image) and $\mathbf{Z}$ (reference image) collected over the same geographical area at two different times. Let us assume that the hyperspectral sensor has L spectral channels and denote with ζ the geographical coordinates of the generic ground resolution cell (GRC) in the scene (i.e. ζ is a two-value array in metric or angular coordinates derived by assuming a distinctive map projection).

Furthermore, let us denote as $\mathbf{y}[\boldsymbol{\eta}_Y(\zeta)]$ the $Lx1$ spectral pixel of $\mathbf{Y}$ corresponding to the GRC positioned in ζ and as $\boldsymbol{\eta}_Y(\zeta)=[r_Y, c_Y]^{\mathrm{T}}$ the vector of the row and column coordinates of that cell in the $\mathbf{Y}$ image. Similarly, $\mathbf{z}[\boldsymbol{\eta}_Z(\zeta)]$ is the $Lx1$ spectral pixel of Z

and $\boldsymbol{\eta}_Z(\zeta)=[r_Z,c_Z]^{\mathrm{T}}$ is the vector of the row and column coordinates in the $\mathbf{Z}$ image of the GRC in ζ. The RMR between the test and the reference image is defined as:

$$\boldsymbol{\Delta}(\zeta)=\boldsymbol{\eta}_Z(\zeta)-\boldsymbol{\eta}_Y(\zeta) \tag{3.1}$$

It is worth noting that the RMR in (3.1) is the residual misalignment of the coordinates (in the row and column directions) denoting the position in the two images of a pixel corresponding to the same GRC.

It must not be confused with the registration noise (RN) introduced and analyzed in [46] and [47] that indicates the effects of the residual mis-registration on the values of the spectral change vectors.

In (3.1) $\boldsymbol{\Delta}(\zeta)$ is modelled as a 2-dimensional wide-sense stationary random process, i.e. $\boldsymbol{\Delta}(\zeta)=[\Delta_r(\zeta),\Delta_c(\zeta)]$ with mean vector $\boldsymbol{\mu}_\Delta=E\{\boldsymbol{\Delta}(\zeta)\}$ and covariance matrix $\boldsymbol{\Gamma}_\Delta=E\left\{[\boldsymbol{\Delta}(\zeta)-\boldsymbol{\mu}_\Delta]\cdot[\boldsymbol{\Delta}(\zeta)-\boldsymbol{\mu}_\Delta]^T\right\}$. Returning, for a moment, to the UW setting problem in the LCRA approach, both $\boldsymbol{\mu}_\Delta$ and $\boldsymbol{\Gamma}_\Delta$ provide useful information to account for the RMR effects. In fact, $\boldsymbol{\mu}_\Delta$ provides an indication of the position of the UW in the reference image, and $\boldsymbol{\Gamma}_\Delta$ allows the size of the UW in both the spatial dimensions to be properly set. In practice, $\boldsymbol{\mu}_\Delta$ and $\boldsymbol{\Gamma}_\Delta$ are not generally *a priori* known. In the following we propose a method to estimate both the parameters directly from the two images $\mathbf{Y}$ and $\mathbf{Z}$.

Specifically, starting from the KPs extracted from the test and the reference image, a set of KP pairs obtained by selecting the KPs with similar features from the two images is determined. Such KP pairs are adopted for estimating both $\boldsymbol{\mu}_\Delta$ and $\boldsymbol{\Gamma}_\Delta$. The *i-th* KP pair is associated with the coordinate vector $\mathbf{k}(\zeta_i)=(\boldsymbol{\eta}_X(\zeta_i),\boldsymbol{\eta}_Y(\zeta_i))$ of two pixels from the images $\mathbf{Y}$ and $\mathbf{Z}$, respectively, corresponding to the GRC located at ζ_i. In the following, for the sake of clarity, we skip the dependence on ζ_i in $\mathbf{k}(\zeta_i)$ and use the term KP pair to indicate the coordinate vector $\mathbf{k}_i=\left(\boldsymbol{\eta}_Y^{(i)},\boldsymbol{\eta}_Z^{(i)}\right)$. The KP pairs and the estimates $\hat{\boldsymbol{\mu}}_\Delta$ and $\hat{\boldsymbol{\Gamma}}_\Delta$ are obtained through a sequential strategy that makes use of a well known procedure based on the SIFT algorithm.

SIFT is a method for extracting distinctive invariant features from images that can be used to perform reliable matching between multi-temporal images. The features are invariant to image scale and rotation, and are shown to provide robust matching across affine distortion, addition of noise, and illumination changes ([58]).

3.3 Noise parameters estimation algorithm

In order to describe the proposed sequential strategy, we start by focusing on a specific iteration denoted with the index *l*. At the *l*-th step, two main operations are performed:

1. detection of KP pairs: the SIFT procedure is applied to the images corresponding to the *l-th* band of the reference and the test HSIs, respectively, in order to extract the KPs, and the matched KP pairs are retained.

2. Robust estimation of the RMR parameters: a robust mean and covariance matrix estimation algorithm is applied to obtain the partial estimates $\hat{\boldsymbol{\mu}}_{\Delta}^{(l)}$ and $\hat{\boldsymbol{\Gamma}}_{\Delta}^{(l)}$ from the KP pairs.

Since the SIFT algorithm is well documented in the specialized literature ([58]), in the following we only summarize its main features.

SIFT has four main modules: 1) scale-space extrema detection, 2) KPs localization, 3) orientation assignment and 4) KPs description. The first three modules aim at extracting the KPs from each of the analyzed image, whereas the fourth assigns to each extracted KP a 128-dimensional vector of descriptors that distinctively identifies the neighbourhood around the position where such a KP is located. In the proposed procedure, to further improve the robustness of the SIFT descriptors to illuminations changes, we apply the algorithm to the two images $\widetilde{Y}_l$ and $\widetilde{Z}_l$, obtained by properly normalizing the images Y_l and Z_l corresponding to the *l*-th band of the test and the reference HSIs:

$$\widetilde{Y}_l = \frac{Y_l - y_l^{\max}}{y_l^{\max} - y_l^{\min}} \cdot 2^R; \;\; \widetilde{Z}_l = \frac{Z_l - z_l^{\max}}{z_l^{\max} - z_l^{\min}} \cdot 2^R \tag{3.2}$$

where $y_l^{\max}$, $y_l^{\min}$, $z_l^{\max}$ and $z_l^{\min}$ are the maximum and the minimum levels in the two images Y_l and Z_l, respectively, whereas R is the radiometric resolution of the considered data.

Once the KPs have been extracted from each of the two images the KP pairs are detected by means of their descriptor vectors and by resorting to a matching criterion based on the minimum Euclidean distance. In particular, let us denote with $K_Y^{(l)}$ and $K_Z^{(l)}$ (generally $K_Y^{(l)} \neq K_Z^{(l)}$) the number of KPs extracted from the test and the reference image, respectively, and with $\boldsymbol{\chi}_Y^k$ ($k = \{1,...,K_Y\}$) and $\boldsymbol{\chi}_Z^m$ ($m = \{1,...,K_Z\}$) the descriptors of the *k-th* KP in the test image and the *m-th* KP in the reference image. The KPs matching is accomplished by means of the following decision rule: the *k-th* KP in the test image is assigned to the *j-th* KP in the reference image, if $\boldsymbol{\chi}_Y^j$ is the closest to $\boldsymbol{\chi}_Z^k$ (in the Euclidean distance sense) and the ratio between $D\left(\boldsymbol{\chi}_Y^k, \boldsymbol{\chi}_Z^j\right)$ and $D\left(\boldsymbol{\chi}_Y^k, \boldsymbol{\chi}_Z^n\right)$ is below a given threshold:

$$\frac{D\left(\boldsymbol{\chi}_T^k, \boldsymbol{\chi}_R^j\right)}{D\left(\boldsymbol{\chi}_T^k, \boldsymbol{\chi}_R^n\right)} < \eta \tag{3.3}$$

In (3.3) $D\left(\boldsymbol{\chi}_T^k, \boldsymbol{\chi}_R^j\right)$ denotes the Euclidean distance between the descriptors of two given KPs and $\boldsymbol{\chi}_Z^n$ is the second-closest to $\boldsymbol{\chi}_Y^k$. In [58] the authors proposed typical values for η ranging from 0.7 to 0.8. The matching algorithm is applied to each KP of the test image and at the end of the procedure, $R^{(l)}$ KP pairs $\mathbf{k}_r^{(l)}$ ($r = \left\{1,...,R^{(l)}\right\}$) with $R^{(l)} \leq \min\left(K_Y^{(l)}, K_Z^{(l)}\right)$, are extracted.

The $R^{(l)}$ KP pairs $\mathbf{k}_r^{(l)}$ extracted at the *l*-th step (from $\widetilde{Y}_l$ and $\widetilde{Z}_l$) are adopted to update the set of all the KP pairs extracted up to the $l-1$*-th* step. In particular, the set of all the KP pairs extracted in the previous steps $U^{(l-1)}$, is updated by adding the KP pairs $\mathbf{k}_r^{(l)}$ which are not already included in $U^{(l-1)}$, i.e. the duplicated pairs are rejected in order to retain only $\widetilde{T}^{(l)}$ ($\widetilde{T}^{(l)} \geq R^{(l)}$) distinct pairs. In this way, a new set $\widetilde{U}^{(l)}$ of $\widetilde{T}^{(l)}$ KP pairs is

defined. From the KP pairs in $\widetilde{U}^{(l)}$, according to equation (3.1), we derive the realizations $\boldsymbol{\Delta}_n$ ($n=1,...,\widetilde{T}^{(l)}$) of the RMR which are, in turn, adopted to obtain the partial estimates of the RMR model parameters $\hat{\boldsymbol{\mu}}_{\Delta}^{(l)}$ and $\hat{\boldsymbol{\Gamma}}_{\Delta}^{(l)}$. In such estimation process, in order to filter the potential outliers in the observed RMR realizations [68], we make use of the Minimum Covariance Determinant (MCD, [69]) method that is a highly robust estimator of multivariate location and scatter. Its objective is to find the *H* observations (out of $\widetilde{T}^{(l)}$) called *inliers*, whose covariance matrix ($\hat{\boldsymbol{\Gamma}}_{\Delta}^{(l)}$) has the lowest determinant. The MCD estimate of location $\hat{\boldsymbol{\mu}}_{\Delta}^{(l)}$ is then the average of these *H* points. Since the number *H* of inliers should be specified as an input parameter, we set *H* by exploiting the estimates $\hat{\boldsymbol{\mu}}_{\Delta}^{(l-1)}$ and $\hat{\boldsymbol{\Gamma}}_{\Delta}^{(l-1)}$ attained at the previous iteration of the proposed procedure and the multidimensional Chebyshev's inequality ([70]). Particularly, *H* is determined as the number of the observed $\boldsymbol{\Delta}_n$ included in a confidence ellipsoid at a given level α ($\alpha << 1$, typical values are $\alpha = 0.05, 0.1$) that is obtained by considering the two dimensional Chebyshev's inequality:

$$\begin{aligned} &\Pr\left(d^{MAHA}(\boldsymbol{\Delta}) < \lambda\right) \le 1-\alpha \\ &d^{MAHA}(\boldsymbol{\Delta}) = \sqrt{\left[\boldsymbol{\Delta}-\boldsymbol{\mu}_{\Delta}\right]^{T} \cdot \boldsymbol{\Gamma}^{-1} \cdot \left[\boldsymbol{\Delta}-\boldsymbol{\mu}_{\Delta}\right]} \\ &\lambda = \sqrt{2/\alpha} \end{aligned} \tag{3.4}$$

In (3.4) $d^{MAHA}(\boldsymbol{\Delta})$ is the Mahalanobis distance of the random variable $\boldsymbol{\Delta}$. Since $\boldsymbol{\mu}_{\Delta}$ and $\boldsymbol{\Gamma}_{\Delta}$ are not known we determine the confidence ellipsoid at level α by considering the Mahalanobis distance evaluated with respect to the estimates $\hat{\boldsymbol{\mu}}_{\Delta}^{(l-1)}$ and $\hat{\boldsymbol{\Gamma}}_{\Delta}^{(l-1)}$.

Once the new estimates $\hat{\boldsymbol{\mu}}_{\Delta}^{(l)}$ and $\hat{\boldsymbol{\Gamma}}_{\Delta}^{(l)}$ have been obtained by applying the MCD algorithm, the set of the KP pairs $U^{(l)}$ (with cardinality $T^{(l)} \le \widetilde{T}^{(l)}$) is derived by retaining only the *inliers* pairs in $\widetilde{U}^{(l)}$. For this purpose, the same idea behind the choice of H is exploited. Specifically, the confidence ellipsoid at level α is determined by means of the two dimensional Chebyshev's inequality (equation (3.4)) applied to the Mahalanobis distance evaluated with respect to $\hat{\boldsymbol{\mu}}_{\Delta}^{(l)}$ and $\hat{\boldsymbol{\Gamma}}_{\Delta}^{(l)}$, and all the KP pairs in $\widetilde{U}^{(l)}$ which are not included in such an ellipsoid are discarded.

Focusing on the *l*-th step, the proposed procedure can be summarized as follows:

- *Normalization*: the images $\widetilde{Y}_l$ and $\widetilde{Z}_l$ are derived by applying the normalization in equation (3.2) to Y_l and Z_l, corresponding to the *l-th* band of the test and the reference HSIs.

- *KP pairs extraction:* $R^{(l)}$ KP pairs ($\mathbf{k}_r^{(l)}$) are extracted from the two images by combining the SIFT procedure for the selection of the KPs in each image and the Euclidean distance based decision rule in (3.3) to match the homologous KPs in the two images.

- *Update of the set of KP pairs* $U^{(l-1)}$: the set $\widetilde{U}^{(l)}$ (with cardinality $\widetilde{T}^{(l)}$) is constructed by adding the new KP pairs ($\mathbf{k}_r^{(l)}$) to those derived in the previous steps (and included in $U^{(l-1)}$).

- *RMR model parameters robust estimation:* the estimates $\hat{\boldsymbol{\mu}}_{\Delta}^{(l)}$ and $\hat{\boldsymbol{\Gamma}}_{\Delta}^{(l)}$ are obtained from the KP pairs in $\widetilde{U}^{(l)}$ by applying the robust MCD estimation algorithm.

- *KP pairs filtering*: the set $U^{(l)}$ (with cardinality $T^{(l)} \le \widetilde{T}^{(l)}$) is extracted from $\widetilde{U}^{(l)}$ by discarding the KP pairs which are not in accordance with the RMR model, i.e.: those KP pairs which fall outside the confidence ellipsoid at level α determined on the basis of the estimates $\hat{\boldsymbol{\mu}}_{\Delta}^{(l)}$ and $\hat{\boldsymbol{\Gamma}}_{\Delta}^{(l)}$ and the two dimensional Chebyshev's inequality.

The previously described procedure is iterated until all the L spectral channels are explored or alternatively until the number $T^{(l)}$ of the extracted inliers gets a user-defined value *N*. Notice that at the first step of the algorithm, the estimates $\hat{\boldsymbol{\mu}}_{\Delta}^{(1)}$ and $\hat{\boldsymbol{\Gamma}}_{\Delta}^{(1)}$ are not obtained by the MCD algorithm, in that at the first step we do not have information about the number *H* of inliers. At that step, in order to mitigate the effects of potential outliers, the estimation of the mean values and standard deviations of the two RMR components, are obtained by exploiting the median, i.e. $\hat{\boldsymbol{\mu}}_{\Delta_r}^{(1)} \equiv \text{median}(\Delta_r(\zeta))$, $\hat{\boldsymbol{\mu}}_{\Delta_c}^{(1)} \equiv \text{median}(\Delta_c(\zeta))$, and the Median Absolute Deviation (MAD), i.e.

$\hat{\boldsymbol{\sigma}}_{\Delta_r}^{(1)} \equiv 1.4826 \cdot \text{median}\left|\Delta_r(\boldsymbol{\zeta}) - \text{median}(\Delta_r(\boldsymbol{\zeta}))\right|$ and $\hat{\boldsymbol{\sigma}}_{\Delta_c}^{(1)} \equiv 1.4826 \cdot \text{median}\left|\Delta_c(\boldsymbol{\zeta}) - \text{median}(\Delta_c(\boldsymbol{\zeta}))\right|$, whereas the correlation coefficient is assumed to be zero.

The whole procedure which will be referred to as Sequential RMR Estimation algorithm (SRMRE), provides as final result the estimates $\hat{\boldsymbol{\mu}}_{\Delta} = \left[\hat{\mu}_{\Delta_R}, \hat{\mu}_{\Delta_C}\right]$ and $\hat{\boldsymbol{\Gamma}}_{\Delta} = \begin{bmatrix} \hat{\sigma}_{\Delta_R}^2 & \hat{\rho}_{\Delta}\hat{\sigma}_{\Delta_R}\hat{\sigma}_{\Delta_C} \\ \hat{\rho}_{\Delta}\hat{\sigma}_{\Delta_R}\hat{\sigma}_{\Delta_C} & \hat{\sigma}_{\Delta_C}^2 \end{bmatrix}$.

In the previous formulas we denoted as $\hat{\mu}_{\Delta_R}$ and $\hat{\sigma}_{\Delta_R}$ the estimates of the mean value and the standard deviation of the RMR in the row direction, with $\hat{\mu}_{\Delta_C}$ and $\hat{\sigma}_{\Delta_C}$ the estimates of the mean value and the standard deviation of the RMR in the column direction and with $\hat{\rho}_{\Delta}$ the estimate of the correlation coefficient between the two components of the RMR vector $\boldsymbol{\Delta}$.

3.4 Experimental results

To evaluate the performance of the proposed method, an experimental analysis has been conducted on two different hyperspectral datasets with high spatial resolution. The first image pair was collected in a rural area over Virginia City with a push-broom hyperspectral sensor. The main characteristics of the data are listed in Table 3.1.

SPECTIR HSI	
Sensor Type	Pushbroom
Platform	Aerial
Spectral range	400-2500 nm
Spectral resolution	5 nm
Spectral channels	356
Ground Spatial Distance	1 m
Number of rows	169
Number of columns	300

Table 3.1 SPEC-TIR Sensor. Main Characteristics of the Virginia Dataset.

The sensor incorporated three ring laser gyro based INS, coupled with a 12-channel GPS system. This case study represents an example of RMR noise estimation in applications based on the direct geo-referencing approach. The geographical coordinates ζ for each pixel are estimated by the onboard inertial instrumentation and stored in an input geometry (IGM) file which is then used for the subsequent processing. Thus, in this direct geo-referencing approach the error introduced by the GPS and INS instrumentation accuracy in the estimate of ζ determines the RMR $\Delta(\zeta)$ through equation (3.1).

We assumed as a benchmark the RMR statistics obtained by means of a supervised technique aimed at selecting couples of corresponding pixels (Control Points, CPs) in the Red Green Blue (RGB) representation of the HSI. In particular, the selection was accomplished by visually inspecting the two images in order to find well noticeable CPs, such as corners, blobs, prominent edges. The extracted CPs were successively adjusted by exploiting the normalized cross-correlation (NCC) to get a sub-pixel accuracy from the coarse CPs selection. In particular, for each CP pair, a template and a region were extracted around the test and the reference CP, respectively. Then the NCC of the template with the region, interpolated in order to achieve an accuracy of one-tenth of a pixel, was calculated, and the absolute peak of the cross-correlation matrix was found. Finally, the position of the peak was used to adjust the coordinates of the test CP

[71]. In Figure 3.1 a) and b) we show the RGB representation of the two considered HSIs where the extracted CPs have been superimposed.

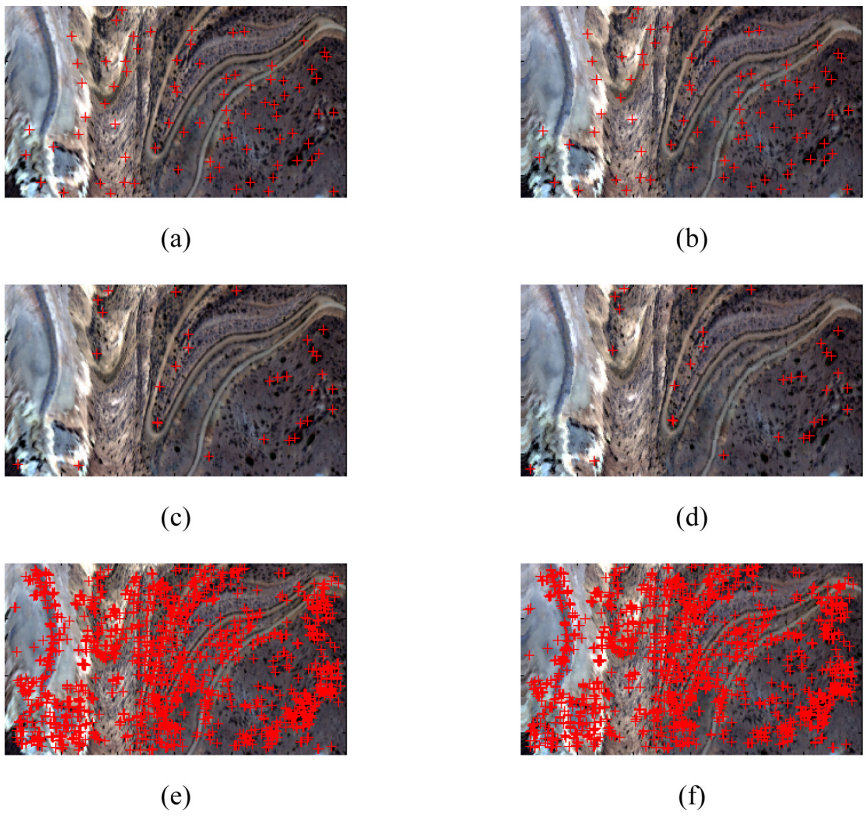

Figure 3.1. RGB representation of the Virginia Dataset: extracted KPs are superimposed in red. (a) Test Image with Supervised CPS, (b) Reference Image with Supervised CPS, (c) Test Image with KPS pairs extracted on GLI, (d) Reference Image with KPS pairs extracted on GLI, (e) Test Image with KPS pairs extracted by means of the SRMRE algorithm, (f) Reference Image with KPS pairs extracted by means of the SRMRE algorithm.

In order to show the improvement derived by exploiting all the spectral content of the data, we compare the results obtained by applying the proposed procedure to: a) the entire hyperspectral dataset and b) in a one-step manner where a single band image is analyzed. In the following, we report the results obtained by considering the images derived by resorting to the conversion from the RGB representation to the gray level image (GLI, hereinafter). Similar results have been found by analyzing as single band images those obtained by taking the 1^{st} principal component of each hyperspectral image and those corresponding to the bands with the highest variance. In Figure 3.1 c) and d) we show the KP pairs extracted by combining the SIFT algorithm and the matching rule described in the previous section (with $\eta = 0.8$). Whereas in Figure 3.1 e)

and f) we show the KP pairs obtained by the proposed SRMRE that explores all the spectral bands (also in this case we set $\eta = 0.8$ at each iteration and $\alpha = 0.1$).

As it can be noticed, the number of KP pairs extracted from the GLI is very low (31) if compared with that provided by the SRMRE (1378), and the KPs are concentrated in three main regions of the image. On the contrary, KP pairs extracted by the proposed procedure are distributed over all the image, thus resulting in a potentially more consistent estimate of the RMR noise parameters.

Moreover, the increase of the cardinality of the KPs pairs selected by the SRMRE is spread along all the spectral channels, as depicted in Figure 3.2, indeed confirming the benefits arising from the exploitation of the entire dataset.

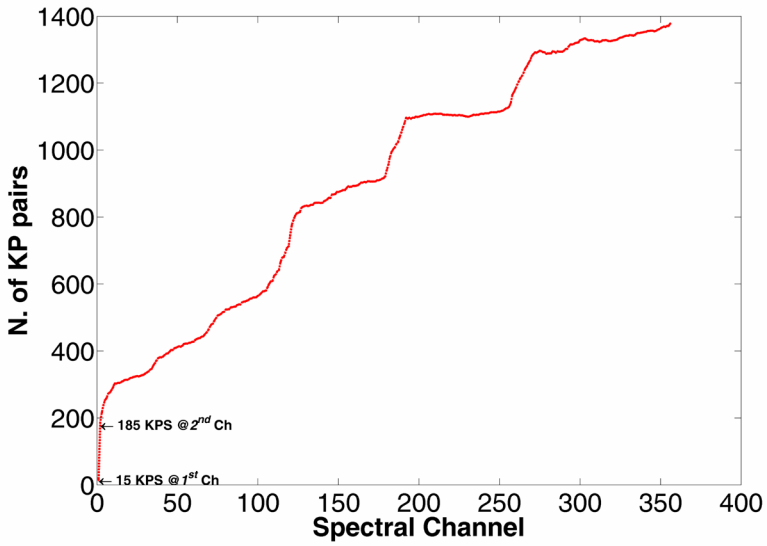

Figure 3.2. Virginia City Dataset: selected KPs pair cardinality vs Spectral Channels.

In Figure 3.3 the scatterplots of the RMR noise realizations, along the row and the column directions, are shown. Particularly, in Figure 3.3 a) the RMR noise realizations obtained by the supervised CPs selection procedure (assumed as benchmark in this experiment) are showed, whereas in Figure 3.3 b) and c) the RMR noise realizations obtained on the GLI and those provided by the SRMRE are reported. In the figures we also plot the confidence ellipsoid at level $\alpha = 0.1$ derived by using the estimates of $\boldsymbol{\mu}_{\Delta}$ and $\boldsymbol{\Gamma}_{\Delta}$ obtained in the three cases. Notice that the graphs show that the noise

realizations obtained by both the one-step procedure and the SRMRE are in accordance with those extracted by the supervised CPs selection method. This confirms the goodness of both the procedures in selecting the RMR noise realizations.

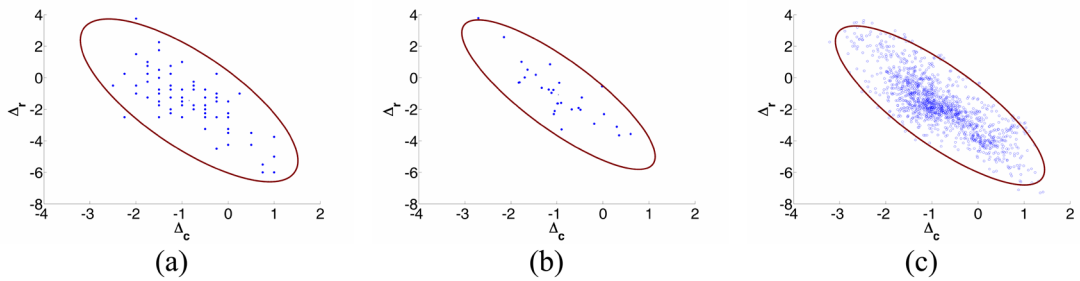

Figure 3.3. Virginia City Dataset: scatterplot of the RMR noise realizations along row (y axis, Δ_r) and column (x axis, Δ_c) direction. (a) Supervised, (b) one-step on the GLI, (c) SRMRE.

In Table 3.2 we report the estimates of the RMR noise parameters obtained on the GLI and by the SRMRE. In the same table we also show the noise parameters estimated by the RMR noise realizations provided by the supervised procedure that are assumed as benchmark values. In particular, we denote as $\mu_{\Delta r}$, $\mu_{\Delta c}$, $\sigma_{\Delta r}$, $\sigma_{\Delta c}$ the mean values and the standard deviations along the row and the column directions, and with ρ_{Δ} the correlation coefficient assumed as benchmark values. Instead we denote as $\hat{\mu}_{\Delta r}$ and $\hat{\sigma}_{\Delta r}$ the estimates of the mean value and of the standard deviation of the RMR in the row direction, with $\hat{\mu}_{\Delta_C}$ and $\hat{\sigma}_{\Delta_C}$ the estimates of the mean value and of the standard deviation of the RMR in the column direction and with $\hat{\rho}_{\Delta}$ the estimate of the correlation coefficient between the two components of the RMR.

Benchmark Values		Estimated Values			RSE		
	Supervised		**One-step on GLI**	**SRMRE**		**One-step on GLI**	**SRMRE**
N.Pts	80 CPS		31 KPs	1378 KPs			
$\mu_{\Delta r}$	-1.44	$\hat{\mu}_{\Delta r}$	-1.07	-1.76	$RSE_{\mu_{\Delta r}}$	0.37	0.32
$\mu_{\Delta c}$	-0.85	$\hat{\mu}_{\Delta c}$	-0.97	-0.83	$RSE_{\mu_{\Delta c}}$	0.12	0.02
$\sigma_{\Delta r}$	1.82	$\hat{\sigma}_{\Delta r}$	1.67	1.78	$RSE_{\sigma_{\Delta r}}$	0.15	0.04
$\sigma_{\Delta c}$	0.84	$\hat{\sigma}_{\Delta c}$	0.74	0.80	$RSE_{\sigma_{\Delta c}}$	0.1	0.04
ρ_{Δ}	-0.74	$\hat{\rho}_{\Delta}$	-0.83	-0.80	$RSE_{\rho_{\Delta}}$	0.09	0.06

Table 3.2. RMR noise parameters estimation. Virginia City dataset.

The comparison of the benchmark values with the results obtained by the SRMRE and the one-step procedure on the GLI, shows that both the algorithms provide values that completely agree with the benchmark ones. Nevertheless, the SRMRE derives the estimates from a number of observations higher than that used in the GLI and this suggests that the SRMRE yields potentially more accurate and reliable estimates of the parameters.

It is important to note that a rigorous performance analysis on the RMR noise parameters estimation algorithms should be carried out by comparing the estimated values with the actual ones. Unfortunately, such an analysis is not feasible when dealing with real data, because the exact values of the parameters from the analyzed images are not available. The values assumed as benchmark, thought obtained by a reliable procedure combining human intervention with a specific refinement algorithm, are not the actual values of the parameters but estimates of them. So, they are, in turn, affected by errors induced by the estimation algorithm (depending on the number of selected CPs) and those due to the unavoidable inaccuracy of the CPs selection procedure. However, they give a sufficiently reliable estimate of the actual parameters values and are useful to describe the general trend of the RMR noise. Just to give a numerical example we have computed the Root Square Error (RSE) between the benchmark

values and the estimates of the noise parameters obtained by the two algorithms. By analyzing the RSE values we note that the SRMRE procedure provides the best result (the smallest RSE for each parameter). For instance the RSE in the estimation of $\sigma_{\Delta c}$ and $\sigma_{\Delta r}$ with the SRMRE is almost 4 times lower than that obtained on the GLI (i.e. $RSE_{\sigma_{\Delta r}} = 0.04$ and 0.15 in the case of SRMRE and one-step algorithm over GLI, respectively). The difference between the RSE obtained by the two algorithms is more pronounced in the case of the mean value $\mu_{\Delta c}$, where the SRMRE is six time better than the corresponding RSE on GLI ($RSE_{\mu_{\Delta c}} = 0.02$ and 0.12 for SRMRE and one-step algorithm over GLI, respectively).

As a second example, we employed the data sets included in the RIT Target Detection project, which are publicly available [72], and consist of two co-registered radiance images (the self and the blind test images) collected with the Hymap sensor around the village of Cooke City, Montana, USA. The two images adopted in this second example were co-registered using supervised selected ground control points. Thus, in this case study the RMR noise is not dominated by the instrumentation errors but it is basically determined by the inaccuracy of the co-registration algorithm. The images include urban and rural environments, and they have been acquired with different illumination conditions. In Table 3 we report the main characteristics of the data. Further details can be found in [73].

HY-MAP HSI	
Sensor Type	Pushbroom
Platform	Aerial
Spectral range	400-2500 nm
Spectral resolution	15 nm
Spectral channels	126
Ground Spatial Distance	3 m
Number of rows	800
Number of columns	280

Table 3.3. HY-MAP Sensor. Main Characteristics of the Cooke City Dataset.

The experimental analysis has been carried out following the same procedure described in the previous example. The extracted CPs and KPs, along with the RGB representation of the collected images are showed in Figure 3.4.

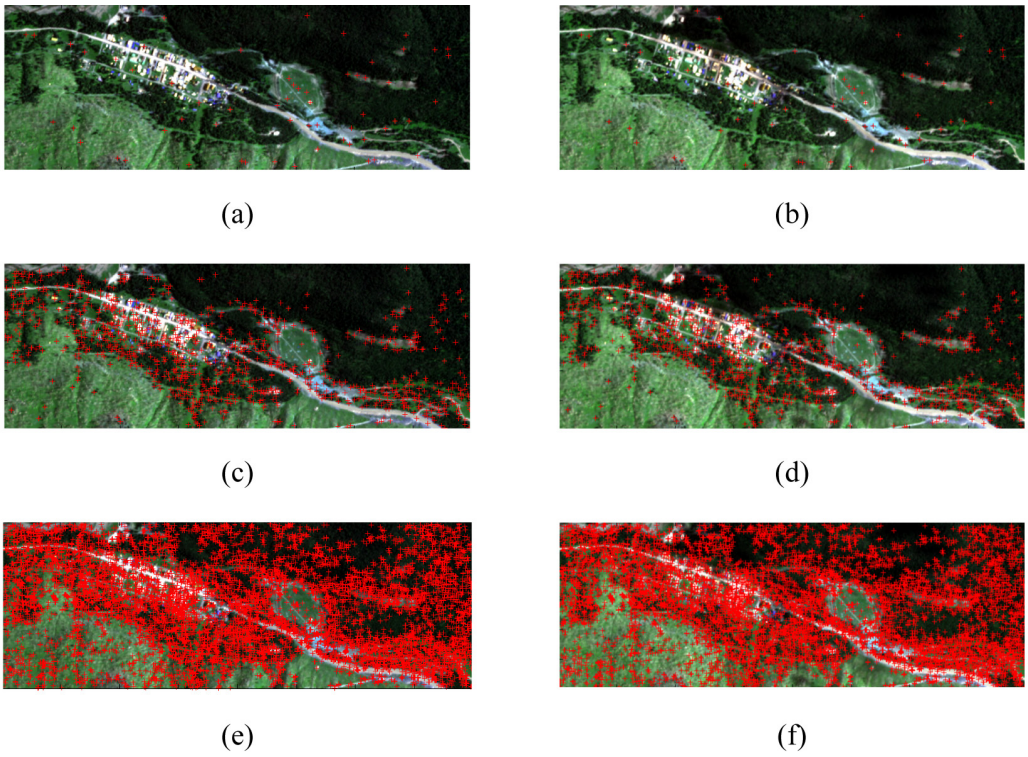

Figure 3.4. RGB representation of the Cooke City Dataset: extracted KPs are superimposed in red. (a) Test Image with Supervised CPS, (b) Reference Image with Supervised CPS, (c) Test Image with KPS pairs extracted on GLI, (d) Reference Image with KPS pairs extracted on GLI, (e) Test Image with KPS pairs extracted by means of the SRMRE algorithm, (f) Reference Image with KPS pairs extracted by means of the SRMRE algorithm.

Due to the higher spatial details contained in the scene, the exploitation of the GLI leads to better results in terms of number of selected KPs pairs, with respect to the previous case. However, the trend observed in the previous example about the spatial distribution of the KP pairs seems to be confirmed. In fact, when the procedure is applied to the GLI, the resulting selected KP pairs are located around well defined regions, such as the urban area. Moreover, regions which are affected by changes in illumination and shadow, such as the vegetation area in the middle right of the scene, are scarcely represented. This is probably due to the fact that the spectral information content is not completely exploited. Such a conclusion is supported by the fact that the SRMRE algorithm that integrates the information taken from all the spectral bands of the HSIs,

provides KP pairs located all over the observed scene. It is worth noting that, also in this case, the cardinality of the selected KPs pairs visibly increases along the spectral channels, as depicted in Figure 3.5.

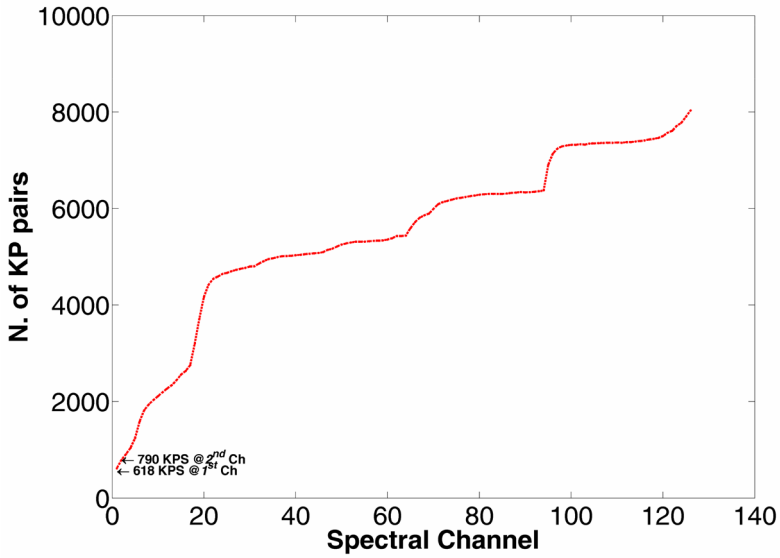

Figure 3.5. Cooke City Dataset: selected KPs pair cardinality vs Spectral Channels.

In Figure 3.6 the scatterplots of the RMR noise realizations obtained by a) the supervised procedure, b) the one-step version of the proposed procedure applied to the GLI, c) the SRMRE algorithm on the entire HSIs are showed, along with the confidence ellipsoid at level $\alpha = 0.1$. Also in this case the general trend of the RMR noise distribution along the row and column directions is well represented by the both the described strategies and the one-step procedure on the GLI.

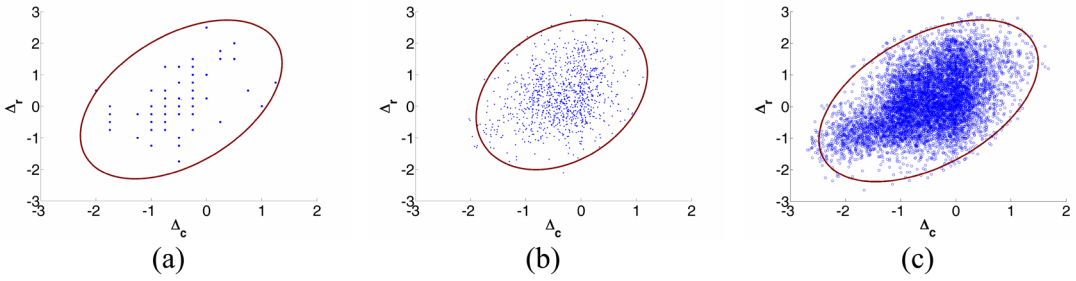

Figure 3.6. Cooke City Dataset: scatterplot of the RMR noise realizations along row (y axis, Δ_r) and column (x axis, Δ_c) direction. (a) Supervised, (b) one-step on the GLI, (c) SRMRE.

The RMR parameters assumed as benchmark along with the estimates obtained with both the SRMRE and the one-step procedure applied to the GLI case (reported in Table 4), have values lower than those observed in the previous example. This is not an unexpected result, because in this example, contrary to the previous case, the two considered images were accurately co-registered by means of a suitable algorithm [73].

Benchmark Values		**Estimated Values**			**RSE**		
	Supervised		**One-step on GLI**	**SRMRE**		**One-step on GLI**	**SRMRE**
N. Pts	60 CPS		1021 KPs	8037 KPs			
$\mu_{\Delta r}$	0.21	$\hat{\mu}_{\Delta r}$	0.36	0.18	$RSE_{\mu_{\Delta r}}$	0.15	0.03
$\mu_{\Delta c}$	-0.46	$\hat{\mu}_{\Delta c}$	-0.35	-0.49	$RSE_{\mu_{\Delta c}}$	0.11	0.03
$\sigma_{\Delta r}$	0.89	$\hat{\sigma}_{\Delta r}$	0.84	0.90	$RSE_{\sigma_{\Delta r}}$	0.05	0.01
$\sigma_{\Delta c}$	0.64	$\hat{\sigma}_{\Delta c}$	0.55	0.70	$RSE_{\sigma_{\Delta c}}$	0.09	0.06
ρ_{Δ}	0.46	$\hat{\rho}_{\Delta}$	0.48	0.30	$RSE_{\rho_{\Delta}}$	0.02	0.16

Table 3.4. RMR noise parameters estimation. Cooke City dataset.

Obviously, in this case, the same remarks reported in the discussion of the results of the previous experiments also hold. Results in Table 3.4 confirm that the SRMRE and the one-step procedure on the GLI give estimates in accordance with the values assumed as benchmark. Once again it is important to stress that the number of observations of the RMR noise extracted by the SRMRE are much higher than those obtained on the GLI and this potentially leads to more accurate estimates. Also in this case to give a numerical example, we have computed the RSE among the estimates and the benchmark values. The analysis shows that the SRMRE gives the lowest RSE values for almost all the RMR parameters. For instance, the RSE on the estimates of $\mu_{\Delta r}$ and $\sigma_{\Delta r}$ provided by the SRMRE are five times lower than those obtained in the GLI case, and the RSE on the estimate of $\mu_{\Delta c}$ obtained with the SRMRE is nearly 4 times lower than

that obtained on the GLI. The estimation of ρ_{Δ} is the only case where the one-step procedure over the GLI outperforms the SRMRE (the RSEs are 0.02 and 0.16 over the GLI and in the SRMRE case, respectively).

3.5 Conclusions

In this chapter the SRMRE algorithm has been proposed for the estimation of the first and second order statistics of the RMR noise. One of the motivations of the present work stems from the need to quantify the RMR in ACD applications where it represents a crucial issue for the detection performance. Particularly, RMR noise characterization is of great interest for a class of ACD algorithms (LCRA) which has been recently proposed to cope with the problem of the performance degradation due to RMR noise. The LCRA approach embeds in the change detection scheme a specific UW whose dimensions must be set according to the magnitude of the RMR noise. In fact the UW size determines the spatial resolution of the change detector, meaning that if a target reallocation really occurs, its detection could be missed due to the choice of the window dimensions. Nevertheless, it should be large enough to allow the RMR effects to be compensated. Existing methods proposed to characterize the RMR noise, make use of ancillary data, such as the GPS-INS and DEM errors, which are not always available and they do not account for the errors due to the co-registration algorithms. On the contrary, the proposed SRMRE algorithm is fully unsupervised, in that it does not require ancillary data and it characterizes the RMR noise by analyzing directly the test and the reference images accounting also for the errors induced by co-registration algorithms. SRMRE is based on the SIFT procedure, which was developed to work on gray level images, and extends its application to HSI. The SIFT technique has been demonstrated to show great performance among the local descriptors algorithms. The method proposed here further improves the SIFT performance by exploiting all the spectral content of the HSI and properly filtering the descriptor errors. In particular, this is achieved by means of a sequential architecture, that jointly exploits the potential distinctive spectral features in different bands of the HSI, the SIFT detector and the

MCD algorithm in order to provide robust estimate of the RMR noise parameters. The estimates of the RMR noise mean vector ($\hat{\boldsymbol{\mu}}_{\Delta}$) and of its covariance matrix ($\hat{\boldsymbol{\Gamma}}_{\Delta}$) provided by the proposed method can be actually used to design directional UW windows adapting both its direction and sizes in the image plane to the real characteristics of the RMR noise.

The results provided by the SRMRE have been analyzed on two different real HSIs. In particular, two different case studies have been considered. First, two geo-referenced HSIs collected over a rural scenario in similar illumination conditions have been tested providing an example of the use of the SRMRE in the so called direct geo-referencing applications. The estimates given by the SRMRE have been compared with the benchmark values obtained by means of a supervised technique. The analysis showed that the SRMRE provides results in accordance with the benchmark values and that the estimates are obtained from a number of observations much higher than that extracted by a version of the algorithm working on single-band images (GLI). Such images are constructed as a linear combination of the spectral bands corresponding to the Red, Green and Blue spectral ranges of the original HSIs. The higher number of RMR noise observations extracted by the SRMRE makes such an algorithm potentially more accurate than that based on the one-step procedure applied to the GLI.

The second test has been conducted on a pair of HSIs co-registered by using ground control points and collected over a scenario, composed of rural and urban areas, in variable illumination and shadow conditions. The analysis has emphasized both the effectiveness of the SRMRE in estimating the RMR noise due to the co-registration processing and the robustness of the SRMRE algorithm even when no preliminary processing had been performed in order to make the two images radiometrically comparable. In this case study we observed that the modified version of the algorithm working on single band images, though providing estimates in accordance with the benchmark values, did not derive such estimates on KP pairs located all over the images. They were concentrated in the urban area, the regions with difference in illumination conditions and shadow were not accounted for and their number was almost eight times lower than that obtained with the SRMRE.

It is worth noting that, in the case of scarcely textured images or significant variation in illumination and shadow conditions, the exploitation of the entire HSI by means of the SRMRE algorithm is mandatory in order to guarantee accurate estimation of the RMR noise parameters. If the images are well textured, it is also possible to adopt the proposed method to a selected channel or to a single image obtained as a linear combination of spectral bands of the original dataset, trading off the performance degradation in the estimation of the RMR noise parameters with a reduced computational load.

As claimed in the previous part of the chapter, one of the interesting applications of the results provided by the SRMRE consists in involving the estimated values $\hat{\mu}_{\Delta_S}$, $\hat{\mu}_{\Delta_L}$, $\hat{\sigma}_{\Delta S}$ and $\hat{\sigma}_{\Delta L}$ in the design of the UW adopted by LCRA based ACDs. To give an example, the UW associated to the PUT located in $\boldsymbol{\eta}_X(\boldsymbol{\zeta}) = [r_X, c_X]^{\mathrm{T}}$, should be designed so as to be centred in $\left[r_X + \hat{\mu}_{\Delta_S}, c_X + \hat{\mu}_{\Delta_L}\right]^{\mathrm{T}}$ and with size proportional to the estimated RMR standard deviations $\hat{\sigma}_{\Delta S}$ and $\hat{\sigma}_{\Delta L}$ along the sample and line directions, respectively. If we use a rectangular UW it should have a size of $3 \div 5 \cdot \hat{\sigma}_{\Delta S}$ and $3 \div 5 \cdot \hat{\sigma}_{\Delta L}$ pixels in both the spatial directions in order to account for the RMR noise.

The proposed method has been implemented in Matlab achieving satisfactory results from a computational load point of view. The analysis has been carried out on a Windows 7 64 bit PC equipped with Intel Core i7 860@2.8GHz processor and 8GB of available RAM. In particular, the total computation time was found to be $T_V^{TOT} \approx 5\,\mathrm{min}$ and $T_V^{TOT} \approx 14\,\mathrm{min}$ for the Virginia City and the Cooke City test data respectively, corresponding to an average computation time for each spectral channel $T_V^{Ch} \approx 1\,\mathrm{sec}$ and $T_V^{Ch} \approx 6\,\mathrm{sec}$. It is worth noting that the Matlab code of the proposed algorithm has not been optimized since this task is out of the scope of this work. However, the possibility to achieve real time performance represents an interesting opportunity which is actually under investigation.

We would also like to stress that, in this work we modelled RMR noise as a wide-sense stationary process. Such an assumption is sufficiently realistic in that, typically, slowly

varying conditions, in terms of pressure gradient, Rossby waves and jet streams characterize the data acquisition. However, especially in the case of images spanning very large geographical areas, the RMR noise might have different statistical parameters in distinct (and large) regions of the analyzed images. In such case the basic idea of the proposed algorithm should be effectively exploited to obtain different estimates of the RMR noise associated to distinct regions of the images by taking advantage of the high cardinality and the uniform spatial distribution of the KPs pairs obtained by iterating the SIFT and the KPs matching procedures all over the spectral bands. This will be the focus of our future research activity.

As a concluding remark, it is worth noting that the proposed method, which sequentially exploits multiple image bands, can potentially be extended to different applications, such as 3D surfaces reconstruction, where different images of the scene are sequentially collected in the time domain at different viewpoints ([74],[75]).

Chapter 4

A novel strategy for Adaptive ACD (AACD)

In this chapter a novel adaptive scheme for ACD in HSI is presented. The technique mitigates the negative effects due to random noise, by means of a band selection technique aimed at discarding spectral channels whose useful signal content is low compared to the noise contribution. Band selection is performed on a per-pixel basis by exploiting the estimates of the noise variance accounting also for the presence of the signal dependent noise component. Real data collected by a new generation airborne hyperspectral camera on a complex urban scenario are considered to test the proposed method. Performance evaluation shows the effectiveness of the proposed approach with respect to a previously proposed ACD algorithm based on the same similarity measure.

4.1 Signal model

We start by introducing the model adopted for the generic pixel of the hyperspectral images used in the ACD task. For this purpose, let us denote as $\mathbf{y}(i,j)$ the pixel vector of the collected at-sensor radiance. It is modeled as an $L \times 1$ random vector (RV) in the spatial position (i,j) (i and j are the row and the column indexes respectively), where L represents the number of sensor spectral channels. According to the model recently introduced in [82] and [83], $\mathbf{y}(i,j)$ can be modeled as the sum of two terms: the useful signal $\mathbf{x}(i,j) = [x_1(i,j), x_2(i,j), ..., x_L(i,j)]^T$ and the noise term $\mathbf{N}(i,j,\mathbf{x}(i,j))$ which is generally dependent on the signal:

$$\mathbf{y}(i,j) = \mathbf{x}(i,j) + \mathbf{N}(i,j,\mathbf{x}(i,j)) \tag{4.1}$$

$\mathbf{x}(i,j)$ is the sensor's measured signal due to the radiation reflected and/or emitted by the materials in the spatial resolution cell corresponding to the coordinates (i,j), i.e. it is the actual information content of $\mathbf{y}(i,j)$. For this reason, throughout the document we will refer to $\mathbf{x}(i,j)$ as "useful signal".

$\mathbf{N}(i,j,\mathbf{x}(i,j))$ is the zero mean random noise which can be modeled as the sum of two contributions, the photon noise ($\mathbf{N}^{ph}(i,j,\mathbf{x}(i,j))$), due to the random nature of the photon arrival process, and the thermal or electronic noise ($\mathbf{N}^{th}(i,j)$), related to the electronic components. Since they refer to distinct physical phenomena, they are assumed to be statistically independent. In particular, $\mathbf{N}^{ph}(i,j,\mathbf{x}(i,j)) = \left[N_1^{ph}(i,j,x_1(i,j)), ..., N_L^{ph}(i,j,x_L(i,j))\right]^T$ is modeled as an uncorrelated zero mean Gaussian random vector. Specifically, the contribution of the photon noise in the *l*-th band ($N_l^{ph}(i,j,x_l(i,j))$) is modeled as a zero mean Gaussian RV with variance depending on the useful signal level $x_l(i,j)$:

$$N_l^{ph}(i,j,x_l(i,j)) = \sqrt{\gamma_{SD,l} \cdot x_l(i,j)} \cdot W_l^{ph}(i,j) \tag{4.2}$$

In (4.2) $W_l^{ph}(i,j)$ is a standard Gaussian distributed RV statistically independent on $\mathbf{x}(i,j)$. The electronic noise $\mathbf{N}^{th}(i,j)$ is modeled as a zero mean uncorrelated Gaussian

random vector with distinct variances for each component. The *l*-th component $N_l^{th}(i,j)$ of the electronic noise $\mathbf{N}^{th}(i,j)$ can be modeled as:

$$N_l^{th}(i,j) = \sqrt{\gamma_{SI,l}} \cdot W_l^{th}(i,j) \tag{4.3}$$

where $W_l^{th}(i,j)$ is a standard Gaussian distributed random variable statistically independent on $\mathbf{x}(i,j)$, and $\gamma_{SI,l}$ is the variance of $N_l^{th}(i,j)$. $\mathbf{N}(i,j,\mathbf{x}(i,j))$ is an uncorrelated Gaussian distributed RV with zero mean and covariance matrix depending on $\mathbf{x}(i,j)$:

$$\begin{aligned} &\mathbf{N}(i,j,\mathbf{x}(i,j)) = \mathbf{\Lambda}^{\frac{1}{2}}(\mathbf{x}(i,j)) \cdot \mathbf{W}(i,j) \\ &\mathbf{\Lambda}(\mathbf{x}(i,j)) = diag\{\lambda_1(x_1(i,j)),...,\lambda_L(x_L(i,j))\} \end{aligned} \tag{4.4}$$

where, according to (4.2) and (4.3):

$$\lambda_l(x_l(i,j)) = \gamma_{SD,l} x_l(i,j) + \gamma_{SI,l} \tag{4.5}$$

4.2 Adaptive band selection ACD (ABS-ACD)

In detection applications, the presence of random noise is obviously detrimental for the performance of ACD algorithms in measuring the similarity between two given spectral vectors. In particular, we have experienced the poor performance of ACD for those pixels having several bands where the useful signal is not sufficiently high with respect to the noise level. This results in an increased false alarms probability because the change detection statistic obtained by applying a method for ACD tends to be high in the regions whose spectral signatures have low values in a certain number of spectral bands. Such a problem has been encountered in processing hyperspectral data collected in the VNIR (Visible and Near Infrared) spectral range and containing sea regions or shadowed areas.

A possible way to improve the robustness of the ACD to the random noise is that of applying it after band selection, i.e. after selecting a set of spectral channels where the observed spectral signatures sufficiently differ from the random noise. Since both the

useful signal level and the noise in a given band strongly depend on the spectral characteristics of the observed material, the selected bands cannot be the same for each pixel. As a consequence, band selection has to be performed in an adaptive fashion and on a per-pixel basis. This is the rationale of the adaptive band selection strategy proposed in this chapter and detailed in the following.

For simplicity, let us start assuming that the random noise $\mathbf{N}(i,j,\mathbf{x}(i,j))$ in the model in equation (4.1) has unit variance in each band, i.e.: $\mathbf{\Lambda}(\mathbf{x}(i,j))=\mathbf{I}_{L\times L}$, $\mathbf{I}_{L\times L}$ being the $L\times L$ identity matrix. For a given spectral pixel $\mathbf{y}$ (the dependence on the spatial coordinates is omitted to simplify the notation) the bands to be retained, i.e. the bands where the useful signal is sufficiently higher than the random noise, can be selected by resorting to the statistical decision theory. In particular, for the observation $y_l = x_l + N_l$ in the *l-th* band, we search for the values of x_l that make it detectable with respect to N_l (having unit variance). In the case of Gaussian noise, the statistical decision theory provides the relationship between the detection performance in terms of detection probability (p_d) and false alarms probability (p_f) and the Signal to Noise Ratio (SNR), i.e.: the ratio between the squared value of the useful signal (x_l^2) and the noise variance ($E\{N_l^2\}$). In particular, for a given pair of p_d and p_f, the SNR in the *l*-th band (d_l) must be greater than the upper bound d_{UB} defined in the following equation.

$$\begin{aligned} d_l &= \frac{x_l^2}{E\{N_l^2\}} = x_l^2 \geq d_{UB} \\ d_{UB} &= \left[Q^{-1}(p_f) - Q^{-1}(p_d)\right]^2 \end{aligned} \tag{4.6}$$

In equation (4.6) $Q^{-1}(\ )$ is the inverse of the *Q*-function (the tail probability of the standard normal distribution). equation (4.6) provides the criterion to select the bands to be retained on the basis of the detection performance in terms of p_d and p_f. The bands to be retained are those having SNR higher than that required to make the useful signal detectable with respect to the noise. Detectability is quantified in terms of p_d and p_f (typically $p_d \cong 1$ and $p_f << 1$). Notice that, in practice, d_l is not known and must be

estimated from the noisy observation y_l. It can be easily proved that the Maximum-Likelihood (ML) estimate of d for a given y_l is $\hat{d} = y_l^2 - 1$.

According to these theoretical remarks, the selection of the bands to be used in the adaptive approach is performed on a per-pixel basis by analysing the PUT $\mathbf{y}(i,j)$. For two fixed values of p_d and p_f, which guarantee high distinctiveness between the useful signal and the random noise ($p_d \cong 1$ and $p_f << 1$), the set of bands $B(i,j;p_f,p_d)$ to be retained in comparing $\mathbf{y}(i,j)$ with each $\mathbf{z}(r,c)$ in $UW(i,j)$ is defined as:

$$\begin{aligned} &B(i,j;p_f,p_d) \equiv \left\{ l^* \in [1,...,L]:\ \hat{d}_{l^*}(i,j) \geq d_{UB}(p_f,p_d) \right\} \\ &d_{UB}(p_f,p_d) = \left[Q^{-1}(p_f) - Q^{-1}(p_d) \right]^2 \\ &\hat{d}_{l^*}(i,j) = y_{l^*}^2(i,j) - 1 \end{aligned} \tag{4.7}$$

It is worth reminding that the per-pixel band selection strategy summarised in equation (4.7) has been derived assuming that the random noise has unit variance in each band. Of course, since this assumption does not hold in practise, we propose to apply a suitable transformation to the original data (both $\mathbf{Y}$ and $\mathbf{Z}$) in order to have unit noise variance in each band. Specifically, we propose to perform such noise whitening (NW, hereinafter) by using the estimated standard deviation (std) per pixel and per band as a normalization factor. For this purpose, we resort to the HYperspectral Noise Parameter Estimation (HYNPE, [82]) algorithm which combines an ML estimator with a well known Multi-Linear Regression approach ([84], [85]) to obtain the estimates $\hat{\gamma}_{SD,l}$ and $\hat{\gamma}_{SI,l}$ of the parameters of the noise model in (4.4) and (4.5) and the noise variance estimates per pixel and per band. With reference to the pixels of the test image and according to the model in (4.4) and (4.5), NW is performed as follows:

$$y_l^{(w)}(i,j) = \frac{y_l(i,j)}{\sqrt{\hat{\gamma}_{SD,l} \cdot \hat{x}_l(i,j) + \hat{\gamma}_{SI,l}}} \tag{4.8}$$

In (4.8), $y_l^{(w)}(i,j)$ is the noise whitened version of $y_l(i,j)$ and $\hat{x}_l(i,j)$ is the estimate of the useful signal in the *l-th* band obtained by means of the MLR based method. NW on the reference image is obtained by following the same procedure.

To conclude, the solution that we propose for the adaptive band selection procedure for ACD is as follows:

- the noise standard deviation for each pixel and in each band of the two images $\mathbf{Y}$ and $\mathbf{Z}$ is estimated by combining the MLR approach for signal estimation and the HYNPE for noise parameters estimation;
- NW is performed on both the images by dividing each pixel for the corresponding estimated noise standard deviation. NW produces the two images $\mathbf{Y}^{(w)}$ and $\mathbf{Z}^{(w)}$ with normalized noise variance;
- the CE ([1]) transform is applied to the reference image in order to compensate the differences in the illumination atmospheric and environmental conditions;
- for each spatial position (i,j) the set $B(i,j;p_f,p_d)$ of the bands to be retained is selected by applying the proposed procedure to the PUT. i.e. the pixel of the noise whitened test image $\mathbf{y}^{(w)}(i,j)$:

$$B(i,j;p_f,p_d) \equiv \left\{ l^* \in [1,\ldots,L]:\ \hat{d}_{l^*}(i,j) \geq d(p_f,p_d) \right\} \quad (4.9)$$
$$\hat{d}_{l^*}(i,j) = \left[y_{l^*}^{(w)}(i,j) \right]^2 - 1$$

- ACD is applied by considering only the selected bands:

$$S_{ABD}(i,j) = S\left[\tilde{\mathbf{y}}^{(w)}(i,j), \tilde{\mathbf{z}}^{(w)}(i,j) \right] \quad (4.10)$$
$$\tilde{\mathbf{y}}^{(w)}(i,j) = \left\{ y_{l^*}^{(w)}(i,j) : l^* \in B(i,j;p_f,p_d) \right\},$$
$$\tilde{\mathbf{z}}^{(w)}(i,j) = \left\{ z_{l^*}^{(w)}(i,j) : l^* \in B(i,j;p_f,p_d) \right\}$$

In (4.10) we used the notation $z_k^{(w)}(r,c)$ to denote the component in the *k-th* band of the pixel $\mathbf{z}^{(w)}(r,c)$ of the noise whitened reference image $\mathbf{Z}^{(w)}$. It is worth noting that the selected bands are not the same for all the pixels and they depend on the two input parameters p_f and p_d which, in turn, determine the values of the threshold $d(p_f,p_d)$. As a concluding remark, we would like to stress that, regardless of the adopted similarity measure, the Adaptive Band Selection (ABS) strategy can be exploited in all

the pixel wise ACD techniques whose statistic $S(i,j)$ results from a pixel per pixel comparison between corresponding pixels of the test and the reference image.

4.3 Experimental results

The performance of the ABS strategy has been tested on a real hyperspectral dataset. Due to adverse atmospheric conditions (i.e. cloud cover of 8 oktas and wind speed of 45kts at the flight altitude), data acquisition was very challenging. In particular, two images strips were collected with a SIM-GA camera from SELEX GALILEO installed onboard a small aircraft. A ground truth map has been documented over an urban scenario with additional information provided by a very high resolution RGB camera installed on a second aircraft flying a few minutes apart. Several targets have been evaluated, spanning in size from two to five meters. The images, characterized by a spatial resolution of about 1m, have been direct geo-referenced by means of ancillary data (GPS-INS). Furthermore, the residual striping noise in both the images has been reduced by resorting to the method detailed in [85] and [86]. The main characteristics of the collected dataset are reported in Table 4.1.

SIMGA HSI	
Spectral Range	400 - 1000 nm
Spectral Sampling	≈ 1.2 nm
# Spectral Bands	512
Image Size	220 x 220 px
Focal Length	17 mm
Nominal IFOV per pixel	1 mrad
Spatial Resolution @ 1000 m	1 m
Field of View (FOV)	± 19°
F#	2.0

Table 4.1. SIM-GA Sensor. Main characteristic of the Zeebrugge dataset

In Figure 4.1 (a) and (b) we show the RGB representation of the test image and the reference image, respectively. In Figure 4.2 the ground truth (GT) for the anomalous changes (or targets T1-T8) is highlighted with yellow circles.

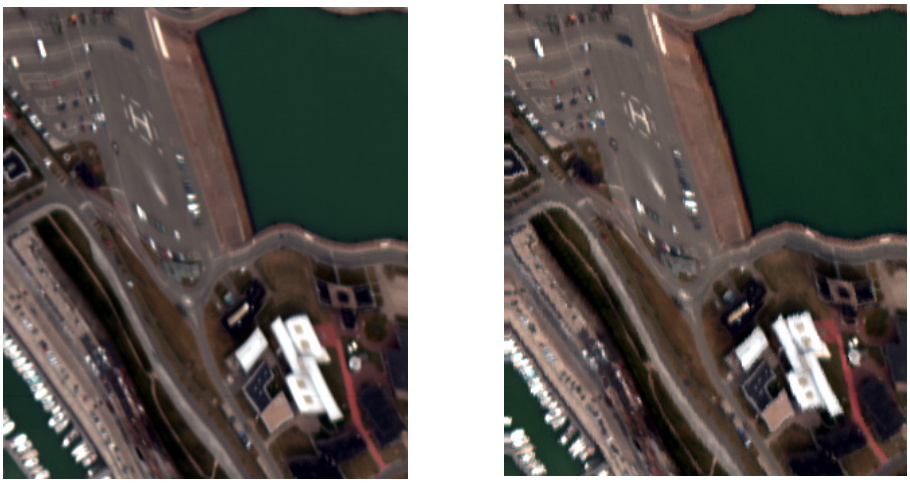

(a) (b)

Figure 4.1. RGB representation of the HSI. (a) Test Image. (b) Reference Image.

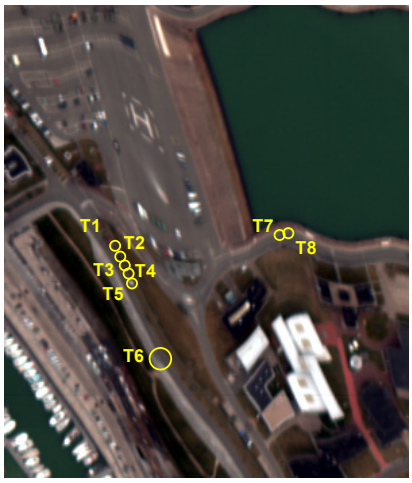

Figure 4.2. Ground truth of the collected HSI. The anomalous changes (*deletions*) are highlighted with yellow circles: two vehicles in the top right, five vehicles in the top left and one vehicle in the middle left.

In Figure 4.3 we report the picture collected with the high spatial resolution camera of the considered targets: in particular the two cars in Figure 4.3 (a) represent the

anomalous changes T7 and T8 of Figure 4.2, whereas the vehicles in (b) (starting from right, except the red car) represent the anomalous changes T1-T5 of Figure 4.2. The change T6 is an opportunity change (vehicle) whose high resolution picture is not available.

(a) (b)

Figure 4.3: RGB detail collected with an high spatial resolution camera for the changes T1-T8 (except for T6): (a) two vehicles referring to the targets T7 and T8; (b) starting from the right: white car (T1), pick up (T2), blue car (T3), white bike (T4), pick up (T5).

We make reference to a detector based on the SAM metric embedded in the framework of the LCRA approach. The UW to be adopted in the LCRA is designed using the estimates of the standard deviation of the RMR noise in the row and column directions provided by the SRMRE algorithm ([81]). Particularly, according to the estimates given by the SRMRE, we have used a rectangular UW with $R = C = 6$.

In Figure 4.4 we show the result of the SAM-LCRA applied to the original data ($L = 512$). The CE transformation has been applied to the reference image $\mathbf{Z}$ in order to compensate the differences in the acquisition conditions. Figure 4.4 (a) shows the ACD statistic $S_{SAM-LCRA}(i, j)$ in terms of hyper-angle measured in degree (see equation (9)). Figure 4.4 (b) shows the probability density function (PDF) of the unchanged areas (background, hereinafter) estimated from all the pixels of the image statistic except for those associated to the targets T1-T8 (included in the GT map). Furthermore, on the same figure we have highlighted (red bar) the maximum values of the ACD statistic for all the targets in the GT map.

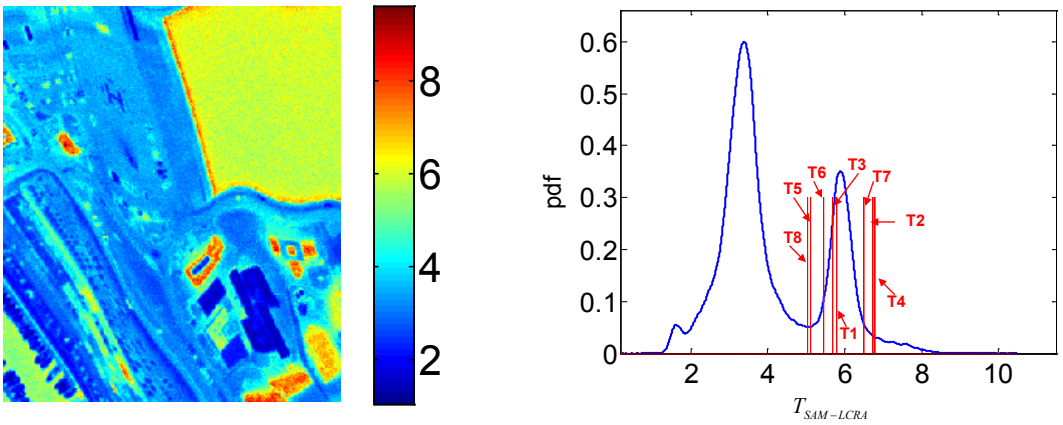

(a) (b)

Figure 4.4: (a) ACD statistic (in degrees) of the SAM-LCRA applied to the original data. (b) Probability density function of the ACD statistic estimated on the background region, the maximum values of the ACD statistic for T1-T8 have been superimposed (red bars).

Notice that the ACD statistic assumes high values in the sea regions at the top-right and at the bottom-left of the scene, in the brown buildings and in the shadowed regions (compare Figure 4.4 (a) with the RGB representation of the test image in Figure 4.1 (a)). Furthermore, it can be noticed that the changes T1-T8 are not easily detectable because they have ACD statistic values very similar to those obtained in unchanged areas (sea regions or shadowed areas). This is confirmed by the results in Figure 4.4 (b) that show that the values of the ACD statistic for T1-T8 are included in the body (and not in the tails as desired) of the background PDF.

Figure 4.5 (a) and (b) show the ACD statistic obtained by applying the proposed ABS-SAM-LCRA algorithm for the two settings: (a) $p_f = 10^{-5}$ and $p_d = 1 - 10^{-3}$ corresponding to $d_{UB,dB} = 20 \cdot \log_{10} d_{UB}(p_f, p_d) = 17.33 dB$ and $p_f = 10^{-10}$ and (b) $p_d = 1 - 10^{-5}$ corresponding to $d_{UB,dB} = 20.52\, dB$. Figure 4.5 (c) and (d) show the PDF of the ACD statistic estimated on the background region for both the considered settings. In both the cases the maximum value of the ACD statistic for each target in the GT has been superimposed (red bars).

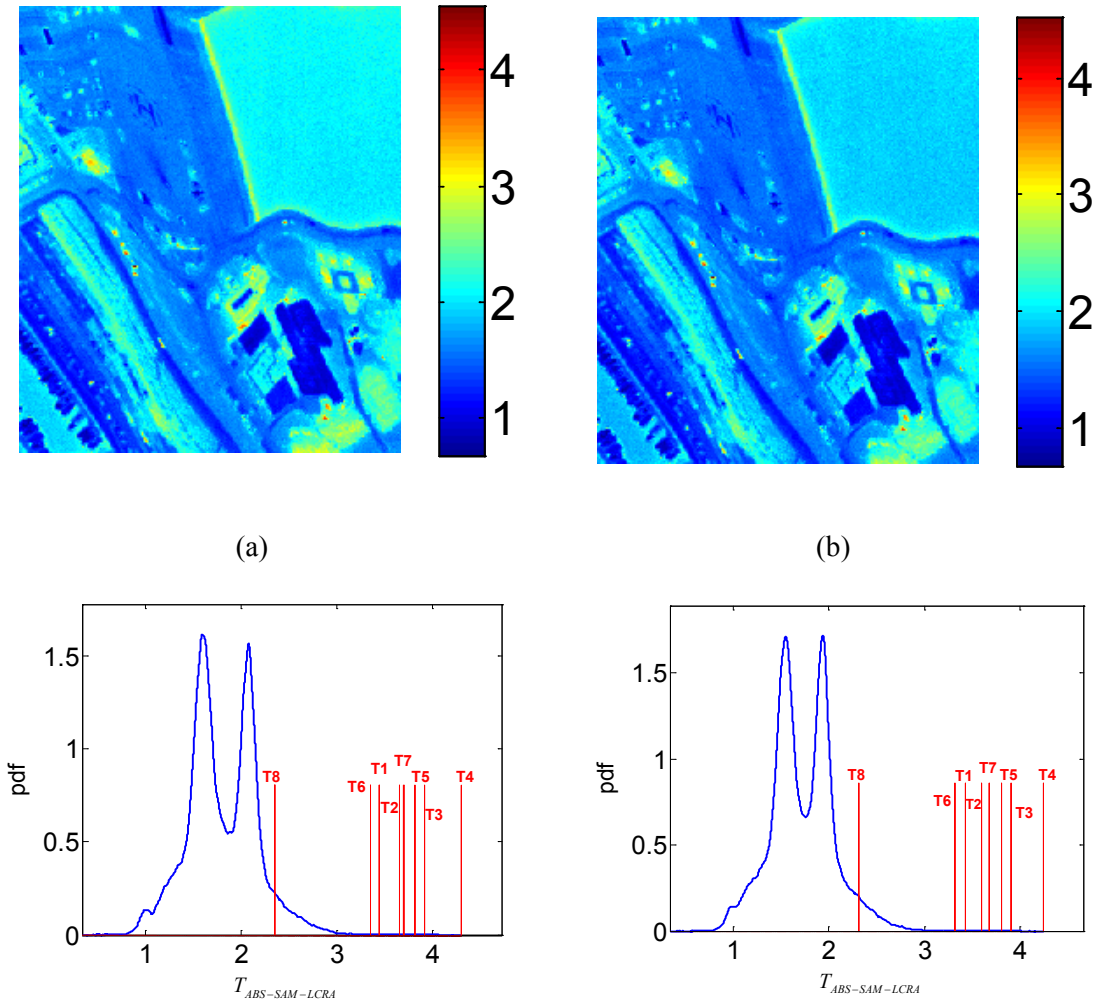

Figure 4.5: (a) - (b) ABS-SAM-LCRA statistic (in degrees) obtained with $p_f = 10^{-5}$ and $p_d = 1-10^{-3}$, and $p_f = 10^{-10}$ and $p_d = 1-10^{-5}$, respectively. (c) - (d) estimated PDF of the ABS-SAM-LCRA statistic on the background in the two cases, the red bars represent the maximum values of the statistics in the pixels corresponding to T1-T8.

Figure 4.5 (a) and (b) show that, by applying the proposed method, the ACD statistic values on the targets T1-T7 are higher than the values obtained on the sea regions and on the shadowed areas. This is confirmed by the results in Figure 4.5 (c) and (d) where it can be noticed that the ACD values on the targets T1-T7 are actually in the tails of the background PDF. As is shown in Figure 4 (c) and (d), only one target (namely, the change T8) cannot be easily detected because its ACD statistic falls in the body of the background statistic PDF.

As an example in Figure 4.6 we show the number of bands retained for each image pixels after the proposed ABS strategy. Particularly, Figure 4.6 (a) refers to the setting ($p_f = 10^{-5}$, $p_d = 1 - 10^{-3}$) and Figure 4.6 (b) refers to the setting ($p_f = 10^{-10}$, $p_d = 1 - 10^{-5}$).

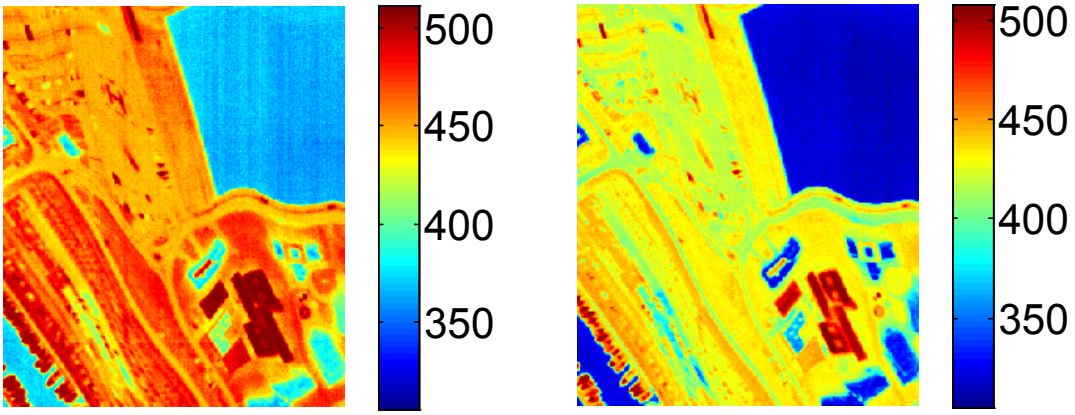

(a) (b)

Figure 4.6: Number of retained bands after the proposed ABS strategy in the case of $p_f = 10^{-5}$, $p_d = 1 - 10^{-3}$ (a) and $p_f = 10^{-10}$, $p_d = 1 - 10^{-5}$ (b)

Figure 4.6 (a) and (b) show that the lowest number of bands is selected in the sea regions, in the brown buildings and in the shadowed areas where it is likely to have low useful signal values especially in the visible (VIS) spectral range. Conversely, the highest number of bands is selected in the white building located in the middle of the scene whose spectrum is characterized by the highest signal values. Furthermore, as expected, the figures show that the number of bands selected with the second setting is smaller than that obtained with the first setting in all the image pixels. To give an example, the number of bands selected in the sea regions with the first setting is in the order of 360, whereas that obtained with the second setting is in the order of 315.

In principle, to assess the performance of a given ACD algorithm experimental Receiver Operating Characteristics (Ex-ROC) should be derived from the available results. Ex-ROC plot the fraction of detected changes or targets (*FoDT*) versus the False Alarm Rate (*FAR*) computed over a particular operating scenario. *FoDT* is computed as the fraction of targets' pixels where the test statistic overcomes a given threshold η. To

compute the *FoDT* a mask of the targets' pixels (Ground Truth- GT) must be available. *FAR*, for a given threshold η, is computed as the ratio between the number of pixels whose test statistic is higher than η and are not true changes (targets) and the total number of background pixels, i.e. the ones outside the GT. In practice, in a change detection problem, it is very difficult to follow this approach because it is actually impossible to include in the GT all the changes occurred in the scene. The possible presence of unknown changes (different from those included in the GT) makes it difficult to assign a practical meaning to the FAR. This is particularly true in very high spatial resolution images of very complex and highly dynamic scenarios, such as the urban one considered in this document. In this case it is expected that, by applying the ACD algorithm, several changes are detected in the scene whose position in the scene is not generally available and included in the GT.

For this reasons, in order to compare the performance of the SAM-LCRA and the ABS-SAM-LCRA (with both the considered settings) for each change within the GT (T1-T8) we have computed two different indexes: the Separability Index (SI) and the False Alarm Rate at the first Detection (FAR@1stD).

For a given change (target) Tk the SI is computed as:

$$SI_{Tk} = \max_{(i,j)\in R_{Tk}} \left\{ \left[\frac{S(i,j) - median_{bkg}(S)}{MAD_{bkg}(S)} \right]^2 \right\} \quad (4.11)$$

where S denotes the ACD statistic, R_{Tk} is the region of the test image occupied by the target Tk, $median_{bkg}(S)$ and $MAD_{bkg}(S)$ are the median and the median absolute deviation (MAD) of the ACD statistic on the unchanged areas (background), respectively. The median and MAD operators are here adopted because of their robustness to potential outliers and furnish an estimate of the mean value and of the standard deviation (except for a multiplicative factor), respectively. SI_{Tk} is a measure of the capability of the ACD algorithm in separating the target Tk from the background. The use of the median and the MAD operators makes the performance index robust to the presence of potential changes not included in the GT.

The FAR@1stD for a given target Tk is obtained by computing the fraction of the pixels included in the background region (outside the GT) whose ACD statistic assumes values higher than λ_{Tk}. This latter is the maximum value of the ACD statistic in the region R_{Tk}. Notice that such an index has the same limitation as the ex-ROC, however it has been included in our analysis for completeness.

In Figure 4.7 we show the values of the SI (in *dB*) for all the considered targets obtained by the SAM-LCRA and the ABS-SAM-LCRA with both the considered settings. Similarly, in Figure 4.8 we show the values of the FAR@1stD in logarithmic scale. The absence of the bars associated to the ABS-SAM-LCRA for T4 means FAR@1stD equal to zero.

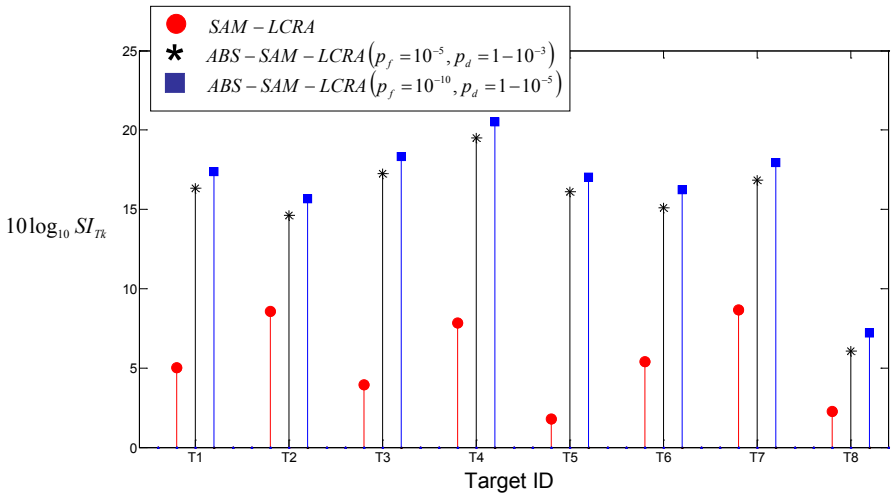

Figure 4.7: values of the SI (in *dB*) obtained for T1-T8 by applying the SAM-LCRA and the ABS-SAM-LCRA with the two considered settings.

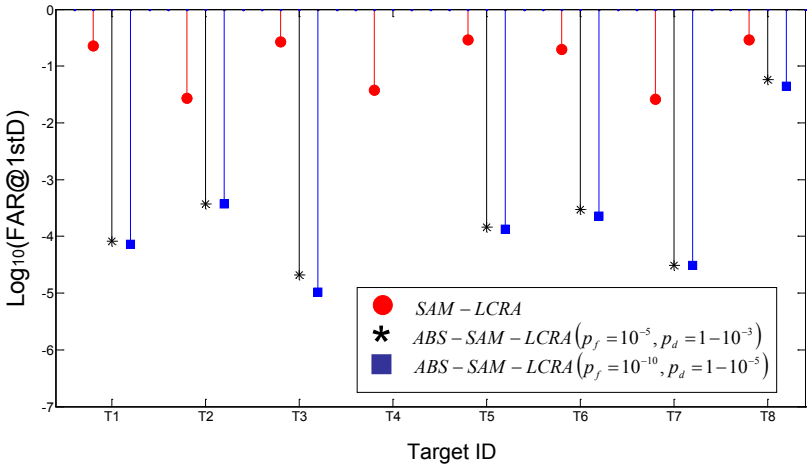

Figure 4.8: values of the FAR@1stD (in logarithmic scale) obtained for T1-T8 by applying the SAM-LCRA and the ABS-SAM-LCRA with the two considered settings.

Figure 4.7 and Figure 4.8 confirm the qualitative conclusion drawn in the previous part of this section. They show the improvement on the ACD performance obtained by the proposed method. Particularly, we can note that:

- using SAM-LCRA, in both the configuration settings, the SI has values more than five *dB* lower than those attained by the proposed algorithm for each of the changes in the GT;
- the values of the FAR@1stD obtained by the ABS-SAM-LCRA are much lower than those provided by the SAM-LCRA. To give a numerical example: the FAR@1stD for T4 is 0.0378 by applying the SAM-LCRA, whereas it is zero by applying the new algorithm.
- the performance of the ABS-SAM-LCRA with the second setting (where less bands are selected) slightly improves with respect to that obtained with the first setting.

Notice that both the SI and the FAR@1stD confirm that the change denoted as T8 is the most difficult to detect for all the experimented methods.

In order to show that the poor performance attained by the SAM-LCRA mainly depends on the presence of the random noise, we have performed a further experiment where the data after spectral binning have been considered. Spectral binning consists in averaging a certain number (two in our case) of contiguous spectral bands in a way that they form a unique channel. Spectral binning results in noise filtering because, being the useful signal highly correlated in the spectral dimension and the random noise actually uncorrelated and with zero mean value, spectral averaging increases the SNR mitigating the effect of noise on the data.

It is worth noting that spectral binning has to be applied with care. In fact, if, on one side, it certainly mitigates the noise effects, on the other hand it tends to "smooth" the spectral signature of the useful signal. Thus, potential discriminative spectral features may be lost as a consequence of such a smoothing effect and this might be detrimental for the performance of ACD (or, more generally, target detection) algorithms.

Figure 4.9 shows the ACD statistic obtained by applying the SAM-LCRA to the data after spectral binning with a factor of 2 ($L = 256$). The CE transformation has been applied to the reference image $\mathbf{z}$ in order to compensate the differences in the acquisition conditions.

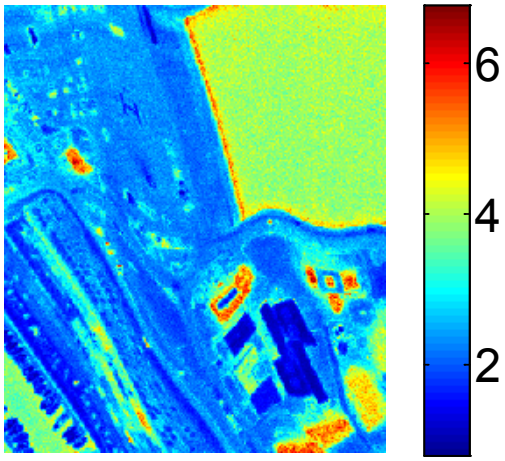

Figure 4.9: ACD statistic (in degrees) of the SAM-LCRA applied to the data obtained after spectral binning with a binning factor of 2.

Notice that also in this case the SAM-LCRA statistic assumes high values in the sea regions at the top-right and at the bottom-left of the scene, in the brown buildings and in the shadowed regions (compare Figure 4.9 with the RGB representation of the test image in Figure 4.1 (a)). It can be also noticed that the changes T1-T8 are not easily detectable, in that they have ACD statistic values very similar to those obtained in unchanged areas (sea regions or shadowed areas). However, the performance of the SAM-LCRA improves in this second data set as is shown by the results in Figure 4.10 and Figure 4.11 that report the comparison between the SAM-LCRA applied to the original data and the data after spectral binning in terms of SI and FAR@1stD, respectively. Figure 4.10 shows that in the data filtered by spectral binning the SAM-LCRA attains the best separability index. Similarly, Figure 4.11 shows that the SAM-LCRA applied to the data after spectral binning has lower false alarm rate for all the targets T1-T8. This in an experimental evidence of the sensitivity of the SAM-LCRA algorithm to random noise.

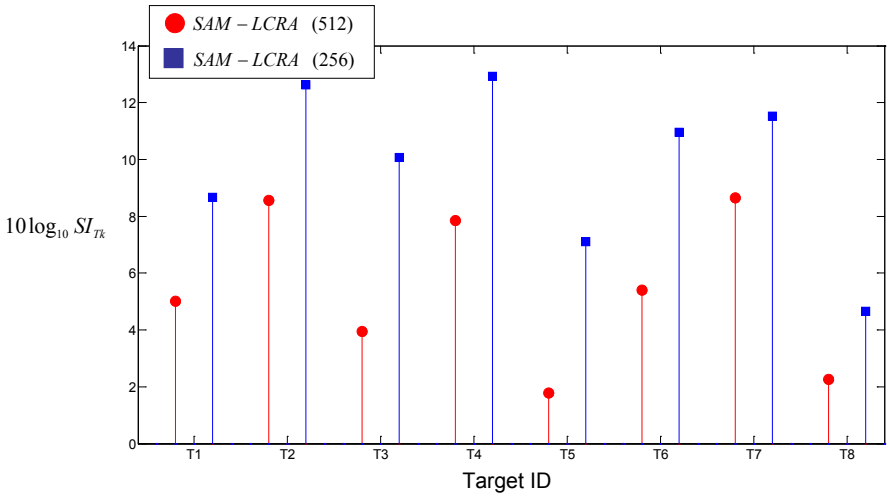

Figure 4.10: values of the SI (in *dB*) obtained for T1-T8 by applying the SAM-LCRA to the original data (512 bands) and to the data after spectral binning (256 bands).

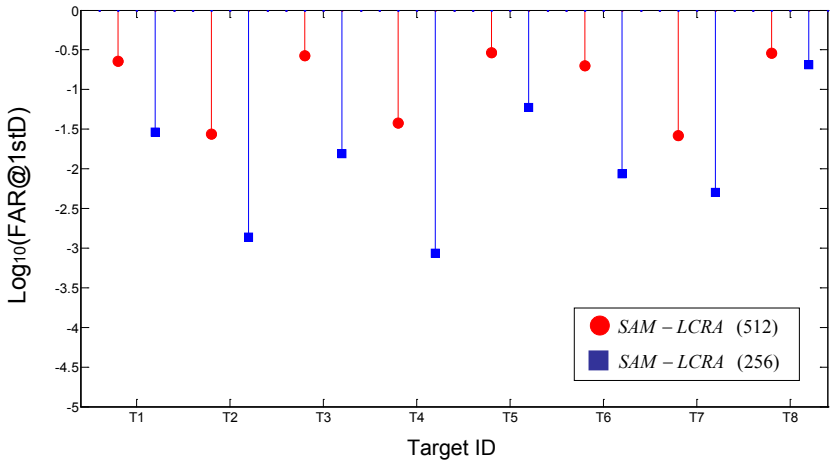

Figure 4.11: values of the FAR@1stD (in logarithmic scale) obtained for T1-T8 by applying the SAM-LCRA to the original data (512 bands) and to the data after spectral binning (256 bands).

In Figure 4.12 we show the results obtained by applying the ABS-SAM-LCRA to the data after binning. Specifically, Figure 4.12 (a) shows the ACD statistic (in degrees) and Figure 4.12 (b) shows the number of selected bands for each pixel. Differently from the previous presented experiment, here we have considered only the setting $p_f = 10^{-10}$, $p_d = 1 - 10^{-5}$ that provides the best performance.

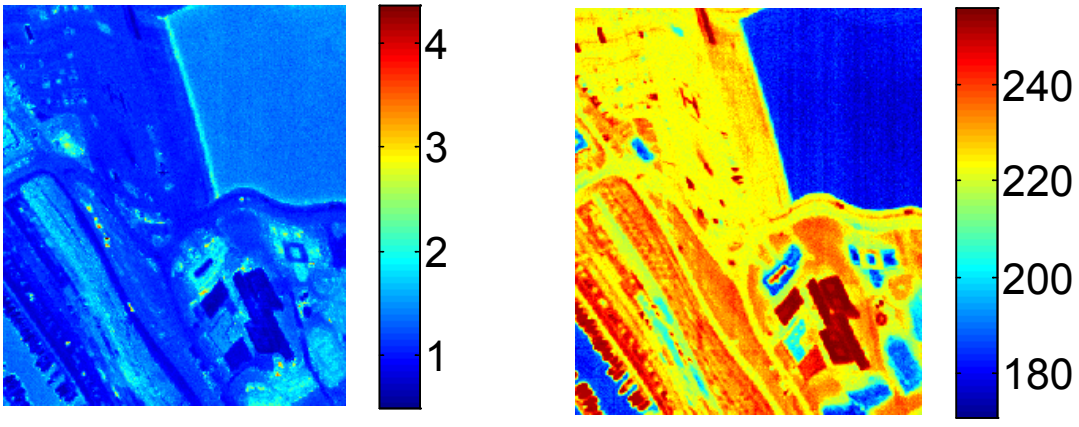

Figure 4.12: (a) ABS-SAM-LCRA statistic (in degrees) obtained with $p_f = 10^{-10}$ and $p_d = 1 - 10^{-5}$ on the data after binning; (b) number of the retained bands for each pixel.

Similarly to the results obtained on the original data ($L = 512$), the lowest number of bands is still selected in the sea regions, in the brown buildings and in the shadowed areas, whereas the highest number of bands is selected over the white building at the bottom-right of the scene. Comparing Figure 4.12 (a) with Figure 4.9, we can appreciate the better separability among T1-T8 and the unchanged areas. Particularly, we can easily notice the reduction of the value of the ACD statistic on the sea regions and on the brown buildings. Such qualitative conclusions are supported by the results presented in Figure 4.13 and Figure 4.14 where the SI and the FAR@1stD values obtained for each target by the SAM-LCRA and the ABS-SAM-LCRA are shown. The new ACD algorithm attains the highest SI values and the smallest FAR@1stD for all the targets.

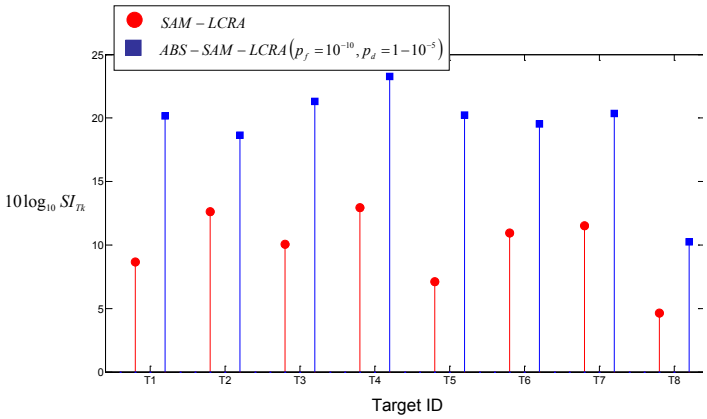

Figure 4.13: values of the SI (in *dB*) obtained for T1-T8 by applying the SAM-LCRA and the ABS-SAM-LCRA to the data after spectral binning (256 bands).

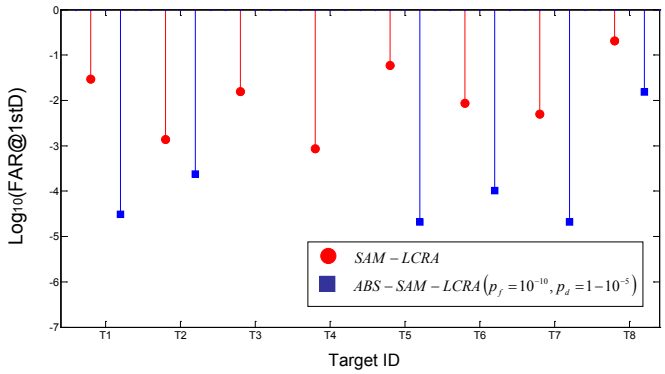

Figure 4.14: values of the FAR@1stD (in logarithmic scale) obtained for T1-T8 by applying the SAM-LCRA and the ABS-SAM-LCRA to the data after spectral binning (256 bands).

Comparing Figure 4.13 and Figure 4.14 with Figure 4.10 and Figure 4.11 we can conclude that the ABS-SAM-LCRA also benefits of the noise mitigation introduced by the spectral binning. In fact, both the SI and the FAR@1stD values obtained on the data after spectral binning are better than those obtained on the original data. However, we would like to stress again that the noise mitigation effect provided by the spectral binning could not be suitable for ACD applications in hyperspectral data. In fact, spectral binning implies a loss in the spectral resolution and can possibly mask relevant spectral features thus preventing the detection of changes occurred in the scene.

4.4 Conclusions

In this chapter we have proposed a robust technique for ACD from airborne HSIs. Particularly, we have approached the problem related to the sensitivity of the algorithm to the presence of random noise. We have proposed a solution to improve the robustness of the ACD algorithm based on an automatic band selection strategy where noisy bands are discarded. Such a strategy is adaptive since, for each PUT, a different number of bands is selected on the basis of the levels of the useful signal and of the random noise in that pixel. The algorithm exploits the estimates of the noise variance per pixel and per band and it also takes into account the presence of the signal dependent noise component in the random noise. This is of paramount importance in applications using data from new generation hyperspectral sensors where the signal dependent noise component is not negligible and cannot be ignored.

Band selection for each pixel is accomplished by retaining only the bands where the useful signal level is high with respect to the noise standard deviation. For this purpose, statistical decision theory has been used to derive a threshold based test to select the spectral channels.

An experimental analysis has been conducted on a real dataset collected by the SIMGA VNIR camera over a urban scenario aimed at evaluating the effectiveness of the proposed method. A scenario arranged *ad hoc* guaranteed numerous changes

between the two images. Several targets have been evaluated spanning in size from two to five meters.

We focused on a specific algorithm (SAM-LCRA) proposed to cope with the presence of the RMR which typically affects data acquired at different times by airborne hyperspectral sensors. Such an algorithm combines the recently proposed LCRA approach with the SAM as a measure of the similarity between two given spectra. The adaptive band selection strategy has been embedded in the SAM-LCRA detection scheme obtaining a new algorithm: the ABS-SAM-LCRA.

Experiments have been performed by applying the SAM-LCRA on the original dataset and on the data after spectral binning which, operating as a low pass filter, mitigates the effects of the random noise. The experiments have shown the improvement on the algorithm performance attained after noise filtering and have indirectly demonstrated the sensitivity of the SAM-LCRA to the noise. The same data sets have been processed by the ABS-SAM-LCRA and the results have demonstrated the effectiveness of the proposed approach, yielding to a consistent improvement of the detection capability with respect to the SAM-LCRA.

Chapter 5

A novel technique for statistical ACD

In this chapter a new ACD technique is proposed considering the common framework based on binary decision theory introduced in Chapter 2. The proposed technique is compared with the previously described approaches. Real data collected by a new generation airborne hyperspectral camera on a complex scenario are exploited to test and compare the presented methods, highlighting advantages and drawbacks of each approach.

5.1 Combined Vector (CV) based ACD (CV-ACD)

In this section we derive new ACD strategies from (2.17) using a different choice of the observation vector and of the secondary data.

It is worth noting that the JV-ACD does not allow the discrimination of anomalous changes occurred in the two images from the spectral anomalies present in both the

images at the same spatial position. To overcome this drawback we propose to measure the degrees of anomalousness of the pixel vector in (i,j) of the test image with respect to the background characterized by the pixels of the reference image.

Thus, in the proposed approach, the observation vector associated to the position (i,j) is the pixel vector of the test image at the same position:

$$\mathbf{e}(i,j) = \mathbf{y}(i,j) \tag{5.1}$$

and the H_0 hypothesis is statistically characterized on the basis of the reference image. This means that we consider as secondary data the pixels of the reference image. For this purpose, we also note that the JV-ACD and the DV-ACD are derived by assuming a *global* Gaussian multivariate distribution for the two images. Though such assumption is commonly used because of its mathematical tractability, it is too simplistic to model the multimodality usually met in real data. A more appropriate model is that adopted to derive the well known RX anomaly detector ([88]) which assumes the *local* Gaussianity of the hyperspectral data. Particularly, hyperspectral data are modeled as a multivariate Gaussian locally stationary random process. The CV based approach proposed in this section uses such local Gaussian model. The assumption of local stationarity for the observations in the two hypotheses is taken into account by considering two different models, leading to two different detectors, the semi-local (CV_{SL}) and the local (CV_L) combined vector detector, respectively.

In the CV_{SL} model, $\mathbf{e}(i,j)|H_0$ is considered as a Gaussian random process having the same covariance matrix $\mathbf{\Gamma}_0$ for all the pixels, and mean vector $\boldsymbol{\mu}_0(i,j)$ assumed to be locally stationary, in the sense that it does not change in a local neighbourhood of the spatial position. According to (2.17), the decision rule associated to the CV_{SL} data model is given by:

$$T_{CV}(i,j) = \left(\mathbf{e}(i,j) - \hat{\boldsymbol{\mu}}_0(i,j)\right)^T \hat{\mathbf{\Gamma}}_0^{-1} \left(\mathbf{e}(i,j) - \hat{\boldsymbol{\mu}}_0(i,j)\right) \underset{H_0}{\overset{H_1}{\gtrless}} \lambda \tag{5.2}$$

$\hat{\mathbf{\Gamma}}_0$ in (5.2), is the ML estimate of $\mathbf{\Gamma}_0$, evaluated exploiting all the pixels of the reference image:

$$\hat{\boldsymbol{\Gamma}}_0 = \frac{1}{N_S \cdot N_L} \sum_{i=1}^{N_S} \sum_{j=1}^{N_L} \left(\mathbf{z}(i,j) - \hat{\boldsymbol{\mu}}_0(i,j)\right) \cdot \left(\mathbf{z}(i,j) - \hat{\boldsymbol{\mu}}_0(i,j)\right)^T \tag{5.3}$$

whereas $\hat{\boldsymbol{\mu}}_0(i,j)$ is the ML estimate of $\boldsymbol{\mu}_0(i,j)$, evaluated considering the reference image pixels included in a given neighbourhood of (i,j). Such a neighbourhood is determined by means of a sliding window $\Omega_\mu(i,j)$ centred at the position (i,j) and capturing N_μ pixels:

$$\hat{\boldsymbol{\mu}}_0(i,j) = \frac{1}{N_\mu} \sum_{(k,l) \in \Omega_\mu(i,j)} \mathbf{z}(k,l) \tag{5.4}$$

In the CV_L model, $\mathbf{e}(i,j)|H_0$ is considered as a Gaussian random process whose mean vector $\boldsymbol{\mu}_0(i,j)$ and covariance matrix $\boldsymbol{\Gamma}_0(i,j)$ are spatially varying but locally stationary, i.e. they do not change in a local neighbourhood of the spatial position (i,j). Particularly, according to the hyperspectral data model in [88] the covariance matrix is assumed to be more slowly spatially-varying than the mean vector. From (2.17), the detector associated to the CV_L model is given by:

$$T_{CV}(i,j) = \left(\mathbf{e}(i,j) - \hat{\boldsymbol{\mu}}_0(i,j)\right)^T \hat{\boldsymbol{\Gamma}}_0(i,j)^{-1} \left(\mathbf{e}(i,j) - \hat{\boldsymbol{\mu}}_0(i,j)\right) \underset{H_0}{\overset{H_1}{\gtrless}} \lambda \tag{5.5}$$

In (5.5), $\hat{\boldsymbol{\mu}}_0(i,j)$ is the ML estimate of $\boldsymbol{\mu}_0(i,j)$, evaluated on N_μ secondary data, whereas $\hat{\boldsymbol{\Gamma}}_0(i,j)$ is the ML estimate of $\boldsymbol{\Gamma}_0(i,j)$, evaluated on N_Γ secondary data. The secondary data are collected from the reference image exploiting two sliding estimation windows $\Omega_\mu(i,j)$ and $\Omega_\Gamma(i,j)$, centered at the position (i,j):

$$\begin{aligned} \hat{\boldsymbol{\mu}}_0(i,j) &= \frac{1}{N_\mu} \sum_{(k,l) \in \Omega_\mu(i,j)} \mathbf{z}(k,l) \\ \hat{\boldsymbol{\Gamma}}_0(i,j) &= \frac{1}{N_\Gamma} \sum_{(k,l) \in \Omega_\Gamma(i,j)} \mathbf{z}(k,l) \cdot \mathbf{z}(k,l)^T - \hat{\boldsymbol{\mu}}_0(i,j) \cdot \hat{\boldsymbol{\mu}}_0(i,j)^T \end{aligned} \tag{5.6}$$

Since the mean vector is supposed to vary spatially faster than the covariance matrix, the dimension of the window used to estimate $\boldsymbol{\mu}_0(i,j)$ is usually smaller than that used

for the covariance matrix $\mathbf{\Gamma}_0(i,j)$, i.e. $N_\mu < N_\Gamma$. The choice of the dimension of the estimation windows is crucial. For example, if on one hand $\Omega_\Gamma(i,j)$ should be large enough to accurately estimate the covariance matrix $\mathbf{\Gamma}_0(i,j)$ (notice that at least $L+1$ samples are needed to guarantee the inversion of the covariance matrix), on the other hand it should be as small as possible to capture a homogeneous background. This is particularly important in complex scenarios, such as in urban areas, where the background is typically highly structured. Moreover, if a target pixel relocates in a different position within $\Omega_\Gamma(i,j)$, it could bias the estimates of $\mathbf{\Gamma}_0(i,j)$ and impair the algorithm performance. Finally, it is important to remark that the computational burden of ACD strategies based on the CV model increases with the size of the estimation windows. In practice, $N_\Gamma = B \cdot L$, $B = 2 \div 5$ represents a good compromise between the two conflicting requirements mentioned above. It is worth noting that the same tradeoff between estimation accuracy and contamination or bias of the estimate also holds in the case of $\hat{\boldsymbol{\mu}}_0(i,j)$. Hereinafter, the detectors derived with the CV_{SL} and the CV_L models will be referred to as CV-ACD-SL and CV-ACD-L, respectively.

The LCRA version of the CV-ACD-SL is obtained by considering $\widetilde{T}_{CV_{SL}}(i,j,r,p)$ as:

$$\widetilde{T}_{CV_{SL}}(i,j,r,p) = \left(\mathbf{e}(i,j) - \hat{\boldsymbol{\mu}}_0(i,j,r,p)\right)^T \cdot \hat{\mathbf{\Gamma}}_0^{-1} \cdot \left(\mathbf{e}(i,j) - \hat{\boldsymbol{\mu}}_0(i,j,r,p)\right) \tag{5.7}$$

where $\mathbf{e}(i,j) = \mathbf{y}(i,j)$, $\hat{\mathbf{\Gamma}}_0$ is obtained globally from the reference image pixels and:

$$\hat{\boldsymbol{\mu}}_0(i,j,r,p) = \frac{1}{N_\mu} \sum_{(k,l) \in \Omega_\mu(i+r,j+p)} \mathbf{z}(k,l) \tag{5.8}$$

In (5.8) $\Omega_\mu(i+r,j+p)$ is the estimation window for the mean vector, centered at the position $(i+r,j+p)$.

Similarly, the LCRA version of the CV-ACD-L is obtained by considering the statistic:

$$\widetilde{T}_{CV_L}(i,j,r,p) = \left(\mathbf{e}(i,j) - \hat{\boldsymbol{\mu}}_0(i,j,r,p)\right)^T \cdot \hat{\mathbf{\Gamma}}_0^{-1}(i,j,r,p) \cdot \left(\mathbf{e}(i,j) - \hat{\boldsymbol{\mu}}_0(i,j,r,p)\right) \tag{5.9}$$

with:

$$\hat{\boldsymbol{\Gamma}}_0(i,j,r,p)=\frac{1}{N_\Gamma}\sum_{(k,l)\in\Omega_\Gamma(i+r,j+p)}\mathbf{z}(k,l)\cdot\mathbf{z}(k,l)^T-\hat{\boldsymbol{\mu}}_0(i,j,r,p)\cdot\hat{\boldsymbol{\mu}}_0(i,j,r,p)^T \tag{5.10}$$

In (5.10) $\Omega_\Gamma(i+r,j+p)$ is the estimation window for the covariance matrix, centered at the position $(i+r,j+p)$.

5.2 Experimental results

To test and compare the effectiveness of the ACD detectors, an experimental analysis has been conducted on a real hyperspectral dataset. Two images have been used in the experiment collected a few days apart with the SIM-GA VNIR camera manufactured by SELEX GALILEO installed onboard a small aircraft. The flight altitude during the acquisitions was around 1000 meters and the corresponding ground spatial resolution was about one meter. The main characteristics of the collected dataset are reported in Table 5.1.

SIM-GA HSI	
Spectral Range	400 - 1000 nm
Spectral Sampling	≈ 1.2 nm
# Spectral Bands	490
Image Size	300 x 340 pixel
Focal Length	17 mm
Nominal IFOV per pixel	1 mrad
Spatial Resolution @ 1000 m	1 m
Field of View (FOV)	± 19°
F#	2.0
Quantization Bits	12 bits
Architecture	Push-broom

Table 5.1. SIM-GA Sensor. Main characteristics of the Mugello dataset

The trial was performed in adverse weather conditions and the image pair, which was only roughly geo-referenced, exhibits a severe residual RMR (in the order of 12 pixels in both the spatial directions). This makes the data set suitable to test the effects of significant RMR in ACD problems. Moreover, the acquired images were affected by striping noise, a typical fixed pattern noise caused in push-broom sensors by relative errors in the calibration of the detectors and by the temporal variation of their responsivity.

An *ad-hoc* scenario was set up in proximity of an airfield for light aircrafts and helicopters. In particular, six man-made targets, spanning in size from two to three meters, were deleted from the scene to generate six anomalous changes (ACs) related to different materials.

In addition, to overcome the inevitable drawback arising from the fact that ACs, being rare, provide few samples to accurately evaluate the statistical performance of the algorithms, we implanted some simulated ACs. Target implanting was accomplished by taking into account the model adopted in [82]. In particular, the pixel vector $\mathbf{y}(i,j)$ of the collected at-sensor radiance is seen as the sum of two terms, the useful signal $\mathbf{s}(i,j)$, related to the radiation reflected and/or emitted by the materials in the spatial resolution cell at the position (i,j), and the noise term $N(i,j,\mathbf{s}(i,j))$, due to different contributions and dependent on the useful signal:

$$\mathbf{y}(i,j)=\mathbf{s}(i,j)+N(i,j,\mathbf{s}(i,j)) \tag{5.11}$$

According to this model, for a given position (i,j) of the test image $\mathbf{Y}$, a synthetic anomalous change, AC_{CA} hereinafter, was obtained by combining the underlying useful signal $\mathbf{s}(i,j)$ with that of a material of the scene picked in a different position (m,n):

$$\mathbf{s}_{CA}(i,j)=\alpha\cdot\mathbf{s}(i,j)+(1-\alpha)\cdot\mathbf{s}(m,n) \tag{5.12}$$

where $0\le\alpha\le1$. In practice, since the two spectra $\mathbf{s}(i,j)$ and $\mathbf{s}(m,n)$ are not available *a priori*, their estimates $\hat{\mathbf{s}}(i,j)$ and $\hat{\mathbf{s}}(m,n)$ have been adopted instead, obtained by exploiting the Multi-Linear Regression approach ([93]). To reproduce a 'camouflage' effect, the spectral signatures $\mathbf{s}(i,j)$ and $\mathbf{s}(m,n)$ were chosen selecting pixels in the image

with similar radiance values in the spectral channels corresponding to the RGB wavelengths, i.e. $s_u(i,j) \approx s_u(m,n)$, $u = [450nm, 550nm, 700nm]$. Furthermore, the noise contribution has been added to all the implanted targets. Noise has been generated according to the model in [94] with the noise parameters estimated from the original image by means of the HYperspectral Noise Parameter Estimation (HYNPE, [55]) algorithm.

In Figure 5.1 (a) and (b) we show the RGB representation of the test image and of the reference image, respectively. In Figure 4.1 (c) the ground truth (GT) of the ACs is highlighted with red and blue squares, related to the six real ACs (which will be referred to "clear" ACs, AC_{CL}, hereinafter) and four AC_{CA}, respectively, resulting in a total of ten ACs.

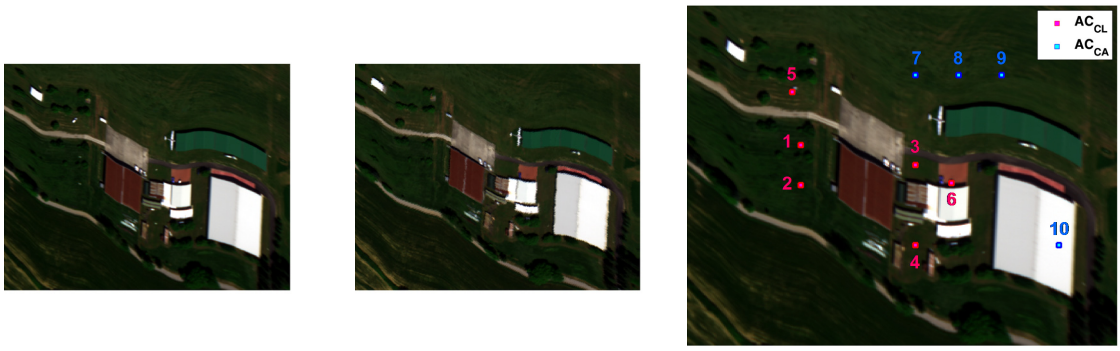

(a) (b) (c)

Figure 5.1: RGB representation of the HSI. (a) Test Image. (b) Reference Image. (c) Scenario Ground Truth, consisting of ten targets removed from the test image. The AC_{CL} are highlighted with red squares (ACs T1 - T6) and the AC_{CA} are highlighted with blue squares (ACs T7 - T10).

In Table 5.2 we summarize the main characteristics of the ACs between the two images. In particular, we report the dimensions of each AC and a short description of their relative properties. Notice that, the AC_{CA} targets T7-T10 where obtained combining materials having the same "colour".

AC ID	SIZE [m]	CLASS	AC PROPERTIES DESCRIPTION
T1	2 x 2	clear	wood panel painted in dark green
T2	2 x 2	clear	wood panel painted in dark green
T3	2 x 2	clear	wood panel painted in dark green
T4	3 x 3	clear	wood panel painted in dark green
T5	2 x 2	clear	white polymeric panel
T6	3 x 3	clear	white polymeric panel
T7	3 x 3	camouflaged	grass - green polymeric panel
T8	3 x 3	camouflaged	grass - green polymeric panel
T9	3 x 3	camouflaged	grass - green polymeric panel
T10	3 x 3	camouflaged	concrete - white polymeric panel

Table 5.2 Main characteristics of the ACs shown in the ground truth

The images have been properly pre-processed to reduce the striping noise and to mitigate the effects of the random noise. In particular, as a first step, residual striping noise in both images has been reduced by the method presented in [85],[86]. In addition, the CE transformation has been applied to the reference image $\mathbf{Z}$ in order to compensate the differences in the acquisition conditions. Furthermore, a spectral binning of a factor 4 was applied to reduce random noise. Thus, the resulting number of spectral bands is $L = 123$.

In Figure 5.2 we show the ACD statistics obtained by the four presented detectors. Notice that, in the experiments the window Ω_μ for the estimation of the mean value $\hat{\boldsymbol{\mu}}_0(i,j)$ in both the CV-ACD-SL and the CV-ACD-L has size 3×3 pixels. In CV-ACD-L the square window Ω_Γ for the estimation of $\hat{\boldsymbol{\Gamma}}_0(i,j)$ has size equal to 15×15 pixels ($N_\Gamma = 225$).

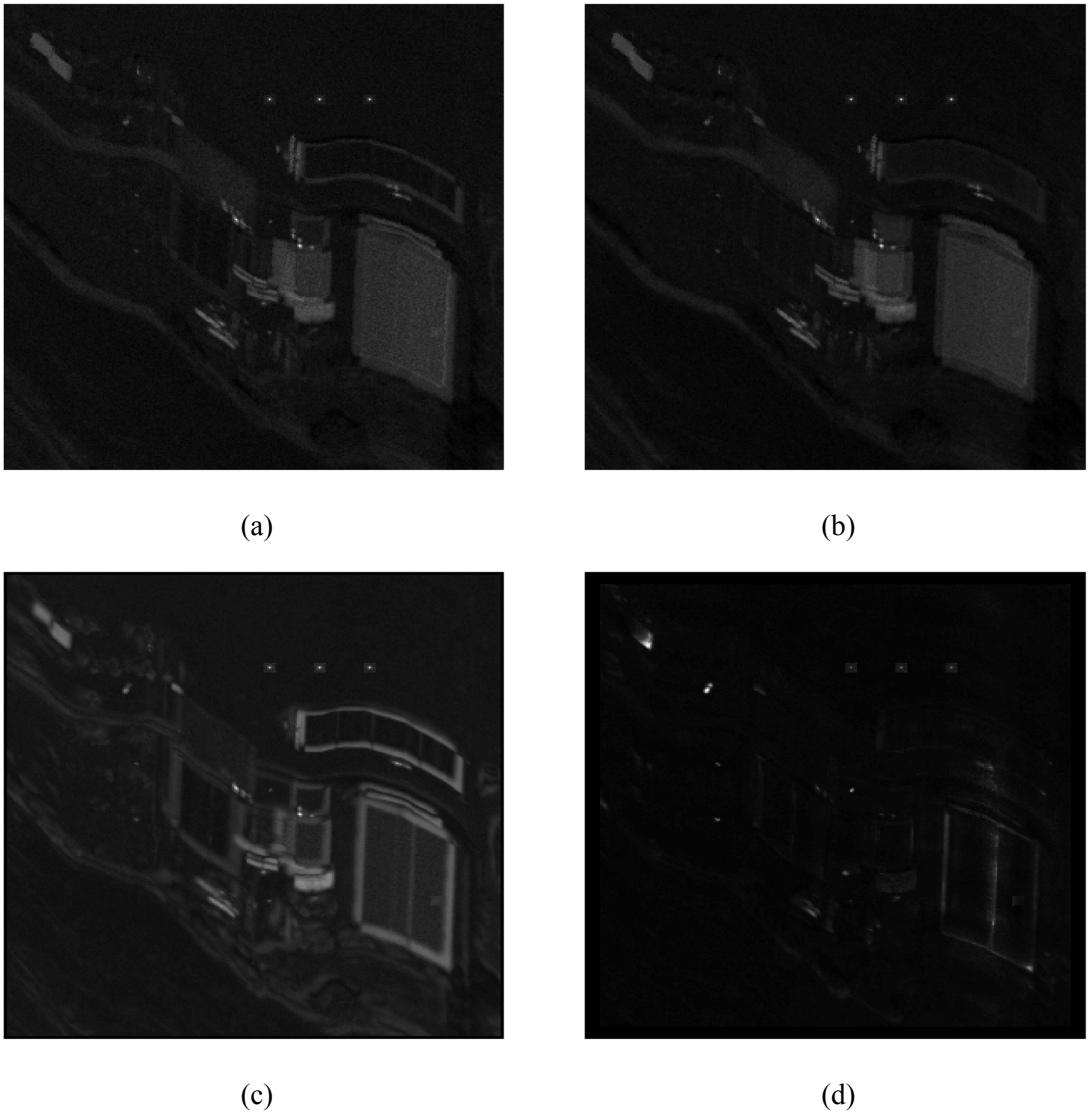

(a) (b)

(c) (d)

Figure 5.2: ACD statistics obtained by means of the: (a) DV-ACD, (b) JV-ACD, (c) CV-ACD-SL, (d) CV-ACD-L.

The ACD statistics associated to the DV-ACD and JV-ACD approaches are quite similar. In fact, the changes T1-T6 are not easily detectable because the values of their ACD statistic is quite similar to those obtained in unchanged areas, while three of the four camouflaged changes (T7, T8 and T9) are well detectable. Notice that the ACD statistic assumes high values in the regions of the two bright buildings located at the center and at the bottom-right of the scene, and in a third building at the upper left corner.

Similar conclusions can be drawn for the CV-ACD-SL approach. In this case, edges and borders between different background classes, mainly the man-made buildings and the vegetation, are seen as spurious detections, indeed confirming the detrimental effects of the RMR. In addition, RMR is clearly visible in the DV-ACD and JV-ACD methods in correspondence of the small aircraft located in the middle of the scene, where the wings seem to be replicated. The performance degradation due to RMR can be also appreciated in the two bright spots located in the center of the scene, exhibiting very high values of the ACD statistic in the DV-ACD, JV-ACD and CV-ACD-SL results. Notice that, in the CV-ACD-SL case the camouflaged white panel (T10) is less visible against the background region than in the DV-ACD and JV-ACD approaches. Conversely, Figure 5.2 (d) shows that the CV-ACD-L yields the best results. In this case, the ACD statistic for the six AC_{CL} T1 - T6 and for three of the four camouflaged changes AC_{CA} (T7, T8 and T9) is well above the values observed in the background region. Differently from the other three approaches, the CV-ACD-L is more robust to the RMR because the window Ω_Γ used to the estimate $\boldsymbol{\Gamma}_0$ tends to partially compensate the RMR. However, this effect is not completely cancelled. Consider, for example, the upper left and bottom right corners, where false detections arise because the magnitude of the RMR exceeds the dimension of the window Ω_Γ.

In order to quantify and compare the performance of the considered ACD algorithms we make use of two performance indexes: the Separability Index (SI) and the False Alarm Rate at the first Detection (FAR@1stDet).

For a given AC Tk, the SI is computed as:

$$SI_{Tk} = \max_{(i,j)\in R_{Tk}} \left\{ \left[\frac{T(i,j) - T_{med}}{T_{MAD}} \right]^2 \right\} \tag{5.13}$$

where R_{Tk} is the region of the test image occupied by the target Tk, and $T_{med} = \underset{(m,n)\in R_{BKG}}{median}\left(T(m,n)\right)$ and $T_{MAD} = \underset{(m,n)\in R_{BKG}}{MAD}\left(T(m,n)\right)$ are the median and the median absolute deviation (MAD) of the ACD statistic on the unchanged background area R_{BKG}, respectively.

The median and the MAD operators are estimators robust to the presence of potential outliers. Particularly, the median is a robust estimator of the mean value and the MAD (except for a multiplicative factor) is a robust estimator of the standard deviation. SI_{Tk} is a measure of the capability of the ACD algorithm to discriminate the target Tk from the background. High values of SI_{Tk} denote high separability between the target and the background. The use of the median and the MAD operators makes the performance index robust to the presence of potential changes not included in the GT.

The FAR@1stDet for a given target Tk is obtained by computing the fraction of the pixels included in the unchanged background area R_{BKG} whose ACD statistic assumes values higher than the threshold λ_{Tk}. Such a threshold is the maximum value of the ACD statistic in the region R_{Tk}, i.e. $\lambda_{Tk} = \max_{(i,j)\in R_{Tk}} (T(i,j))$.

In Figure 5.3 we show the values of the SI (in *dB*) for all the considered targets obtained using the four ACD methods discussed in this work.

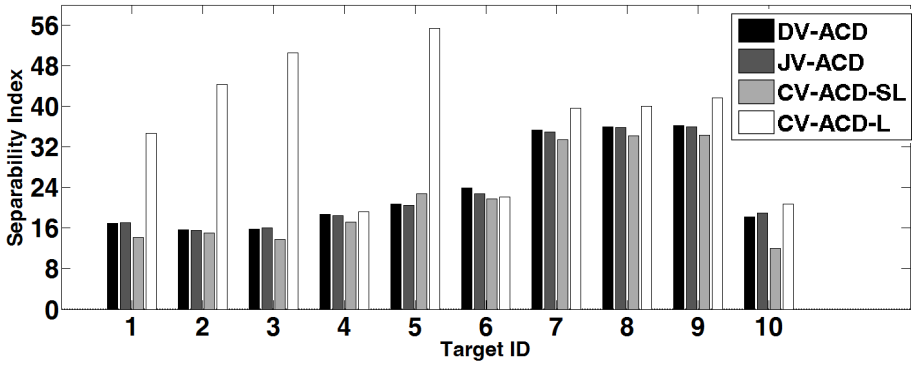

Figure 5.3: values of the SI (in *dB*) obtained for T1-T10 by applying the different algorithms. DV-ACD - black, JV-ACD - dark gray, CV-ACD-SL - light gray, CV-ACD-L - white.

In Figure 5.4 we show the values of the FAR@1stDet in logarithmic scale. The absence of the bars associated to the CV-ACD-L for T5 means FAR@1stDet equal to zero.

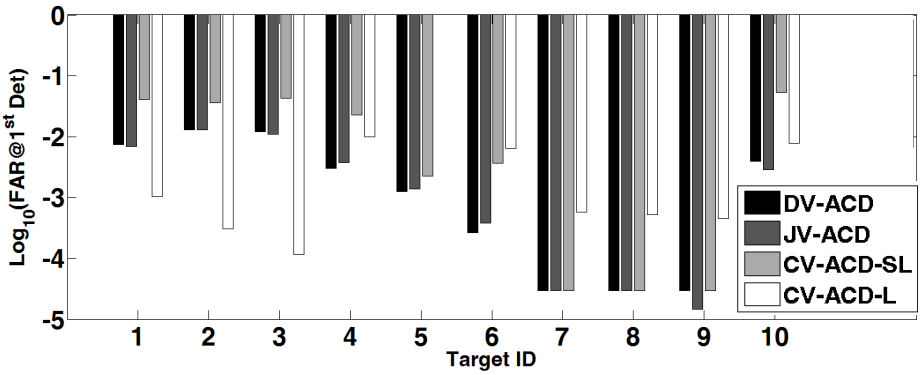

Figure 5.4: values of the FAR@1stDet (in logarithmic scale) obtained for T1-T10 by applying the different algorithms. DV-ACD - black, JV-ACD – dark gray, CV-ACD-SL - light gray, CV-ACD-L - white.

Figure 5.3 and Figure 5.4 confirm the qualitative conclusions drawn in the beginning of this section. Particularly, we note that:

- the performance of the DV-ACD method is very similar to that of the JV-ACD method, and slightly better than that of the CV-ACD-SL;
- with the exception of AC T6, the best SI is obtained with the CV-ACD-L approach for every AC in the GT. The low SI obtained with the CV-ACD-L method on the change T6 is explained noting that it is caused by a bias in the estimation of the parameters caused by the presence of spectral signatures similar to that of the AC T6 in the local background of the reference image (the white roof of the building in the middle of the scene);
- the DV-ACD method has the lowest values of the FAR@1stDet on the ACs T4, T6, T7 and T8, while the FAR@1stDet associated to CV-ACD-L is the lowest for the ACs T1, T2, T3 and T5.

Notice that both the SI and the FAR@1stDet confirm that the ACs denoted as T4 and T10 are the most difficult to detect.

To mitigate the effects of the RMR on the detection performance, the LCRA versions of the proposed algorithms have been applied to the real data. According to the RMR estimates obtained by the SRMRE algorithm, the LCRA has been applied exploiting a square uncertainty window W_R having size of 25×25 pixels. Figure **5.5** shows the ACD

statistic obtained by applying the LCRA approach to each of the four presented methods.

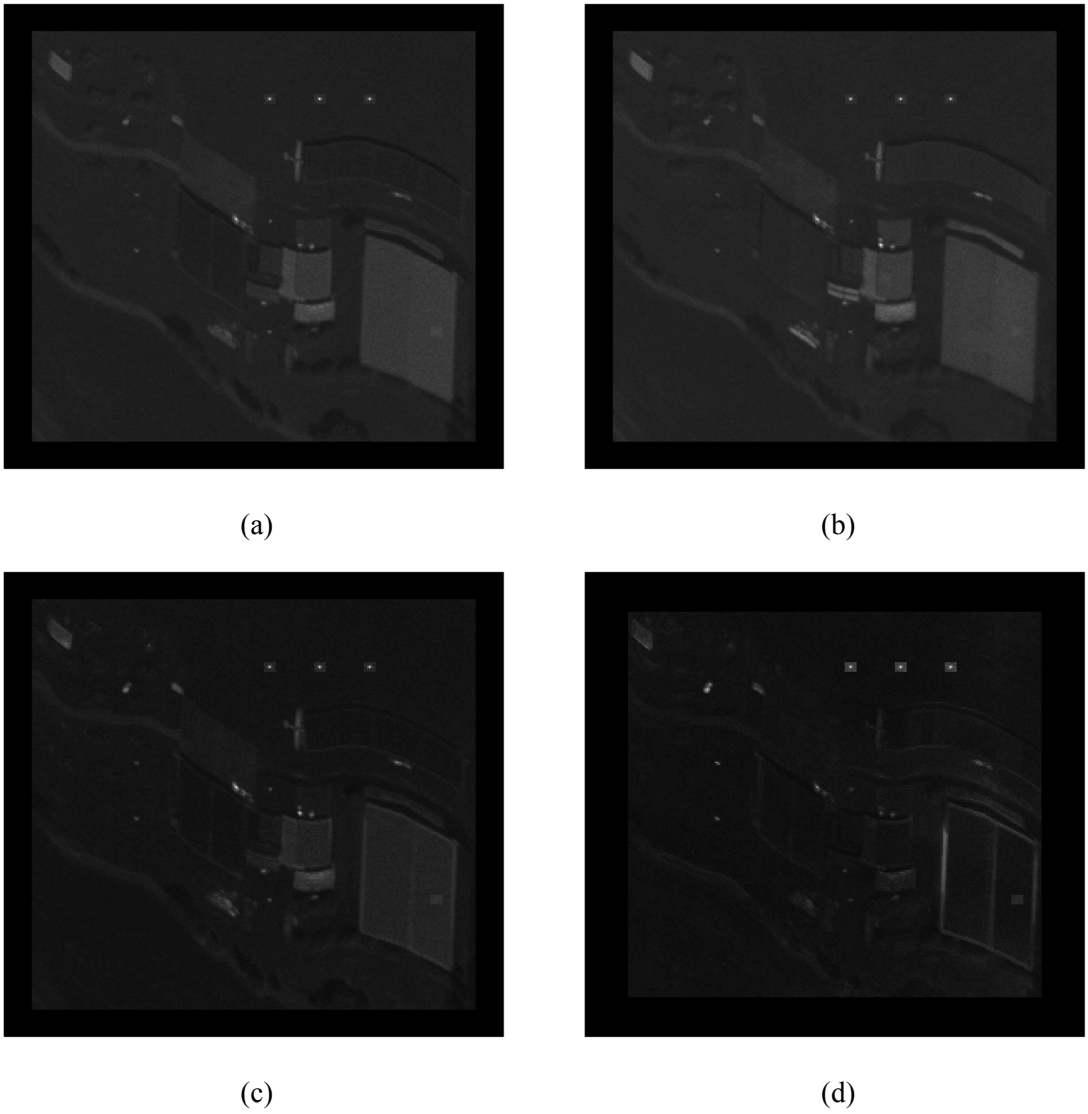

(a) (b)

(c) (d)

Figure 5.5: LCRA - ACD statistics obtained on the collected dataset by means of the: (a) DV-ACD, (b) JV-ACD, (c) CV-ACD-SL, (d) CV-ACD-L.

Notice that also in this case the ACD statistics of the DV-ACD and JV-ACD methods assume high values in the regions covered by the bright buildings at the top left and at the bottom right of the scene, (compare Figure 4.4 (a) and (b) with Figure 5.5 (a) and (b)), but the effect of the RMR is considerably reduced. It can be also noticed that the changes T1-T6 have a better contrast with respect to the statistic obtained without

LCRA compensation. Concerning the CV-ACD-SL, the benefit arising from the LCRA approach is more evident because the spurious detections along the edges of the buildings are better suppressed. Instead, the CV-ACD-L method seems to have no benefits from the LCRA approach because, as already mentioned, it is inherently more robust to RMR effects. Nevertheless, the spurious detections in the upper left and bottom right corner are greatly reduced and the AC_{CA} T10 is better emphasized (compare Figure 5.2 (d) with Figure **5.5** (d)).

In Figure 5.6 and Figure 5.7 we show the values of the SI and the FAR@1stDet, respectively, evaluated for all the considered ACs and obtained with the LCRA approach. The absence of the bars associated to the CV-ACD-L for T7, T8 and T9 indicates FAR@1stDet equal to zero.

Comparing Figure 5.6 with Figure 5.3, we can appreciate the better detectability of T1-T10. Particularly, we can easily notice that the SI values are always above 20dB, as compared to the previous case, where some of the most difficult ACs exhibited values below 15dB (see T2, T3 and T10 in Figure 4.7). Similarly to the results obtained in the original case, the highest SI values are reached by the CV-ACD-L approach, which overcomes the other methods in six of the ten considered ACs.

Also notice that the gap between the SI values of each AC in the CV-ACD-L method and those attained in the DV-ACD, JV-ACD and CV-ACD-SL methods is sensibly reduced in the LCRA approach with respect to the original case. This is explained recalling that, in the LCRA approach, the same uncertainty window W_R used to get better suppression of the RMR effects, can also reduce the detection performance. In fact, enlarging the dimension of W_R increases the probability that materials similar to the one in the pixel under test fall in its neighbourhood, thus preventing the detection (adjacency contamination). This effect, is more evident in the CV-ACD-L approach, where $\boldsymbol{\mu}_0(i,j)$ and $\boldsymbol{\Gamma}_0(i,j)$ are estimated locally from the reference image. As a result, they are more sensitive to adjacency contamination effects. Of course, this confirms the importance of an accurate geo-referencing step in the data collection to reduce the dimension of the uncertainty window as much as possible.

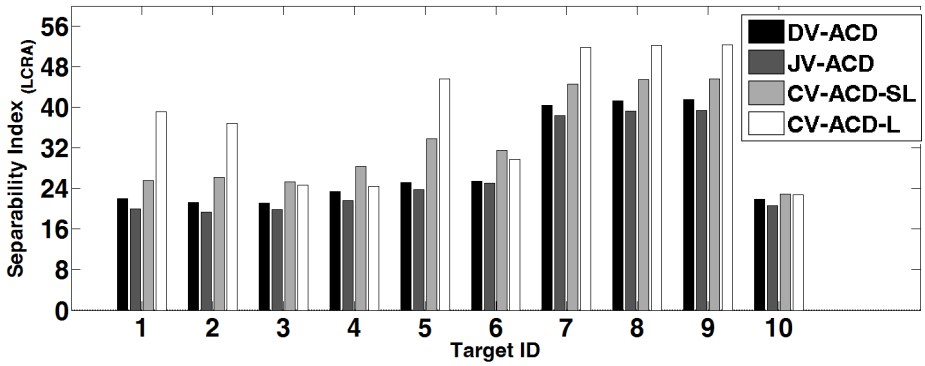

Figure 5.6: values of the SI (in *dB*) obtained for T1-T10 by applying the different algorithms in the LCRA case. DV-ACD - black, JV-ACD - dark gray, CV-ACD-SL - light gray, CV-ACD-L - white.

Similar conclusions can be drawn from the results presented in Figure 5.7, where the CV-ACD-L attains the lowest FAR@1stDet values for six of the ten evaluated ACs. However, the gap between the values of the FAR@1stDet assumed by the different methods is globally reduced. To give an example, the adjacency contamination effect deteriorates the FAR@1stDet of the AC T3 in the CV-ACD-L method, increasing from FAR@1stDet $\approx 10^{-4}$ in the first case, to FAR@1stDet $\approx 5 \cdot 10^{-3}$ in the LCRA case. Conversely, the FAR@1stDet of the same target in the DV-ACD and CV-ACD-SL decreases from values higher than $5 \cdot 10^{-2}$ to values lower than 10^{-3}. In addition, with the exception of AC T1, the same trend is evidenced by the ACs T2, T4, T6 and T10, where the FAR@1stDet in the CV-ACD-L method increases, while in the other methods it decreases.

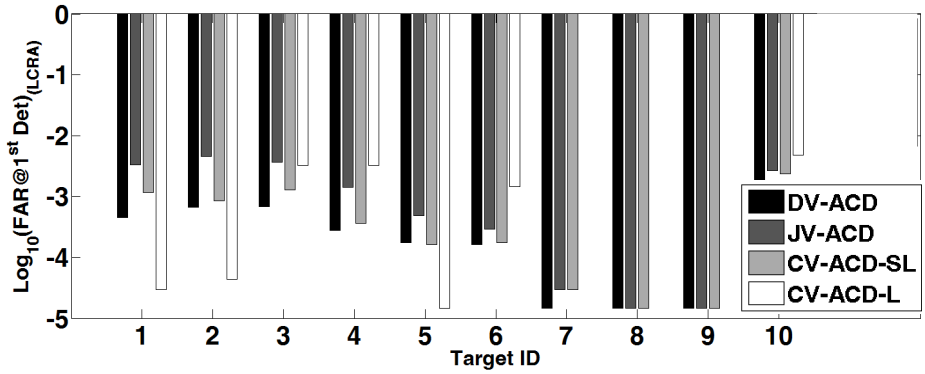

Figure 5.7: values of the FAR@1stDet (in logarithmic scale) obtained for T1-T10 by applying the different algorithms in the LCRA case. DV-ACD - black, JV-ACD - dark gray, CV-ACD-SL - light gray, CV-ACD-L - white.

5.3 Conclusions

In this chapter, we have presented a new technique for ACD in hyperspectral images, focusing on a specific class of detectors based on the squared Mahalanobis distance between the observation and the no change class. The proposed method overcomes the limitation due to RMR that affects images collected by airborne platforms. Afterwards, in the experimental section, the major advantages and drawbacks of the proposed method have been discussed by comparing the CV-ACD-SL and the CV-ACD-L methods with two well-known techniques for hyperspectral ACD, characterized by distinct methodologies, the DV-ACD and the JV-ACD. To this purpose, we adopted a real dataset consisting of two hyperspectral images with high spatial resolution. Adverse weather conditions during the acquisition and the moderate accuracy of the geo-referencing process resulted in a severe RMR distortion, thus making the ACD task very challenging.

The CV-ACD-L has been shown to be able to properly detect ACs in the case of severe geometrical distortion due to RMR. The method naturally provides a way to partially compensate the detrimental effects of the RMR because it is a local algorithm. In fact, the secondary data for the estimation of the parameters of the observed models are locally estimated from the reference image. In the presence of significant RMR distortion, global methodologies, such as the DV-ACD and the JV-ACD methods, inevitably lead to poor performance. As a consequence, CV-ACD-L undoubtedly represents a robust alternative to these approaches. At the same time, the advantage in detection performance exhibited by the CV-ACD-L algorithm with respect to the others, tends to vanish when a scheme suitable to cope with the RMR, such as the LCRA, is exploited, due to the concurrent adjacency effects that inevitably arise. In this situation the different algorithms are likely to exhibit similar performance. Benefits arising from the exploitation of the LCRA approach has been particularly evident in the case of the CV-ACD-SL method where, conversely to the CV-ACD-L case, the RMR effects are detrimental in terms of performance degradation if no RMR compensation scheme is provided.

It is worth noting that, the CV-ACD-L method is the only one suitable for processing the image line by line as data are collected, and it can be implemented in a quasi-real time processing scheme.

Chapter 6

Summary and conclusion

In this PhD thesis, the problem of Anomalous Change Detection in multi-temporal hyperspectral images has been addressed considering the main issues related to this research topic. For each aspect, a survey of the existing techniques has been carried out, highlighting the major drawbacks and disadvantages, and an original solution has been proposed in order to overcome the identified limitations. In particular, the analysis has been conducted in order to enforce the consistency of the global ACD processing chain. To this purpose, attention has been devoted to the two main phases which contribute to the ACD process, i.e. the pre-processing step and the detection step.

With reference to the first stage, two main contributions have been offered: i) an unsupervised technique for the estimation of the residual mis-registration noise affecting images collected from airborne sensors, and ii) an adaptive approach for ACD in HSI which mitigates the negative effects due to random noise.

The first contribution stems from the difficulty, in particular in airborne sensors, to achieve a perfect co-registration between images, thus resulting in the existence of a Residual Mis-Registration, i.e. a per-pixel shift in both the row and column directions.

When GPS positional errors, INS angular errors and DEM errors are not available, the estimation of the RMR noise remains an open issue. Since the correct evaluation of the magnitude of the RMR is crucial for ACD algorithms, a new fully unsupervised algorithm, named Sequential Residual Mis-Registration Estimation has been proposed to estimate the magnitude of the RMR directly from the image pairs. The proposed technique assumes the RMR as a unimodal bivariate random variable and estimates both its mean value and its covariance matrix. The method is based on the Scale Invariant Feature Transform algorithm, which represents a well-established technique for extracting interest points in gray level images on the basis of their local spatial features. The SIFT algorithm is embedded in a sequential processing scheme that allows the potential distinct spectral features present in the numerous channels of the hyperspectral data to be accounted for. The algorithm does not require ancillary data about the instrumentation accuracy. Therefore, when dealing with ACD problem, it can be successfully applied as a method to mitigate the effect of misalignment both after the co-registration step and in those applications that use the image pairs aligned through direct geo-referencing.

The results provided by the SRMRE have been analyzed on two different real HSIs. In particular, two different case studies have been considered. First, two geo-referenced HSIs collected over a rural scenario in similar illumination conditions have been tested providing an example of the use of the SRMRE in the so called direct geo-referencing applications. The estimates given by the SRMRE have been compared with the benchmark values obtained by means of a supervised technique. The analysis showed that the SRMRE provides results in accordance with the benchmark values and that the estimates are obtained from a number of observations much higher than that extracted by a version of the algorithm working on single-band images. The second test has been conducted on a pair of HSIs co-registered by using ground control points and collected over a scenario, composed of rural and urban areas, in variable illumination and shadow conditions. The analysis has emphasized both the effectiveness of the SRMRE in estimating the RMR noise due to the co-registration processing and the robustness of the SRMRE algorithm even when no preliminary processing had been performed in order to make the two images radiometrically comparable.

Afterwards, the attention has been focused on noise filtering techniques aimed at enforcing the consistency of the ACD process. A solution has been proposed to improve the robustness of the ACD algorithm based on an automatic band selection strategy where noisy bands are discarded. Such a strategy is adaptive since, for each PUT, a different number of bands is selected on the basis of the levels of the useful signal and of the random noise in that pixel. The algorithm exploits the estimates of the noise variance per pixel and per band and it also takes into account the presence of the signal dependent noise component in the random noise. This is of paramount importance in applications using data from new generation hyperspectral sensors where the signal dependent noise component is not negligible and cannot be ignored.

Band selection for each pixel is accomplished by retaining only the bands where the useful signal level is high with respect to the noise standard deviation. For this purpose, statistical decision theory has been used to derive a threshold based test to select the spectral channels. An experimental analysis has been conducted on a real dataset collected by the SIMGA VNIR camera over a urban scenario. It has demonstrated the effectiveness of the proposed approach, yielding to a consistent improvement of the detection capability with respect to the existing methods.

As to the detection step, it has been deeply analyzed reviewing the most common proposed techniques, in the purpose of embedding them in a common framework based on binary decision theory. Particular emphasis has been posed on statistical approaches, where ACD is derived in the framework of Neymann Pearson theory and the decision rule is carried out on the basis of the statistical properties assumed for the two hypotheses distribution, the observation vector space and the secondary data exploited for the estimation of the unknown parameters. Typically, ACD techniques assume that the observation represents the realization of jointly Gaussian spatial stationary random process. Though such assumption is adopted because of its mathematical tractability, it may be quite simplistic to model the multimodality usually met in real data. A more appropriate model is that adopted to derive the well known RX anomaly detector which assumes the local Gaussianity of the hyperspectral data.

In this framework, a novel contribution has been offered by presenting a new statistical ACD method which considers the local Gaussianity of the hyperspectral data. The assumption of local stationarity for the observations in the two hypotheses is taken into account by considering two different models, leading to two different detectors. The proposed technique has been shown to be able to properly detect ACs in the case of severe geometrical distortion due to RMR. The method naturally provides a way to partially compensate the detrimental effects of the RMR because it is a local algorithm. In fact, the secondary data for the estimation of the parameters of the observed models are locally estimated from the reference image. Therefore, whether global methodologies inevitably lead to poor performance in the presence of significant RMR distortion, the proposed approach represents a robust alternative to these approaches.

Further developments of the proposed techniques are scheduled with the perspective of enforcing the pre-processing step. In particular, in the light of the achieved results, the possibility to exploit Subspace Projection (SP) techniques in ACD will be investigated. SP, which represents a powerful tool for dimensionality reduction (DR) in HSIs, perform data reduction by projecting the data onto a linear space which addresses the most of their information content. DR based on SP relies on the assumption that, being the useful signal (the signal content of hyperspectral data) strongly correlated in the spectral dimension, it can be effectively represented in a linear space having dimension (or rank) much smaller than the number of spectral channels of the sensor. In practice, such linear space is not generally known and it must be estimated from the data themselves. This task is generally referred to as Signal Subspace Identification (SSI).

DR represents a key issue in HSI processing because the more compact representation of the data without significant information loss is beneficial in terms of noise mitigation, computational load reduction and fast data storage and retrieval. Furthermore, benefits from DR can be obtained also in classification and detection applications when the adopted algorithms need to estimate some parameters from training data collected from the image itself.

To the best of our knowledge, the problem of SSI for DR of two HSIs for ACD applications, has not been sufficiently analysed yet. Since the SSI techniques proposed in the past and working on a single HSI are not fully appropriate to be used in ACD applications, the effort will be concentrated towards the problem of jointly estimating the subspace addressing the relevant signal components of two multi-temporal HSIs.

References

[1] M. Butenuth, D. Frey, A.A. Nielsen, H. Skriver, "Infrastructure assessment for disaster management using multi-sensor and multi-temporal remote sensing imagery," International Journal of Remote Sensing, vol. 32, pp. 8575-8594, 2011.

[2] T. Fung, "An assessment of TM imagery for land-cover change detection," IEEE Transaction on Geoscience and Remote Sensing, vol. 28, pp. 681–684, 1990.

[3] S. Ghosh, L. Bruzzone, S. Patra, F. Bovolo, A. Ghosh, "A context-sensitive technique for unsupervised change detection based on Hopfield-type neural networks," IEEE Transaction on Geoscience and Remote Sensing, vol. 45, pp. 778-789, 2007.

[4] M. Shimoni, R. Heremans, D. Borghys, and C. Perneel, "Change Detection in Complex Industrial and Urban Scenes using VNIR and TIR Hyperspectral Imagery," 6th EARSeL SIG IS Workshop, 2009.

[5] F. Bovolo, L. Bruzzone, "A detail-preserving scale-driven approach to change detection in multitemporal SAR images," IEEE Transactions on Geoscience and Remote Sensing, Vol. 43, Issue 12, pp: 2963 - 2972, 2005.

[6] Y. Bazi, L. Bruzzone, F. Melgani, "An unsupervised approach based on the generalized Gaussian model to automatic change detection in multitemporal SAR images," IEEE Transactions on Geoscience and Remote Sensing, Vol. 43, Issue 4, pp: 874 - 887, 2005.

[7] N. Acito, S. Resta, G. Corsini, M. Diani, "Change Detection In Spotlight SAR Cosmo-Skymed Images For Harbour Infrastructures Monitoring: A Case Study," IEEE Tyrrhenian Workshop 2012 On Advances In Radar And Remote Sensing, pp. 1-4, 2012.

[8] N. Acito, S. Resta, G. Corsini, M. Diani, A. Rossi, "Unsupervised Change Detection In Very High Spatial Resolution COSMO-Skymed SAR Images," Proceedings of SPIE Conference SAR Image Analysis, Modeling, and Techniques XII, vol. 8536, pp. 853602-608, 2012.

[9] F. Bovolo, et al. "A support vector domain method for change detection in multitemporal images.", Pattern Recognition Lett., 2009.

[10] F. Bovolo, L. Bruzzone, "A theoretical framework for unsupervised change detection based on change vector analysis in the polar domain," IEEE Transaction on Geoscience and Remote Sensing, vol. 45, pp. 218-236, 2007.

[11] M. T. Eismann, J. Meola, A. D. Stocker, S. G. Beaven, and A. P. Schaum, "Airborne hyperspectral detection of small changes," Applied Optics, vol. 47, pp. F27–F45, 2008.

[12] K.R. Merril and L. Jiajun, "A comparison of four algorithms for change detection in an urban environment," Remote Sensing of Environment., vol. 63, pp. 95–100, 1998.

[13] S. Matteoli, M. Diani, and G. Corsini, “A tutorial overview of anomaly detection in hyperspectral images,” IEEE Aerosp. Electron. Syst. Mag. Tutorials, vol. 25, no. 7, pp. 5-28, 2010.

[14] D. Manolakis and G. Shaw, “Detection algorithms for hyperspectral imaging applications,” IEEE Signal Process. Mag., vol. 19, no. 1, pp. 29–43, 2002.

[15] D.W.J. Stein, S.G. Beaven, L.E. Hoff, E.M. Winter, A.P. Schaum, and A.D. Stocker, “Anomaly detection from hyperspectral imagery,” IEEE Signal Process. Mag., vol. 19, no. 1, pp. 58-69, 2002.

[16] I. Renhorn, D. Bourghys, U. De ceglie, R. Dekker, I. Kasen, S. Resta et al., "Detection in urban scenario using combined airborne imaging sensors," 5th International Symposium on Optronics in Defence and Security (OPTRO)," pp 1-6, 2012.

[17] I. Renhorn, D. Bourghys, X. Briottet, U. De ceglie, R. Dekker, S. Resta, et al., "Detection in urban scenario using combined airborne imaging sensors," Proc. of SPIE Conference Infrared Technology and Applications XXXVIII, vol. 8353, pp.1-7, 2012.

[18] I. Renhorn, M. Axelsson, R.J. Dekker, I. Kåsen, M. Lo Moro, S. Resta, et al., "Hyperspectral reconnaissance in urban environment," Accepted for SPIE Defense, Security, and Sensing, Baltimore, 2013

[19] Resta, S.; Acito, N.; Diani, M.; Corsini, G.; Opsahl, T.; Haavardsholm, T.V.; "Detection of small changes in airborne hyperspectral imagery: Experimental results over urban areas," 6th International Workshop on the Analysis of Multi-temporal Remote Sensing Images (Multi-Temp), 2011.

[20] M.L.F. Velloso, F.J. de Souza, M. Simoes, "Improved radiometric normalization for land cover change detection: an automated relative correction with artificial neural network," IEEE International Geoscience and Remote Sensing Symposium, pp 3435 - 3437, 2002.

[21] D.M. Muchoney and B.N. Haack, “Change detection for monitoring forest defoliation,” Photogrammetric Engineering and Remote Sensing, vol. 60, pp. 1243–1251, 1994.

[22] L. Bruzzone and D. Fernàndez Prieto, “Automatic analysis of the difference image for unsupervised change detection,” IEEE Transaction on Geoscience and Remote Sensing., vol. 38, pp. 1171–1182, 2000.

[23] P. S. Chavez, Jr. and D. J. MacKinnon, “Automatic detection of vegetation changes in the southwestern United States using remotely sensed images,” Photogrammetric Engineering and Remote Sensing, vol. 60, pp. 1285–1294, 1994.

[24] B. Zitova, J. Flusser, “Image registration methods: a survey,” Image and Vision Computing, vol. 21, pp. 977-1000, 2003.

[25] X. Dai, S. Khorram, “The effects of image misregistration on the accuracy of remotely sensed change detection,” IEEE Transaction on Geoscience and Remote Sensing, vol. 36, pp. 1566-1577, 1998.

[26] Goshtasby, “2D and 3D image registration for medical, remote sensing, and industrial applications,” Wiley-Interscience publication, New Jersey, 2005.

[27] Liu, P. Gong, M. Kelly, Q. Guo, “Automatic registration of airborne images with complex local distortion,” Photogrammetric Engineering and Remote Sensing, vol. 72, pp. 1049-1059, 2006.

[28] N. Bourdis, D. Marraud, H. Sahbi, "Constrained optical flow for aerial image change detection," IEEE International Geoscience and Remote Sensing Symposium, pp. 4176-4179, 2011.

[29] S. Watanabe and K. Miyajima, “Detecting building changes using epipolar constraint from aerial images taken at different positions,” Proceedings of the International Conference on Image Processing, vol. 2, pp. 201–204, 2001.

[30] M.T. Eismann, J. Meola, R.C. Hardie, “Hyperspectral Change Detection in the Presence of Diurnal and Seasonal Variations”, IEEE Transactions on Geoscience and Remote Sensing, vol. 46, pp. 237-249, 2008.

[31] Schaum, and A. Stocker, “Hyperspectral change detection and supervised matched filtering based on covariance equalization,” In Proc. SPIE, 5425, 77–90, 2004.

[32] J. Theiler, C. Scovel, B. Wohlberg, B.R. Foy, "Elliptically Contoured Distributions for Anomalous Change Detection in Hyperspectral Imagery," Geoscience and Remote Sensing Letters, IEEE, vol.7, issue 2, pp. 271-275, April 2010.

[33] A.A. Nielsen, "The Regularized Iteratively Reweighted MAD Method for Change Detection in Multi and Hyperspectral Data," IEEE Transactions on Image Processing, vol. 16, no. 2, pp. 463-478, Feb. 2007.

[34] J. Theiler, "Quantitative comparison of quadratic covariance-based anomalous change detectors," Applied Optics, vol. 47, pp. F12–F26, 2008.

[35] J. Meola, M.T. Eismann, R.L. Moses, J.N. Ash, “Application of Model-Based Change Detection to Airborne VNIR/SWIR Hyperspectral Imagery,” IEEE Transactions on Geoscience and Remote Sensing, vol. 50, pp. 3693 - 3709, 2012.

[36] Schaum, A. Stocker, "Long-Interval Chronochrome Target Detection," Proceedings of International Symposium on Spectral Sensing Research, 1998.

[37] Schaum, A. Stocker, "Linear Chromodynamics Models for Hyperspectral Target Detection," IEEE Aerospace Conference, IEEE, Feb. 2003.

[38] M. J. Carlotto, "A cluster-based approach for detecting man-made objects and changes in imagery," IEEE Transactions on Geoscience and Remote Sensing, vol. 43, no. 2, pp. 374-387, Feb. 2005.

[39] Clifton, “Change detection in overhead imagery using neural networks,” Applied Intelligence, vol. 18, pp. 215–234, 2003.

[40] C. Bustos, O. Campanella, K. Kpalma, "A method for change detection with multi-temporal satellite images based on Principal Component Analysis," 6th International Workshop on the Analysis of Multi-temporal Remote Sensing Images (Multi-Temp), pp. 197-200, 2011.

[41] N. Acito, S. Resta, M. Diani, G. Corsini, "Joint signal subspace identification in hyperspectral images for change detection applications," Submitted to IEEE Transactions on Geoscience and Remote Sensing, 2012.

[42] M. Diani, S. Resta, N. Acito, G. Corsini, S.U. de Ceglie, "A novel technique for adaptive anomalous change detection in airborne hyperspectral imagery," Proc. SPIE 8542, Electro-Optical Remote Sensing, Photonic Technologies, and Applications VI, pp. 854220-226, 2012.

[43] O.A. Carvalho Júnior, R.F. Guimarães, A.R. Gillespie, N.C. Silva and R.A.T. Gomes, "A New Approach to Change Vector Analysis Using Distance and Similarity Measures," Remote Sensing, vol. 3, pp. 2473-2493, 2011.

[44] J. Theiler and S. Perkins, "Proposed Framework for Anomalous Change Detection," ICML Workshop on Machine Learning Algorithms for Surveillance and Event Detection, pp. 7 - 14, 2006.

[45] B. Wohlberg, J. Theiler, "Improved change detection with local co-registration adjustments," First Workshop on Hyperspectral Image and Signal Processing: Evolution in Remote Sensing, IEEE, WHISPERS, 2009.

[46] L. Bruzzone, R. Cossu, M. Gomarasca, "Adaptive estimation of the registration-noise distribution for accurate unsupervised change detection," IEEE 2001 International Geoscience and Remote Sensing Symposium, IGARSS, 2001.

[47] F. Bovolo, L. Bruzzone and S. Marchesi, "Analysis and Adaptive Estimation of the Registration Noise Distribution in Multitemporal VHR Images," IEEE Transactions on Geoscience and Remote Sensing, vol. 47, no. 8, Aug. 2009.

[48] L. Lining, W. Yunhong, Y. Wang, "Tie points based pixel-level compensation of misregistration for change detection," IEEE International Geoscience and Remote Sensing Symposium, IGARSS, 2010.

[49] N. Yokoya, N. Miyamura, A. Iwasaki, "Detection and correction of spectral and spatial misregistrations for hyperspectral data," IEEE International Geoscience and Remote Sensing Symposium, IGARSS, 2010.

[50] W. Hongqing, C. Erle Ellis, "Image Misregistration Error in Change Measurements," Photogrammetric Engineering & Remote Sensing, Vol. 71, No. 9. pp. 1037-1044, 2005.

[51] B. Wohlberg, J. Theiler, "Symmetrized local co-registration optimization for anomalous change detection," Proc. SPIE Computational Imaging VIII, vol. 7533, pp. 753307, Jan. 2010.

[52] J. Theiler, B. Wohlberg, "Local Coregistration Adjustment for Anomalous Change Detection," IEEE Transaction on Geoscience and Remote Sensing, vol. 50, pp. 3107-3116, 2012.

[53] K.M. Brown, G.M. Foody, P.M. Atkinson, "Modeling geometric and misregistration error in airborne sensor data to enhance change detection," Int. Journal of Remote Sensing, vol. 28, issue 12, June 2007.

[54] N. Acito, S. Resta, M. Diani, G. Corsini, "Residual misregistration noise estimation in hyperspectral anomalous change detection," Optical Engineering, vol. 51, issue 11, pp. 111705, 2012.

[55] N. Acito, M. Diani, G. Corsini, "Signal-Dependent Noise Modeling and Model Parameter Estimation in Hyperspectral Images", IEEE Transaction on Geoscience and Remote Sensing, Vol. 49, No. 8, pp. 2957-2971, 2011.

[56] S. Resta, N. Acito, M. Diani, G. Corsini, " A theoretical framework for anomalous change detection in hyperspectral images based on hypothesis test," Submitted to IEEE Transactions on Geoscience and Remote Sensing, 2012.

[57] D.G. Lowe, "Object recognition from local scale-invariant features," International Conference on Computer Vision, Corfu, Greece, September 1999.

[58] D.G. Lowe, "Distinctive Image Features from Scale-Invariant Keypoints," International Journal of Computer Vision, vol. 60, issue 2, pp. 91-110, 2004.

[59] N. Acito, S. Resta, M. Diani, G. Corsini, "A robust technique for anomalous change detection in airborne hyperspectral imagery based on automatic and adaptive band selection," Submitted to Optical Engineering, 2012.

[60] R. Rasi, O. Kissiyar, M. Vollmar, "Land cover change detection thresholds for Landsat data samples," 2011 6th International Workshop on the Analysis of Multi-temporal Remote Sensing Images (Multi-Temp), pp: 205 - 208, 2011.

[61] D. Lu, P. Mausel, E. Brondízio, and E. Moran, "Change detection techniques," Int. J. Remote Sensing, Vol. 25, No. 12, Taylor&Francis, pp. 2365-2407, 2004.

[62] O.A. de Carvalho Junior, "Spectral change detection," IEEE International Geoscience and Remote Sensing Symposium, IGARSS 2007, pp: 1935 - 1938, 2007.

[63] O.A. Carvalho Júnior, R.F. Guimarães, A.R. Gillespie, N.C. Silva and R.A.T. Gomes, "A New Approach to Change Vector Analysis Using Distance and Similarity Measures," Remote Sensing, vol. 3, pp: 2473-2493, 2011.

[64] P.R. Coppin, M.E. Bauer, "Processing of multitemporal Landsat TM imagery to optimize extraction of forest cover change features". IEEE Transactions on Geoscience and Remote Sensing, vol. 60, Issue 3, pp. 287–298, 1994.

[65] O.A. Carvalho Júnior, P.R. Menezes, "Spectral Correlation Mapper (SCM): An Improving Spectral Angle Mapper," Summaries of the Ninth JPL Airborne Earth Science Workshop, vol. 1, AVIRIS Workshop, pp. 65-74, 2000.

[66] L. Bruzzone, R. Cossu, "An adaptive approach to reducing registration noise effects in unsupervised change detection," IEEE Transactions on Geoscience and Remote Sensing, Vol: 41, Issue: 11, pp: 2455 - 2465, 2003.

[67] R.A. Leathers, A.P. Schaum, T.V. Downes, "Signature evolution with covariance equalization in oblique hyperspectral imagery," Proc. SPIE 6233, Algorithms and Technologies for Multispectral, Hyperspectral, and Ultraspectral Imagery XII, pp.623307, 2006.

[68] W. Wang, J. Hong, Y. Tang, "Image Matching for Geomorphic Measurement Based on SIFT and RANSAC Methods," IEEE International Conference on Computer Science and Software Engineering, 2008.

[69] M. Hubert, M. Debruyne, "Minimum covariance determinant," WIREs Computational Statistic Conference, 2010.

[70] P.L. Chebyshev, "A source book in mathematics," New York: McGraw-Hill, pp. 580–587, 1929.

[71] R.M. Haralick, L.G. Shapiro, "Computer and Robot Vision," Volume II, Addison-Wesley pp. 316-317, 1992.

[72] Snyder, J. Kerekes, I. Fairweather, R. Crabtree, J. Shive, and S. Hager, "Development of a Web-based Application to Evaluate Target Finding Algorithms," Proceedings of the 2008 IEEE International Geoscience and Remote Sensing Symposium (IGARSS), vol. 2, pp. 915-918, Boston, MA, 2008.

[73] T. Cocks, R. Jenssen, A. Stewart, I. Wilson, and T. Shields, "The HyMap Airborne Hyperspectral Sensor: the System, Calibration and Performance," Proc. 1st EARSeL Workshop on Imaging Spectroscopy, EARSeL, Paris, pp. 37-43, 1998.

[74] Keju Peng, C. Xin, Z. Dongxiang, L. Yunhui, "3D reconstruction based on SIFT and Harris feature points," IEEE International Conference on Robotics and Biomimetics (ROBIO), 2009.

[75] Flint, A. Dick, A. van den Hengel, "Thrift: Local 3D Structure Recognition," 9th Biennial Conference of the Australian Pattern Recognition Society on Digital Image Computing Techniques and Applications, pp. 182 - 188, 2007.

[76] A.G. Evans, U.V. Bhapkar, J.P. Cunningham, B.R. Hermann, J.P. Dugan, J.Z. Williams, "Fusion of Reference-Aided GPS, Imagery, and Inertial Information for Airborne Geolocation," 13th International Technical Meeting of the Satellite Division of the Institute of Navigation, 2000.

[77] C. Campion, J.P. Dugan, C.C. Piotrowski, A.G. Evans, "Direct geo-referencing technique for rapid positioning of targets and environmental products using tactical grade airborne imaging data," IEEE OCEANS 2002, Issue: 2002, Volume: 3, pp: 1603-1608, 2002.

[78] T. Farin and P.H.N. de With, "Misregistration Errors in change detection algorithms and how to avoid them," International Conference on Image Processing (ICIP), vol. 2, pp. 438-441, 2005.

[79] J. Meola, M.T. Eismann, R.L. Moses, J.N. Ash, "Detecting Changes in Hyperspectral Imagery Using a Model-Based Approach," IEEE Transactions on Geoscience and Remote Sensing, Vol 49, Issue 7, pp 2647-2661, 2011.

[80] W. Hongqing, C. Erle Ellis, "Image Misregistration Error in Change Measurements," Photogrammetric Engineering & Remote Sensing, Vol. 71, No. 9. pp. 1037-1044, 2005.

[81] N. Acito, S. Resta, M. Diani, G. Corsini, “Residual misregistration noise estimation in hyperspectral anomalous change detection”, Optical. Engineering. 51, 111705 (2012).

[82] N. Acito, M. Diani, G. Corsini, “Signal-Dependent Noise Modeling and Model Parameter Estimation in Hyperspectral Images”, IEEE Transaction on Geoscience and Remote Sensing, Vol. 49, No. 8, pp. 2957-2971, August 2011.

[83] J. Meola, M. T. Eismann, R. L. Moses, and J. N. Ash, “Modeling and estimation of signal-dependent noise in hyperspectral imagery”, Applied Optics, Vol. 50, No. 21, pp. 3829-3846, 2011.

[84] J.M. Bioucas-Dias, J.M.P. Nascimento, “Hyperspectral Subspace Identification”, IEEE Transactions on Geoscience and Remote Sensing, vol. 46, no. 8, Aug. 2008, pp. 2435-2445.

[85] N. Acito, M. Diani, G. Corsini, “Residual striping reduction in hyperspectral images”, 17th International Conference on Digital Signal Processing, 2011, doi: 10.1109/IACDSP.2011.6005002, pp.1-7.

[86] N. Acito, M. Diani, G. Corsini, “Subspace-Based Striping Noise Reduction in Hyperspectral Images“, IEEE Trans. on Geoscience and Remote Sensing, Vol.49, No. 4, February 2011, pp. 1325-1342.

[87] J. Meola, M.T. Eismann, "Image misregistration effects on hyperspectral change detection," Proceedings of the SPIE, Algorithms and Technologies for Multispectral, Hyperspectral, and Ultraspectral Imagery XIV, vol. 6966, pp. 69660-69669, 2008.

[88] I.S. Reed, X. Yu, "Adaptive multiple-band CFAR detection of an optical pattern with unknown spectral distribution," IEEE Transactions on Acoustics, Speech, and Signal Processing, vol. 38, pp. 760-770, 1990.

[89] S. Resta, N. Acito, M. Diani, G. Corsini, "Unsupervised mis-registration noise estimation in multi-temporal hyperspectral images," Proc. SPIE 8537, Image and Signal Processing for Remote Sensing XVIII, pp. 85370-75, 2012.

[90] R. Mayer, F. Bucholtz, D. Scribner, "Object detection by using 'whitening/dewhitening' to transform target signatures in multitemporal hyperspectral and multispectral imagery," IEEE Transaction on Geoscience and Remote Sensing, vol. 41, no. 5, pp. 1136–1142, 2003.

[91] N. Acito, G. Corsini, M. Diani, "Statistical analysis of hyper-spectral data: a non-Gaussian approach," Eurasip Journal on Advances in Signal Processing, vol. 2007, pp 1-10, 2007.

[92] B. Marden and D. Manolakis, "Modeling hyperspectral imaging data," Proc. SPIE, vol. 5093, pp. 253–262, 2003.

[93] N. Acito, M. Diani, G. Corsini, "Hyperspectral Signal Subspace Identification in the Presence of Rare Vectors and Signal-Dependent Noise," IEEE Transaction on Geoscience and Remote Sensing, vol. PP, pp. 1-17, 2012.

List of Publications

Journals

[1] N. Acito, S. Resta, M. Diani, G. Corsini, "Residual misregistration noise estimation in hyperspectral anomalous change detection," Optical Engineering, vol. 51, issue 11, pp. 111705, 2012. doi:10.1117/1.OE.51.11.111705.

[2] N. Acito, S. Resta, M. Diani, G. Corsini, "A robust technique for anomalous change detection in airborne hyperspectral imagery based on automatic and adaptive band selection," Accepted for Optical Engineering, 2013.

[3] N. Acito, S. Resta, M. Diani, G. Corsini, "Joint signal subspace identification in hyperspectral images for change detection applications," Submitted to IEEE Transactions on Geoscience and Remote Sensing, 2012.

[4] S. Resta, N. Acito, M. Diani, G. Corsini, " A theoretical framework for anomalous change detection in hyperspectral images based on hypothesis test," Submitted to IEEE Transactions on Geoscience and Remote Sensing, 2012.

Conference Proceedings

[5] N. Acito, G. Corsini, M. Diani, S. Matteoli, S. Resta, "A novel technique for hyperspectral signal subspace estimation in target detection applications," IEEE International Geoscience and Remote Sensing Symposium (IGARSS), vol.3, pp 95-98, 2008. doi: 10.1109/IGARSS.2008.4779291.

[6] S. Resta, N. Acito, M. Diani, G. Corsini, "Signal subspace estimation in hyperspectral data for target detection applications," IEEE Gold Remote Sensing Conference, pp 1-4, Livorno, Italy, 2010.

[7] S. Resta, N. Acito, M. Diani, G. Corsini, T. Opsahl, T.V. Haavardsholm, "Detection of small changes in airborne hyperspectral imagery: Experimental results over urban areas, IEEE 6th International Workshop on the Analysis of Multi-temporal Remote Sensing Images (Multi-Temp)," pp 5-8, 2011. doi: 10.1109/Multi-Temp.2011.6005033.

[8] I. Renhorn, M. Axelsson, C. Benoist, D. Bourghys, Y. Boucher, X. Briottet, U. De ceglie, R. Dekker, A. Dimmeler, O. Friman, I. Kasen, J. Maerker, S. Resta, P. Schwering, M. Shimoni, T. Haavardsholm, M. Van persie, "Detection in urban scenario using combined airborne imaging sensors," 5th International Symposium on Optronics in Defence and Security (OPTRO)," pp 1-6, 2012.

[9] I. Renhorn, M. Axelsson, C. Benoist, D. Bourghys, Y. Boucher, X. Briottet, U. De ceglie, R. Dekker, A. Dimmeler, O. Friman, I. Kasen, J. Maerker, S. Resta, P. Schwering, M. Shimoni, T. Haavardsholm, M. Van persie, "Detection in urban scenario using combined airborne imaging sensors," Proceedings of SPIE Conference Infrared Technology and Applications XXXVIII, vol. 8353, pp.1-7, 2012. doi:10.1117/12.921473.

[10] N. Acito, S. Resta, G. Corsini, M. Diani, "Change Detection In Spotlight SAR Cosmo-Skymed Images For Harbour Infrastructures Monitoring: A Case Study," IEEE Tyrrhenian Workshop 2012 On Advances In Radar And Remote Sensing, pp. 193-197, 2012. doi: 10.1109/TyWRRS.2012.6381128.

[11] N. Acito, S. Resta, G. Corsini, M. Diani, A. Rossi, "Unsupervised Change Detection In Very High Spatial Resolution COSMO-Skymed SAR Images," Proceedings of SPIE Conference SAR Image Analysis, Modeling, and Techniques XII, vol. 8536, pp. 853602-608, 2012. doi:10.1117/12.974663.

[12] S. Resta, N. Acito, M. Diani, G. Corsini, "Unsupervised mis-registration noise estimation in multi-temporal hyperspectral images," Proceedings of SPIE Conference Image and Signal Processing for Remote Sensing XVIII, vol. 8357, pp. 85370Q, 2012. doi:10.1117/12.974216.

[13] M. Diani, S. Resta, N. Acito, G. Corsini, S.U. De Ceglie, "A Novel Technique For Adaptive Anomalous Change Detection In Airborne Hyperspectral Imagery," Proceedings of SPIE Conference Electro-Optical Remote Sensing, Photonic Technologies, and Applications VI, Vol. 8542-81, pp. 854220, 2012. doi:10.1117/12.974628.

[14] I.G. Renhorn, M. Axelsson, R.J. Dekker, I. Kåsen, M. Lo Moro, S. Resta, et al., "Hyperspectral reconnaissance in urban environment," Accepted for SPIE Defense, Security, and Sensing, Baltimore, 2013.